

**Spectroscopy of Excited States of ^{130}Cd and
Simulations and Detector Developments for HISPEC
Slowed Down Beam Experiments**



Inaugural-Dissertation
zur
Erlangung des Doktorgrades
der Mathematisch-Naturwissenschaftlichen
Fakultät der Universität zu Köln

Author: Michael Armstrong

Institut für Kernphysik
Universität zu Köln

Friday 31st May, 2024

First reviewer: Prof. Dr. Jan Jolie
Second reviewer: Prof. Dr. Peter Reiter

Date of oral defense: 12th April 2024

Erklärung zur Dissertation
gemäß der Promotionsordnung vom 12. März 2020

Diese Erklärung muss in der Dissertation enthalten sein.
(This version must be included in the doctoral thesis)

„Hiermit versichere ich an Eides statt, dass ich die vorliegende Dissertation selbstständig und ohne die Benutzung anderer als der angegebenen Hilfsmittel und Literatur angefertigt habe. Alle Stellen, die wörtlich oder sinngemäß aus veröffentlichten und nicht veröffentlichten Werken dem Wortlaut oder dem Sinn nach entnommen wurden, sind als solche kenntlich gemacht. Ich versichere an Eides statt, dass diese Dissertation noch keiner anderen Fakultät oder Universität zur Prüfung vorgelegen hat; dass sie - abgesehen von unten angegebenen Teilpublikationen und eingebundenen Artikeln und Manuskripten - noch nicht veröffentlicht worden ist sowie, dass ich eine Veröffentlichung der Dissertation vor Abschluss der Promotion nicht ohne Genehmigung des Promotionsausschusses vornehmen werde. Die Bestimmungen dieser Ordnung sind mir bekannt. Darüber hinaus erkläre ich hiermit, dass ich die Ordnung zur Sicherung guter wissenschaftlicher Praxis und zum Umgang mit wissenschaftlichem Fehlverhalten der Universität zu Köln gelesen und sie bei der Durchführung der Dissertation zugrundeliegenden Arbeiten und der schriftlich verfassten Dissertation beachtet habe und verpflichte mich hiermit, die dort genannten Vorgaben bei allen wissenschaftlichen Tätigkeiten zu beachten und umzusetzen. Ich versichere, dass die eingereichte elektronische Fassung der eingereichten Druckfassung vollständig entspricht.“

Teilpublikationen:

Datum, Name und Unterschrift

18/01/2024

Michael Armstrong



Acknowledgements

I foresee in years to come that I will eventually forget all about ^{130}Cd . That I will have no idea what HISPEC even stands for. But I will never forget the people who have supported me. Nor what they taught me in these brief few years, least of all that which I have learned as a student in life more even than as student of physics.

I most of all cannot overstate the contribution of Magda Górska, who has guided me, supported me and often rightfully lectured me ;) at GSI. I will never forget my times with the people of the nuclear spectroscopy department she has inherited from Jürgen Gerl at GSI and the friendly atmosphere they together have built that has attracted the colourful cast of locals, who without their own group now join us for lunch and coffee each day.

This opportunity would never have existed if it weren't for Jan Jolie, his research group and his students who took me for my first night out in Köln in anticipation of my first accelerator experiment, navigated me through years of administration and taught me that at least in the nuclear physics context plungers don't always bear relation to unclogging toilets. He who, together with Gereon Hackenberg and Dennis Bittner, I fondly remember designing and building an array of magnets for a detector. This detector I was later disappointed to learn is only as strong as a common fridge magnet.

I thank also the very many members of my friends and family whose love I cherish. Those who have each Christmas put up with the many science trivia discussions I have initiated and any and all unsolicited corrections of sci-fi media we have jointly consumed.

Finally I thank those few stalwart and brilliant men who have put me on this path in life, Hugh Dunlop who instilled a driving love of the natural sciences, Laurence Hartnett whose moral and mathematical instruction has proven as key to my happiness as my studies, Jerry Gilfoyle who's energy and optimism showed me the fun that can be had in physics and finally my father who's exemplary dedication to our family at work and at home continues to put me to shame.

Contents

Contents	ii
List of Figures	v
List of Tables	xii
1 Introduction	2
2 Physics background	4
2.1 Stellar nucleosynthesis	4
2.2 R-process	5
2.2.1 R-process path	5
2.3 The nuclear shell model	6
2.3.1 Independent particle motion	7
2.3.2 Shell model calculations	12
2.3.3 The doubly magic ^{132}Sn region	12
2.4 Electromagnetic transitions	15
2.4.1 Transition strengths	15
2.5 Coulomb Excitation	16
2.5.1 Safe Coulex	16
2.5.2 Semi-classical approach	17
2.6 Production of rare isotope beams	17
2.6.1 Abrasion fission	17
2.6.2 Knockout reactions	18
3 Excited States of ^{130}Cd	19
3.1 HiCARI Experiments	19
3.2 BigRIPS-ZeroDegree particle identification	19
3.2.1 Particle identification with the $TOF - B\rho - \Delta E$ method	20
3.2.2 Charge state changes	21
3.2.3 PPAC detectors	21
3.2.4 MUSIC detectors	23
3.2.5 Plastic scintillators	24
3.2.6 A/Q correction coefficients	24

3.2.7	Reaction channels statistics	28
3.3	HiCARI HPGe array	28
3.3.1	High-purity Germanium detectors	29
3.3.2	Doppler correction in HiCARI in-flight decay spectroscopy experiments	30
3.3.3	Emission angle and velocity reconstruction	30
3.3.4	HiCARI array geometry	33
3.4	Analysis of HiCARI experiment	35
3.4.1	Experimental energy calibration	35
3.4.2	Simulated HiCARI HPGe energies	35
3.4.3	Detector Efficiency	36
3.4.4	Comparison of simulated and experimental detection efficiency	39
3.4.5	Validation of energy-lifetime extraction with ^{131}In	40
3.5	Studies of the excited states of ^{130}Cd	47
3.5.1	Observed transitions	47
3.5.2	Constructing the ^{130}Cd level scheme	48
3.5.3	^{130}Cd decay cascade fitting function	49
3.5.4	Initial parameters for ^{130}Cd gamma-ray energy spectrum fitting	51
3.5.5	Interdependent ^{130}Cd gamma-ray energy spectrum fitting	53
3.6	Results of studies of ^{130}Cd	57
3.6.1	Strengths of transitions between excited states of ^{130}Cd	59
3.7	Discussion of ^{130}Cd results	60
3.7.1	Excitation energies	60
3.7.2	Transition strengths	60
3.7.3	Summary of ^{130}Cd results	61
4	Simulations for HISPEC Slowed Down Beam Campaign	62
4.1	Slowed down beam experiments at FAIR	62
4.1.1	Low energy coulomb Excitation	63
4.2	Slowing down ions in SDB experiments	63
4.3	Particle identification in SDB experiments	65
4.3.1	Mass reconstruction	65
4.3.2	Atomic number reconstruction	66
4.4	SDB kinematics and Doppler correction	66
4.4.1	Reconstructing emission angles	66
4.4.2	Measuring transition strengths in SDB experiments	66
4.4.3	Angular straggling	68
4.5	HPGe Background Discrimination	69
4.5.1	Shielding	69
4.5.2	Timing conditions	70
4.5.3	Ion kinematics conditions	70
4.6	Estimated Required Detector performances	70

4.7	Simulations for SDB Experiments	71
4.7.1	Geant4 simulations for SDB experiments	72
4.7.2	SDB simulation architecture	72
4.7.3	Geant4 simulated SDB geometry	73
4.7.4	Coulomb excitation in Geant4	73
4.7.5	^{64}Ni SuperFRS ion-transport simulations	76
4.7.6	Target spacing	78
4.7.7	Geant4 EM Physics Validation	80
4.7.8	DSSSD Geometry	84
4.7.9	SDB DSSSD pileup	86
4.7.10	DSSSD array geometry investigations	89
4.7.11	Simulated SDB particle identification reconstruction	91
4.7.12	Simulated SDB gamma-ray reconstruction	92
4.7.13	Simulated HPGe noise discrimination	94
4.8	Study of required detector performance parameters	96
4.8.1	Performance parameters for particle identification	96
4.8.2	Performance parameters for gamma-ray Doppler correction	97
4.8.3	Comparison of new requirements for detectors to previous estimates	100
4.9	Hypothetical ^{64}Ni SDB test experiment	100
4.9.1	Conclusions of simulations for SDB experiments	102
5	Bibliography	103

List of Figures

2.1	Solar nuclear abundance as a function of atomic number [14].	4
2.2	Binding energy per nucleon for elements as a function of atomic mass. Annotated with the iron peak, showing the point at which fusion and fission reactions are energetically favoured [16].	5
2.3	Plot of nuclear proton number against neutron number illustrating horizontal r-process neutron capture path from ^{56}Fe seed nuclei and vertical path through waiting point nuclei [20]	6
2.4	Schematic representation of (a) spacing of single particle energy levels in a harmonic oscillator for each N, (b) orbital angular momentum l splitting in a Woods-Saxon potential and (c) spin-orbit splitting for orbitals with j total angular momenta. These levels increase vertically in energy and are labelled in (e) with each nl_j substate, (f) parity and (g) total number of occupying nucleon [20].	9
2.5	Illustration of coupling between nucleons in j and j' orbitals forming J total angular momentum states. Parallel and anti-parallel (j, j') projections showing maximum and minimum J states respectively. Modified figure from [27].	10
2.6	Solar r-process abundance distributions compared to two r-process calculations. Black line showing the assumption of a pronounced d	13
2.7	Illustration of single particle or hole proton π and neutron ν energies for ^{132}Sn . Updated version of plot from [37] using newly measured $0f_{\frac{5}{2}}$ single particle energy [38].	14
2.8	Illustration of abrasion fission reaction between heavy ^{238}U projectile and light ^9Be target from [42].	18
2.9	Illustration of single nucleon knockout reaction between projectile and ^9Be target showing subsequent gamma-decay of excited product nucleus [42].	18
3.1	RIBF189 ^{238}U primary beam acceleration scheme showing ECRIS ion source, RILAC, RRC, fRC, IRC and SRC cyclotrons [49].	20
3.2	Illustration of BigRIPS and ZeroDegree magnetic fragment separators illustrating primary and secondary targets, PPAC, Music, Plastic scintillator and HiCARI detectors. Edited version of diagram from [51].	20

3.3	Diagram of PPAC showing charged anode/cathode plates enclosing ionization gas volume connected to delay line [53].	22
3.4	T_{sum} histogram for BigRIPS F3 PPACs demonstrating BigRIPS-ZeroDegree background suppression selection. Red interval showing suppression of inconsistently detected ion events.	22
3.5	Cross-sectional diagram of tilted electrode gas ionization chamber MUSIC detector used by BigRIPS and ZeroDegree. Diagram from [54].	23
3.6	Histogram showing F3 plastic scintillator $\ln \frac{q_1}{q_2}$ to $t_2 - t_1$ correlation. Labelled with graphical selection on correlation of positions reconstructed using timings and charge methods.	25
3.7	BigRIPS $ZvsA/Q$ histogram labelled with incoming ^{130}Cd ions before application of correction coefficients.	25
3.8	BigRIPS $ZvsA/Q$ histogram labelled with incoming ^{130}Cd ions after application of correction coefficients.	26
3.9	$\Delta B\rho_{if}$ histogram demonstrating separation of ions that change charge state from between the dipole magnets before and after the F8 target and those that do not.	26
3.10	ZeroDegree $ZvsA/Q$ histogram showing ions that did not change charged state with labelled ^{130}Cd ions.	27
3.11	ZeroDegree $ZvsA/Q$ histogram showing electron pickup charge state channel with labelled ^{130}Cd ions.	27
3.12	ZeroDegree $ZvsA/Q$ histogram showing electron drop-off charge state channel with labelled ^{130}Cd ions.	28
3.13	Illustration Miniball HPGe crystal segmented into 6 sections surrounding a central core [59].	29
3.14	Picture of Miniball detector showing LN_2 Dewar which cool the HPGe crystals and parts of the electronics below [59].	30
3.15	Illustration of HiCARI Doppler reconstruction of ion trajectory through F8 PPACs to mid-target and reconstruction of gamma-ray emission angles from mid-target position and half-life delayed emission site.	31
3.16	Plot of DWEIKO computed ^{131}In ion nuclear absorption cross section as they penetrate 6mm ^9Be target and lose kinetic energy [62].	32
3.17	Plot of ^{131}In ions remaining un-absorbed in nuclear reactions as they penetrate 6mm ^9Be target. Absorption cross sections computed with DWEIKO [62].	32
3.18	Proposed angular, velocity and intrinsic energy contributions to total Doppler corrected energy uncertainty for Miniball (solid line) and tracking (dashed line) detectors. Edited version of figure in proposal from [106].	34
3.19	Reconstructed polar emission angle hits in tracking (red), Superclover (blue) and Miniball (green) from UCHiCARI simulation.	35

3.20 Residual energy between linear calibration of HiCARI raw channel energies and known ^{152}Eu source gamma-rays at 344 keV and 1408 keV for HiCARI HPGe crystals.	36
3.21 Comparison of experimental observed ^{152}Eu source gamma-ray energies (blue) to UChiCARI simulated ^{152}Eu source energies(red) demonstrating consistency of simulated gamma-ray energy peak positions and widths with experimental.	37
3.22 Absolute efficiency of HiCARI array measured as a function of gamma-ray energy for Miniball and superclover detectors as well as tracking detectors using the ^{60}Co and ^{152}Eu source data.	37
3.23 Absolute simulated HiCARI gamma-ray detection efficiency measured as a function of gamma-ray energy for the Miniball and superclover detectors combined and the tracking detectors from the UChiCARI simulations.	38
3.24 Combined Miniball and superclover absolute detection efficiency as a function of gamma-ray energy comparing experimentally measured detection efficiency from radioactive ^{152}Eu and ^{60}Co source data and UChiCARI simulations.	39
3.25 Tracking detector absolute detection efficiency as a function of gamma-ray energy comparing experimentally measured detection efficiency from radioactive ^{152}Eu and ^{60}Co source data and UChiCARI simulations.	39
3.26 Experimentally reconstructed rest-frame gamma-ray energy histogram showing ^{131}In , $J^\pi = \frac{3}{2}^-$ 988 keV gamma-decay energy alignment in Miniball (green), Superclover (blue) and tracking detector (red).	40
3.27 $^{131}\text{In} \rightarrow ^{131}\text{In}$ channel gamma-ray energy distribution showing tracking detector energies (red), Superclover energies (blue) and Miniball energies (green).	41
3.28 Reconstructed Miniball rest-frame gamma-ray energy distribution showing experimental energies (blue), simulated $^{131}\text{In} \frac{3}{2}^- \rightarrow \frac{1}{2}^-$ transition (purple) assuming a $T_{1/2} = 0.2\text{ps}$ half-life, fitted experimental background (green) and combined fit (red).	42
3.29 χ^2 Miniball histogram as a function of ^{131}In , $J^\pi = \frac{3}{2}^-$ UChiCARI simulation excitation energy and half-life fitted to experimental energy distribution. Labelled with χ^2 minimum (red).	43
3.30 χ^2 Superclover histogram as a function of ^{131}In , $J^\pi = \frac{3}{2}^-$ UChiCARI simulation excitation energy and half-life fitted to experimental energy distribution. Labelled with χ^2 minimum (red).	43
3.31 χ^2 tracking detector histogram as a function of ^{131}In , $J^\pi = \frac{3}{2}^-$ UChiCARI simulation excitation energy and half-life fitted to experimental energy distribution. Labelled with χ^2 minimum (red).	44

3.32	χ^2 goodness-of-fit between experimental Doppler corrected ^{131}In gamma-ray energy distribution and combined fitted background and simulated ^{131}In energy distribution from UCHiCARI simulation as a function of longitudinal beamline position from central F8 HiCARI array target position.	45
3.33	χ^2 goodness-of-fit between experimental Doppler corrected ^{131}In gamma-ray energy distribution and combined fitted background and simulated ^{131}In energy distribution from UCHiCARI simulation as a function of average mid target velocity from reconstructed from measured after target velocity and LISE++ simulations. Tracking detector fit in red, Superclover fit in blue, Miniball fit in green.	45
3.34	Doppler corrected gamma-ray energy histogram for Miniball detectors (green), Superclovers (blue) and tracking detectors (red).	49
3.35	^{130}Cd level scheme constructed on the basis of theoretical calculations (left) and experimental observations of gamma-ray energy peaks (right).	50
3.36	^{130}Cd Doppler corrected gamma-ray energy distributions fitted with combined fitted-backgrounds and simulations of direct population of (2^+) (green), (4^+) (blue), (5^-) (yellow), (4^-) (purple) states for Superclover detectors.	51
3.37	^{130}Cd Doppler corrected gamma-ray energy distributions fitted with combined fitted-backgrounds and simulations of direct population of 2^+ (green), 4^+ (blue), 5^- (yellow), 4^- (purple) states for Miniball detectors.	52
3.38	^{130}Cd Doppler corrected gamma-ray energy distributions fitted with combined fitted-backgrounds and simulations of direct population of 2^+ (green), 4^+ (blue), 5^- (yellow), 4^- (purple) states for tracking detectors.	52
3.39	χ^2 Miniball fit histogram as a function of ^{130}Cd , $J^\pi = 4^-$ UCHiCARI simulation transition energy and half-life fitted to experimental energy distribution. Labelled with 90% confidence region (red) and χ^2 minimum (green).	53
3.40	χ^2 Superclover fit histogram as a function of ^{130}Cd , $J^\pi = 4^-$ UCHiCARI simulation transition energy and half-life fitted to experimental energy distribution. Labelled with 90% confidence region (red) and χ^2 minimum (green).	54
3.41	χ^2 tracking detector fit histogram as a function of ^{130}Cd , $J^\pi = 4^-$ UCHiCARI simulation transition energy and half-life fitted to experimental energy distribution. Labelled with 90% confidence region (red) and χ^2 minimum (green).	54
3.42	χ^2 (2^+) energy half-life matrix for fit of simulated ^{130}Cd UCHiCARI Doppler corrected energy distribution to experimental energy distribution. Labelled with 90% confidence region (red) and χ^2 minimum (green).	56

3.43	Proposed ^{130}Cd level scheme including excitation energies for (2^+) , (4^+) , (6^+) , (8^+) states from previous experiment [33]. Excitation energies for (4^-) , (5^-) states and (2^+) , (4^+) , (4^-) , (5^-) half-lives from averaged solutions in table 3.4. Unobserved 166 keV $(5^-) \rightarrow (6^+)$ transition labelled in red.	58
4.1	Plot of atomic number and atomic mass of beam species available for study in HISPEC experiments coloured by achievable beam intensity [83]	63
4.2	Single and multi step Coulomb projectile excitation cross section of ^{74}Zn on a ^{208}Pb target. Modified version of plot from [86].	64
4.3	Illustration of SDB experiment including degrader (blue), two emissive foils (black), from which secondary electrons and knocked into tracking detectors (red) as well as DSSSD $\Delta E - E$ telescope (green), target (gold) and a AGATA crystal (purple). Gamma-ray emission angle between ion scattering angle from target into DSSSD and AGATA gamma-ray hit position.	64
4.4	Geant4 Visualisation of HISPEC SDB Experiment Geometry including AGATA (red, blue, green), the thin foils (red), wire grids (black), target (gold) and DSSSD array (green) without vacuum chamber. Thin foils brought closer together (57cm separation) for purposes of illustration.	73
4.5	Geant4 Visualisation of HISPEC SDB Experiment Geometry including AGATA (red, blue, green) and vacuum chamber (grey) enclosing the thin MCP foils	74
4.6	Illustration of MCP detection process. Incident ion enters foil left, knocking out secondary electron. Electron is accelerated by electrostatic wire grid into the diagonal drift volume. Magnet Array along drift volume (not illustrated) provides longitudinal magnetic field along drift volume causing electron to spiral in helical pattern towards surface of the MCP where it is detected.	74
4.7	CAD drawing of MCP detector system including black magnet array blocks along drift volume length Horizontal volume connected to main SDB vacuum chamber with flanges and encloses a SDB emissive foil. CAD drawing courtesy of University of Koeln workshop.	75
4.8	Single 2^+ and multi-step 4^+ projectile Coulomb excitation cross sections for ^{64}Ni on ^{197}Au target. Low energy Safe Coulex cross-sections calculated with CLX [101]. High energy cross sections calculated with DWEIKO [63]. Intermediate region is a linear interpolated between the CLX and DWEIKO cross sections.	76
4.9	Plot of number of sub-coulomb barrier post-degrader ions for chosen Al SDB degrader thickness from MOCADI Simulation of the slowing of an incident 233MeV/u ^{64}Ni primary beam to its Coulomb barrier in ^{197}Au at 4.22 MeV/u.	77

4.10	Histogram of post-degrader beam energy distribution resulting from the slowing of 233MeV/u ^{64}Ni beam in a 3558.3 mg/cm ² simulated in MOCADI simulation.	78
4.11	Spacial distribution of post-degrader ^{64}Ni ions from MOCADI simulation.	79
4.12	Angular distribution of post-degrader ^{64}Ni ions obtained from MOCADI simulation.	79
4.13	Pie chart illustrating the fractions of ions that are fully stopped in the SDB degrader, that underwent nuclear reactions becoming ions other than ^{64}Ni and the remaining ^{64}Ni primary beam fraction. Distribution produced in SuperFRS MOCADI simulation of the slowing of 233 MeV/u ^{64}Ni beam to Coluomb barrier energies in 3888 mg/cm ² target.	80
4.14	X vs Y histogram of ^{64}Ni beam spread extrapolated from degrader to final SDB DSSSD produced in Geant4 simulation.	81
4.15	Energy deposition curve of ^{64}Ni ions across range of kinetic energies in 20um ^{28}Si target block labelled with 1.8 MeV/u punch through point.	82
4.16	Energy deposition curve of ^{64}Ni ions across range of kinetic energies in 2um ^{197}Au target block labelled with 0.12 MeV/u punch through point.	82
4.17	HPGe gamma-ray energy distribution with characteristic photopeak, Compton edge and escape peaks from [57].	83
4.18	Histogram of energy deposition of 1346 keV gamma-ray in Ge target block demonstrating full energy peak and Compton edge structures.	84
4.19	Polar scattering angle of ^{64}Ni ions from 2um ^{197}Au target into DSSSD array. DSSSD Detection efficiency drops at transverse angles along target and angles backwards angles labelled in blue and green respectively.	85
4.20	Number of incoming ions that hit target (blue) and number of excited ions that are captured in DSSSD array as a function of incoming hole radius (red).	86
4.21	Number of excited ions that are captured by DSSSD array as a function of outgoing hole radius.	87
4.22	Geant4 Visualisation of spherical DSSSD geometry. Thick DSSSD layer in blue, thin DSSSD layer in green and target in red.	90
4.23	Geant4 Visualisation of barrel DSSSD geometry. Thick DSSSD layer in blue, thin DSSSD layer in green and target in red.	90
4.24	Geant4 Visualisation of box DSSSD geometry. Thick DSSSD layer in blue, thin DSSSD layer in green and target in red.	91
4.25	Illustration of thin DSSSD thickness traversal reconstruction in spherical case.	92
4.26	Simulated energy deposited by ions in thin DSSSD against total energy collected in DSSSD layers demonstrating $\Delta E - E$ separation of black Ni ions, red Co ions and blue Fe ions.	93

4.27	Simulated invariant mass reconstruction from MCP velocity extrapolation and DSSSD energy deposition showing separation between ^{64}Ni , ^{63}Ni and ^{62}Co isotope masses.	93
4.28	Doppler corrected gamma-ray energy distribution reconstructed of excitation of ^{64}Ni to 2^+ and 4^+ states showing reconstructed 1346 keV and 1264 keV $2^+ \rightarrow 0^+$ and $4^+ \rightarrow 2^+$ transitions. Rest-frame gamma-ray energy distributions reconstructed assuming perfect MCP and DSSSD detector resolutions and realistic AGATA energy and position resolutions [92]. . .	94
4.29	Simulated HPGe background energy extracted from 2021 HISPEC SDB experiment.	95
4.30	HPGe timing distribution demonstrating time separation of degrader background from ion-correlated signal.	96
4.31	Histogram of reconstructed invariant mass of post-degrader isotopes with (black) and without (red) intrinsic MCP position and timing and DSSSD energy resolutions from Geant4 simulation with enhanced post-degrader secondary product production cross sections demonstrating separation of isotopes.	97
4.32	Simulated energy deposited by ions in thin DSSSD against total energy collected in DSSSD layers demonstrating deltaE-E separation of black Ni ions, red Co ions and blue Fe ions with 1.5% DSSSD energy resolution. .	98
4.33	Simulated Doppler corrected gamma-ray energy distribution showing reconstruction of 1346 keV $2^+ \rightarrow 0^+$ transition with simulated SDB detector resolutions (black) and without simulated detector resolutions (red).	99
4.34	Simulated Doppler corrected gamma-ray energy distribution showing reconstruction of 1346 keV transition from first 2^+ excited state of ^{64}Ni using $\Delta E - E$ and invariant mass reconstruction, scattering angle selection and HPGe background timing suppression.	99

List of Tables

2.1	Table of allowable J configurations for a pair of like nucleons within $j = 9/2$ and $j' = 9/2$ orbitals made up of $M(m, m')$ unique magnetic substate configurations. Only positive total M values are shown as the table is symmetric for $M < 0$. Based on table from [29].	11
2.2	Table of theoretical excitation energies computed for ^{130}Cd with Oxbash (left). Experimentally determined excitation energies from [33] assigned to $J^\pi = (2^+), (4^+), (6^+), (8^+)$ states connected by $2^+ \rightarrow 0^+, 4^+ \rightarrow 2^+, 6^+ \rightarrow 4^+, 8^+ \rightarrow 6^+$ transitions also summarised.	14
3.1	Table of ^{131}In and ^{130}Cd ions produced in proton knockout reactions in the secondary HiCARI target.	28
3.2	Table of χ^2 minima showing sensitivity of fitting solutions to average mid-target velocity and target position.	44
3.3	Table of energy/half-life χ^2 minima with 1 parameter fitting uncertainty limits and averaged values.	47
3.4	Table of energy/half-life χ^2 minima with 1 parameter fitting uncertainty limits. ^a excitation energies from [33].	55
3.5	Table of experimental ^{130}Cd reduced transition probabilities based on proposed level scheme in figure 3.45.	59
3.6	Table of theoretical ^{130}Cd reduced transition probabilities calculated in Oxbash [34].	59
4.1	Table of estimated SDB MCP and DSSSD intrinsic detector performance requirements [87][96]. Achieved AGATA intrinsic energy and position reconstruction performance from [92].	71
4.2	Table of spacial and angular spread of 233 MeV/u ^{64}Ni ions after 3558 mg/cm ² Al degrader in MOCADI simulation.	78
4.3	Table of upper limits of pile-up rates that 3.125 mm and 0.625 mm width strips that are hit with ions scattering at >10 deg in the target into spherically arranged 5x5 cm DSSSDs encounter in Geant4 SDB simulations as they are exposed to different beam intensities.	89

4.4	Table of upper limits of pile-up rates that 3.125 mm and 0.625 mm width strips that are hit with ions scattering at <10 deg in the target into spherically arranged 5x5 cm DSSSDs encounter in Geant4 SDB simulations as they are exposed to different beam intensities.	89
4.5	Table of simulated detector resolutions used in Geant4 simulation study of minimum necessary detector for sufficiently precise Doppler correction and particle identification. AGATA gamma-ray energy and position resolutions from previous experiment [92], timing resolution estimated from [57].	100

Chapter 1

Introduction

Physics is the empirical study of matter. Its structure, motions and behaviours are observed experimentally and described theoretically according to natural laws. No singular model successfully describing all fundamental forces through which matter has been observed to interact has yet been constructed. The success of the mostly widely accepted physical models are limited in scope and scale, disagreeing on even the most fundamental axiomatic assumptions regarding the nature of space and time [1]. The model with the grandest of scope is the standard model, failing only to describe the gravitation of matter the effect of which is small on the quantum scale. The standard model is a quantum field theory wherein matter is composed of excitations of underlying and fundamental electro-weak and chromodynamic fields called quanta and relies on many bosonic and fermionic degrees of freedom to describe these fields [2]. Standard model calculations predicting the properties of nuclear systems are limited in their ability to describe heavy nuclear systems because of the necessary complexity inherited by the introduction of these many degrees of freedom [3]. A patchwork of phenomenological shell models based on realistic interactions informed by experimental results have however demonstrated success in describing heavy nuclear systems throughout the nuclear chart. Stable nuclei within the valley of stability are easily experimentally accessed and are mostly successfully theoretically described, but only in the last half-century have particularly exotic unstable nuclei become accessible for study at Rare Isotope Beam (RIB) facilities. In RIB experiments it has been found that nuclear shell structure evolves towards the extremes of isospin, single particle energies shift becoming effective single particles and new nuclear magic numbers appear due to the reordering of nuclear orbitals [5][6][7]. The study of the exotic nuclei and their decays are of special importance to understanding the astrophysical r-process nucleosynthesis. r-process reaction rates and nuclear abundance calculations diverge on their paths through the unknown extremes of the neutron rich region [8]. Experimental studies of neutron rich nuclei at rare isotope beam facilities can therefore improve both our understanding of exotic nuclear structure and r-process nucleosynthesis. In this thesis a study of the low-lying excited states of ^{130}Cd in an in-flight gamma-ray decay spectroscopy experiment are presented. This includes the observation of two new electromagnetic

transitions tentatively assigned to $(4^-) \rightarrow (5^-)$ and $(5^-) \rightarrow (4^+)$ transitions between (4^-) , (4^+) and (5^-) excited states. From these transitions the excitation energies of tentatively assigned (4^-) and (5^-) states were newly deduced as well as the first determination of the ^{130}Cd $(2^+) \rightarrow (0^+)$, $(4^+) \rightarrow (2^+)$, $(4^-) \rightarrow (4^+)$ and $(4^-) \rightarrow (5^-)$ transition strengths. Simulations and developments for High-resolution Inflight SPECTroscopy (HISPEC) Slowed Down Beam (SDB) experiments aimed at nuclear spectroscopy of exotic nuclei in multi-step Coulomb excitation reactions are also presented [9]. On the basis of MOCADI ion-transport and geometric Geant4 simulations the feasibility of HISPEC SDB experiments at FAIR with the Advanced Gamma Tracking Array (AGATA) and the SuperFRS (Super-conducting FRagment Separator) are studied [10][11][12]. Possible SDB detector geometries with necessitated detector performances are evaluated.

Chapter 2

Physics background

2.1 Stellar nucleosynthesis

Solar and stellar elemental abundances obtained with the well established absorption-line spectroscopy technique suggest the distribution of elements within stellar systems throughout the universe favours lighter elements [13][14]. The predominance of the abundance of these light elements is shown in figure 2.1.

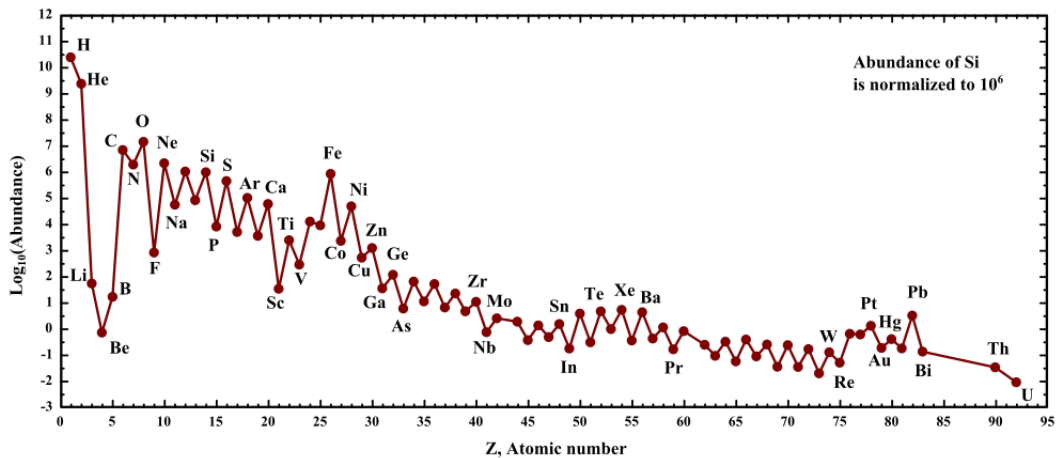


Figure 2.1: Solar nuclear abundance as a function of atomic number [14].

In 1946 Fred Hoyle proposed that of these elements, nuclei as heavy as iron could be produced in a series of fusion reactions facilitated by the extreme heat and pressure within the cores of stars [15]. However as shown in figure 2.2 the binding energy per nucleon of elements as a function of their atomic mass reaches a maximum at iron [16]. Stellar fusion reactions forming less strongly bound nuclear systems are not energetically favoured to occur beyond the iron peak. The stellar fusion hypothesis can therefore only explain the origin of elements up to the iron-nickel peak [17].

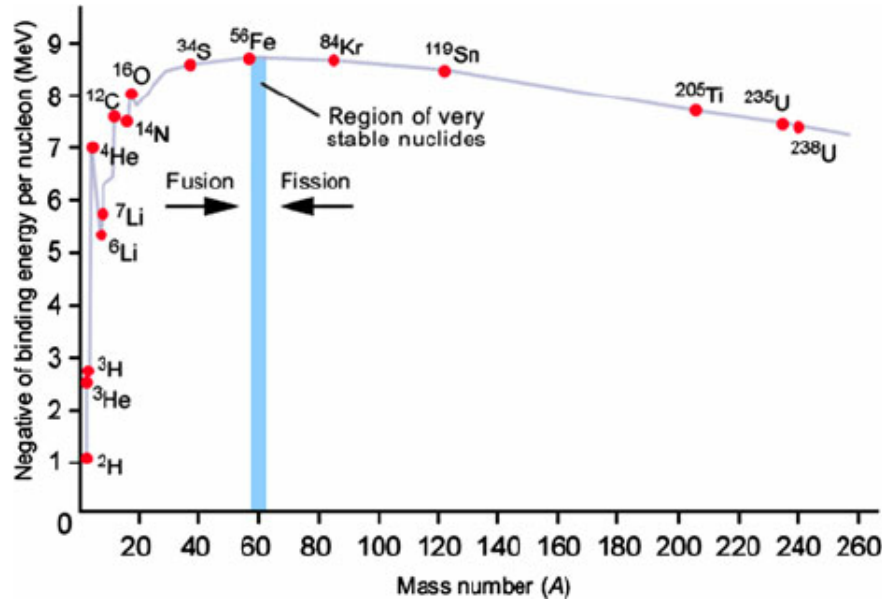


Figure 2.2: Binding energy per nucleon for elements as a function of atomic mass. Annotated with the iron peak, showing the point at which fusion and fission reactions are energetically favoured [16].

2.2 R-process

In their 1957 B^2FH paper Fred Hoyle, William Fowler and Margret and Geoffrey Burbidge expand upon Hoyle's original stellar nucleosynthesis theory identifying that neutron capture reactions toward heavier and less stable isotopes followed by beta-decays could produce the remaining heavier elements [18]. These reactions would necessarily occur within environments with high neutron flux ($10^5 - 10^{11}$ neutrons per cm^2) in order to facilitate single neutron captures in the slow s-process or extreme neutron flux (10^{22} neutrons per cm^2) in the case of successive neutron captures in rapid r-process nucleosynthesis [18][19]. The astrophysical sites with sufficient neutron flux for the r-process to occur are still debated but candidate examples include the the prompt explosions of ONeMg stellar cores, accretion disk jets and during the outflow of baryonic matter as nascent neutron stars cool and emit neutrino winds [20][21][22][23][24].

2.2.1 R-process path

The path of nuclei as they increase in proton and neutron number along an r-process path is illustrated in figure 2.3 [20] As they gain neutrons becoming increasingly unstable and so when the neutron flux stops, they cease gaining neutrons and instead eventually decay via β^- decay, α emission or fission towards stability forming stable isotopes of elements as heavy as Th, U and Pu. Figure 2.3 shows there are vertical sections in the r-process path at $N=82$ and $N=126$ neutron number. The neutron separation energy for these isotopes is so low that the r-process halts and β^- decays towards stability are favoured. If the neutron flux is sustained over the β^- decay time scale these β^- decay are followed by further neutron captures and β^- decays along the vertical paths. As

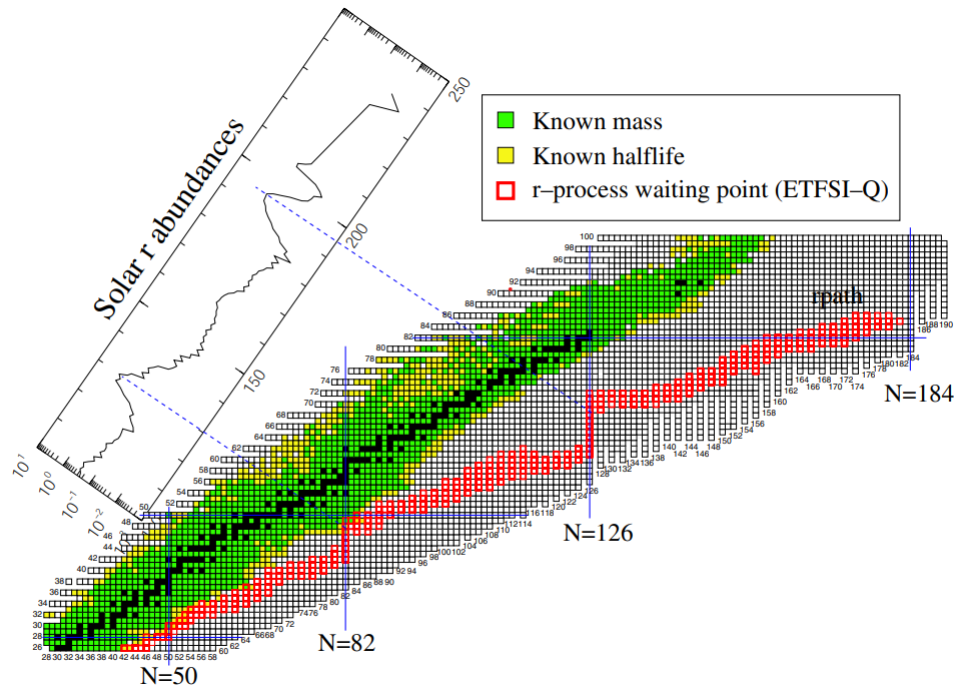


Figure 2.3: Plot of nuclear proton number against neutron number illustrating horizontal r -process neutron capture path from ^{56}Fe seed nuclei and vertical path through waiting point nuclei [20]

shown in the solar r -process abundance plot in figure 2.3 at these waiting points there are nuclear abundance peaks connected to the bottle-necking of the r -process. The enhanced stability of these *magic numbers* of nucleons persists to $N = 2, 8, 20, 28, 50, 72, 126$ and 184 combinations of protons and neutrons [17]. As is shown in the following section these magic numbers arise due to the way that nucleons in many body nuclear systems can interact to form discrete energy levels.

2.3 The nuclear shell model

The standard model of particle physics is widely considered to be the most successful theory for describing fundamental electromagnetic, weak and strong interactions. The application of quantum field theory to the prediction of the properties of heavy, many body nuclear systems such as magic numbers is troublesome however. The many postulated degrees of freedom within the standard model results in descriptions of large nuclear systems of many quanta involving currently incalculably large numbers of interaction terms [25]. In 1963 Mayer and Jensen showed the properties and structure of these heavier nuclei can be reproduced by approximating the many interactions between nucleons into an average nuclear potential for the whole nucleus [26][27]. In the shell model, nucleons orbit within this average nuclear potential with discrete energy levels depending on the principle quantum number n , orbital angular momentum l and total angular momentum j they occupy depending upon their spin s with $j = l + s$. In accordance with the Pauli-exclusion principle no two identical fermions in a given

system can occupy the same quantum numbers and therefore nucleons fill unique and discrete energy levels which cluster into shells of increasing energy [17]. In this section the filling of nucleons characterised by combinations of quantum numbers into these energy levels is presented based on a section from [28]. First proceeding by analysis of the independent motion of particles within an average nuclear potential. Then continuing by separating this independent component from the total to leave a residual nucleon-nucleon contribution. This is finally followed by an description of the formation of single-particle and two-particle states with an example shell model calculation for the ^{130}Cd case.

2.3.1 Independent particle motion

Consider first the single-particle wave function $\phi_a(r)$ for a single nucleon within a nucleus characterised by a combination of quantum numbers a at a particle coordinate r within a single particle potential $U(r)$ with kinetic-energy operator T that solves the Schrödinger equation

$$[T + U(r)]\phi_a(r) = e_a\phi_a(r) \quad (2.1)$$

with single-particle energy e_a [28]. The Hamiltonian for the independent motion of nucleons is then given as the sum of $k = 1, 2, 3 \dots A$ total nucleons within the nucleus with

$$H^0 = \sum_k^A [T(k) + U(k)] \quad (2.2)$$

The eigenfunctions for this Hamiltonian are then obtained as the product of the single particle wave functions

$$\Phi_{a_1, a_2 \dots a_A} = \prod_{k=1}^A \phi_{a_k}(r(k)) \quad (2.3)$$

with eigenenergies

$$E^0 = \sum_{k=1}^A e_{a_k} \quad (2.4)$$

The full Hamiltonian H meanwhile of a nucleus consisting of $k = 1 \dots A$ nucleons with wave function ψ could consist of the sum of $T(k)$ and two-particle interaction $\sum_{k < l} W(k, l)$ terms solving the Schrödinger equation

$$H\psi(1, 2 \dots A) = \left[\sum_{k=1}^A T(k) + \sum_{1=k < l}^A W(k, l) \right] \psi(1, 2 \dots A) = E\psi(1, 2 \dots A) \quad (2.5)$$

By introducing the single-particle potential $U(r)$, the full Hamiltonian can then be split into a H^0 term defining the independent-particle motion of individual nucleons within the nucleus and a second H^1 *residual interaction* term reflecting the fact that particles do not orbit completely independently and that there are in fact residual nucleon-nucleon interaction occurring in addition to this independent motion [28]

$$H = \sum_{k=1}^A [T(k) + U(k)] + \left[\sum_{1=k < l}^A W(k, l) - \sum_{k=1}^A U(k) \right] = H^0 + H^1 \quad (2.6)$$

By splitting the Hamiltonian into these independent and residual components, each can be considered separately and the formation of single and two-particle states can be separately considered.

Single-particle states

The independent-particle component of the full Hamiltonian in equation 2.6 is often described with a centrally acting potential [28]. One such choice is an isotropic harmonic-oscillator potential

$$U(r) = \frac{1}{2}M\omega^2r^2 \quad (2.7)$$

where M is the mass of a nucleon, $\hbar\omega$ is a quantum of energy for the harmonic oscillator and r is the distance from the coordinate origin [28]. The Schrödinger equation for a nucleon within this potential is

$$H^0\phi(r) = E^0\phi(r) \quad (2.8)$$

with

$$H^0 = T + U = \frac{p^2}{2M} + \frac{1}{2}M\omega^2r^2 \quad (2.9)$$

Converting to spherical harmonics, the eigenfunctions for equation 2.8 are

$$\phi_{nlm} = R_{nl}(r)Y_{lm}(\theta\phi) \quad (2.10)$$

For each unique combination of quantum numbers there is a solution of the second order differential equation

$$H^0\phi(r) = \frac{1}{2}\hbar\omega \left[\frac{\hbar}{M\omega} \nabla^2 + \frac{M\omega}{\hbar} r^2 \right] \phi(r) = E_{nl}^0\phi(r) \quad (2.11)$$

with eigenvalues

$$E_{nl}^0 = \left(2n + l + \frac{1}{2} \right) \hbar\omega = \left(N + \frac{3}{2} \right) \hbar\omega \quad (2.12)$$

where N is the total number of oscillator quanta excited with $N = 2(n - 1) + l$ [28]. The spacing of the energy states obtained with the harmonic oscillator are illustrated in figure 2.4 (a). The r^2 dependence of the quantum harmonic oscillator inaccurately predicts that the strength of the potential grows infinitely from the center [28]. In order to better reproduce experimentally obtained single-particle energies more realistic potentials such as the Woods-Saxon potential may instead be relied upon which approaches a finite value in this limit with

$$V(r) = \frac{V_0}{1 + \exp(r - R/a)} \quad (2.13)$$

where typical values for the nuclear skin thickness a and the nuclear potential strength V_0 are $a \sim 0.5\text{fm}$ and $V_0 \sim 50\text{MeV}$. R is the nuclear radius depending upon the atomic mass with $R = r_0A^{\frac{1}{3}}$ with a radial constant of $r_0 = 1.25 \text{ fm}$ [28][29]. A schematic representation of the spacing of the Woods-Saxon splitting into single particle energy

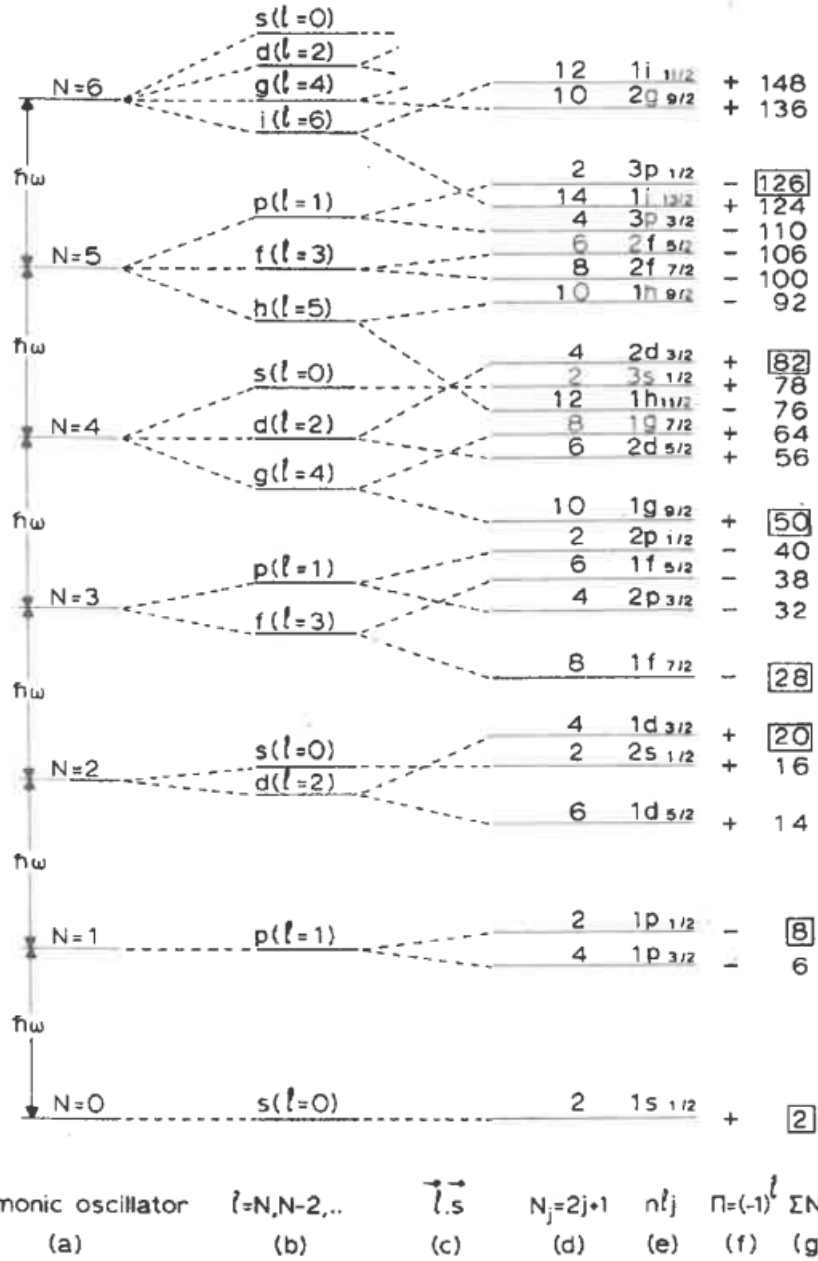


Figure 2.4: Schematic representation of (a) spacing of single particle energy levels in a harmonic oscillator for each N, (b) orbital angular momentum l splitting in a Woods-Saxon potential and (c) spin-orbit splitting for orbitals with j total angular momenta. These levels increase vertically in energy and are labelled in (e) with each n l j substate, (f) parity and (g) total number of occupying nucleon [20].

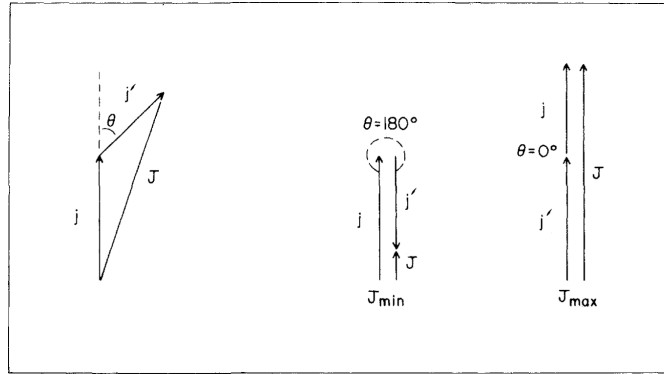


Figure 2.5: Illustration of coupling between nucleons in j and j' orbitals forming J total angular momentum states. Parallel and anti-parallel (j, j') projections showing maximum and minimum J states respectively. Modified figure from [27].

levels is shown in figure 2.4 (b) while spin-orbit splitting is represented in (c). In the (d) section of figure 2.4 the total number of nucleons occupying m_j substates in each j orbital is illustrated while (e) illustrates the form of the spectroscopic notation for each nl_j substate with $l = (0, 1, 2, 3, 4, 5, 6) = (s, p, d, f, g, h, i)$. Section (f) of figure 2.4 shows the parity $\pi = (+, -)$ of the single particle state with $\pi = (-1)^l$ and (g) counts the number of nucleons at the closing of each shell. One of the greatest successes of the shell model is this prediction of large jumps in energy between these $N = 2, 8, 20, 28, 50, 82$ and 126 *magic numbers* as magic nuclei are indeed experimentally observed to have particularly strong binding energy at these combinations of nucleons [21][22][23]. In recent decades ab-initio derivations of this nuclear potential from realistic QCD nuclear forces have been constructed however phenomenological adjustments and or purely phenomenological models are still generally relied upon to successfully describe nuclei across the nuclear chart [29][30].

Residual interaction

Nucleons do not however orbit completely independently of one another within the average potential [28]. One contribution to this residual interaction is when two nucleons interact with one another, coupling to form two particle states. Consider for example two orbiting nucleons with (j, m) and (j', m') total angular momenta and magnetic substate. When the two nucleons couple they can form a two-particle state with angular momentum J . As illustrated in figure 2.5, there are many ways differently aligned nucleons may couple, with the sum of their magnetic substates $M = m + m'$ maximised for parallel (m, m') combinations and minimised for anti-parallel combinations. In the case of like (isospin $T = 0$) nucleon pairs such as a like nucleon pair in $j = 9/2$ and $j' = 9/2$ orbitals, $m = m'$ configurations are not possible meaning J is restricted to $J = 0^+, 2^+, 4^+, 6^+, 8^+$ even pairs made up of unique $M(m, m')$ combinations such as is in table 2.1 [29].

$j = 9/2$ m	$j' = 9/2$ m'	M	J
9/2	7/2	8	8
9/2	5/2	7	8
9/2	3/2	6	8
9/2	1/2	5	8
9/2	-1/2	4	8
9/2	-3/2	3	8
9/2	-5/2	2	8
9/2	-7/2	1	8
9/2	-9/2	0	8
7/2	5/2	6	6
7/2	3/2	5	6
7/2	1/2	4	6
7/2	-1/2	3	6
7/2	-3/2	2	6
7/2	-5/2	1	6
7/2	-7/2	0	6
5/2	3/2	4	4
5/2	1/2	3	4
5/2	-1/2	2	4
5/2	-3/2	1	4
5/2	-5/2	0	4
3/2	1/2	2	2
3/2	-1/2	1	2
3/2	-3/2	0	0
1/2	-1/2	0	0

Table 2.1: Table of allowable J configurations for a pair of like nucleons within $j = 9/2$ and $j' = 9/2$ orbitals made up of $M(m, m')$ unique magnetic substate configurations. Only positive total M values are shown as the table is symmetric for $M < 0$. Based on table from [29].

2.3.2 Shell model calculations

Computing codes such as Oxbash and NushellX are designed to compute the properties of nuclear systems with the shell model [31][32]. In these codes an inert nuclear core is specified and the interaction of a selected range of valence particles (or holes) orbiting this core forms a model-space within which nucleon-nucleon interactions in the presence of the core are computed. The properties of states formed by the interaction of pairs of nucleons with user input single particle energies are then computed using a table of user input two-body matrix elements describing the strength of the interaction for each interacting pair of nucleons within the model space with wave functions $|I_1\rangle$ and $|I_2\rangle$ depending upon the quantum numbers of each state $I(n, l, j)$

$$\langle I_1 | H_{TB} | I_2 \rangle \quad (2.14)$$

2.3.3 The doubly magic ^{132}Sn region

Figure 2.6 shows r-process abundances computed using different assumptions about the nature of N=82 isotones. In the solid black line a pronounced shell gap at the N=82 neutron shell closure for N=82 isotones is assumed. As shown in figure 2.4, this results in solar r-process abundance dips before the $N \sim 130, 195$ mass peaks. The solid grey line however assumes a reduced ("quenched") shell gap and consequently the grey lines better reproduce the experimentally observed solar abundances. In a gamma-spectroscopy experiment studying the energies of gamma-rays emitted in transitions between the excited states of ^{130}Cd no evidence of shell quenching was found [33]. This does however demonstrate the sensitivity of r-process abundances to the nuclear structure of N=82 isotones in the region of ^{132}Sn [20]. The nuclear structure of isotopes in the doubly magic ^{132}Sn mass region has still not been extensively studied however, including many of these N=82 isotones. As is demonstrated in figure 2.6 this can limit precision of r-process models which rely on nuclear structure inputs to predict nuclear abundances. This makes the study of isotopes surrounding ^{132}Sn a particularly exciting cases to acquire nuclear structure information for and to test nuclear structure models in. In the case of ^{130}Cd only the excitation energy of yrast $J^\pi = (2^+), (4^+), (6^+), (8^+)$ states have been studied [8][33]. In the 2007 isomer spectroscopy experiment, 1325, 539, 138 and 128 keV energy transitions were observed and were tentatively assigned to transitions between $J^\pi = (2^+), (4^+), (6^+), (8^+)$ states respectively [33].

Shell model calculations for ^{130}Cd

Using the single particle energies illustrated in figure 2.7 the excitation energies of the excited states of ^{130}Cd were calculated in Oxbash [34]. The Na22 interaction first applied in 2016 to predict the excited states of ^{130}Cd was used in this calculation predicting the excitations energies of $J^\pi = 2^+, 4^+, 6^+, 5^-, 8^+, 4^-$ for $\pi(g9/2)$ and $\pi(p1/2)$ proton orbitals [33]. These excitation energies are summarised in table 2.2 along with the experimentally obtained $J^\pi = (2^+), (4^+), (6^+), (8^+)$ excitation energies [33]. In the GSI

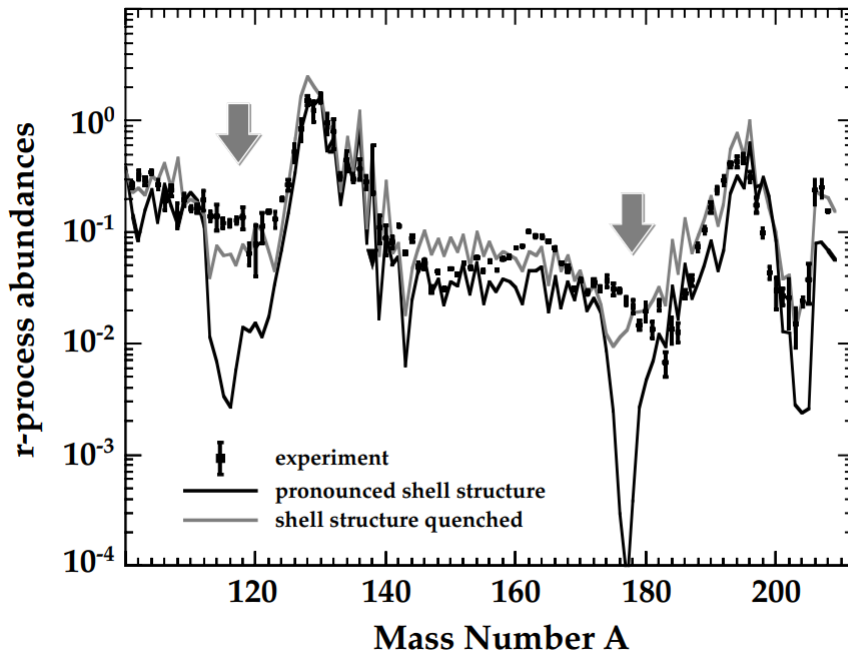


Figure 2.6: Solar r -process abundance distributions compared to two r -process calculations. Black line showing the assumption of a pronounced d

isomer spectroscopy experiment ^{130}Cd ions were produced in abrasion fission reactions and transported through the 72m long FRagment Separator (FRS) from the primary production target to a passive stopper for implantation [35][36]. Decays from directly populated short lived states are therefore unlikely to have been observed as these states decay before they reach the passive stopper around which gamma-ray detectors were positioned. After implantation the cascades of decays from long lived isomeric states were however observed and the $(8^+) \rightarrow (6^+) \rightarrow (4^+)$ transition sequence was fitted to a single decay exponential $\tau_{\frac{1}{2}} = 220(30)$. If the 5^- and 4^- states predicted by the shell model calculations were initially populated in this experiment it is possible these states were short enough lived that the gamma-decays of the 5^- and 4^- states may have occurred before the excited nuclei could be transported into sufficient proximity to be detected in the present gamma-ray detectors. As the theoretical calculations suggest the existence of the 5^- and 4^- states and the previous isomer spectroscopy experiment does not exclude the possibility that they are short lived, it is possible that they might be observed in an in-flight gamma-spectroscopy experiment producing excited ^{130}Cd nuclei in the same manner but observing their in-flight decays shortly after they are produced. As expanded upon in later sections an in-flight gamma-spectroscopy experiment also has the advantage that the previously unmeasured transition strengths of these excited states can be extracted from analysis of the Doppler shifting of detected gamma-ray energies.

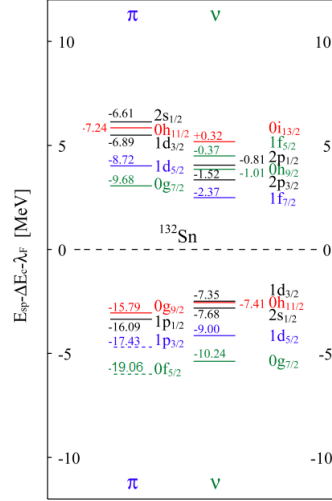


Figure 2.7: Illustration of single particle or hole proton π and neutron ν energies for ^{132}Sn . Updated version of plot from [37] using newly measured $0f_{7/2}$ single particle energy [38].

J^π	Theoretical E_x [MeV]	Experimental E_x [MeV]
0^+	0.0	0.0
2^+	1.316	1.325
4^+	1.825	1.864
6^+	1.998	1.992
5^-	2.075	-
8^+	2.097	2.130
4^-	2.417	-

Table 2.2: Table of theoretical excitation energies computed for ^{130}Cd with Oxbash (left). Experimentally determined excitation energies from [33] assigned to $J^\pi = (2^+), (4^+), (6^+), (8^+)$ states connected by $2^+ \rightarrow 0^+, 4^+ \rightarrow 2^+, 6^+ \rightarrow 4^+, 8^+ \rightarrow 6^+$ transitions also summarised.

2.4 Electromagnetic transitions

As an excited nucleus transitions from a higher energy state to a low energy state it emits a gamma-ray equal in energy to the difference in the excitation energy of the states [17]. By detecting these gamma-rays the excitation energies of the excited states can be determined from their energies and the strengths of the transitions can be gleaned from the rate at which gamma-rays are observed [39].

2.4.1 Transition strengths

The rate at which transitions between nuclear states occurs depends upon the charge and current distribution within the nucleus [29] The function describing the resultant electromagnetic potential can be treated with a multipole expansion and separated for electric E and magnetic M transitions of λ order multipolarity. For a transition from a higher spin state $|I_1 M_1\rangle$ to a lower spin state $|I_2 M_2\rangle$ the *matrix element* with the electromagnetic transition multipole operator $\widehat{O}_{\lambda\mu}$ is

$$\langle I_2 M_2 | \widehat{O}_{\lambda\mu} | I_1 M_1 \rangle \quad (2.15)$$

With the Wigner Eckart theorem

$$\langle I_2 M_2 | \widehat{O}_{\lambda\mu} | I_1 M_1 \rangle = \frac{1}{\sqrt{2I_2 + 1}} \langle I_1 M_1 \lambda \mu | I_2 M_2 \rangle \langle I_2 | \widehat{O}_\lambda | I_1 \rangle \quad (2.16)$$

the matrix element for a transition can be separated into a *reduced matrix element* $\langle I_2 | \widehat{O}_\lambda | I_1 \rangle$ component describing the magnetic orientation of the states and a Clebsch-Gordan coefficient matrix $\langle I_1 M_1 \lambda \mu | I_2 M_2 \rangle$ describing the intrinsic strength of couplings between states of different orientations in spherical harmonics [29]. This reduced matrix element can be related to a reduced transition probability

$$B(O_\lambda; I_1 \rightarrow I_2) = \frac{1}{2I_1 + 1} |\langle I_2 | \widehat{O}_\lambda | I_1 \rangle|^2 \quad (2.17)$$

The reduced transition probability is a useful quantity to define because it can be related to an experimentally observable transition strength $T^{E\lambda}$ or $T^{M\lambda}$ for electric and magnetic transitions respectively [29].

$$T^{E\lambda} = \frac{8\pi(\lambda + 1)e^2 b^\lambda}{\lambda((2\lambda + 1)!!)^2 \hbar} \frac{E\lambda^{2\lambda+1}}{\hbar c} B(E\lambda) \downarrow \quad (2.18)$$

$$T^{M\lambda} = \frac{8\pi(\lambda + 1)\mu_N^2 b^{\lambda-1}}{\lambda((2\lambda + 1)!!)^2 \hbar} \frac{E\lambda^{2\lambda+1}}{\hbar c} B(M\lambda) \downarrow \quad (2.19)$$

where e is elementary charge 1.602×10^{19} C, b is a barn $1 \times 10^{-28} f m^2$ and μ_N^2 is the square of the nuclear magneton $1.59 \times 10^{-36} \text{ keV } cm^3$. By evaluating the first few transitions strengths for λ multipolarity one obtains

$$T(E1) = 1.59e10^{15} E_\gamma^3 B(E1) \quad (2.20)$$

$$T(E2) = 1.23e10^9 E_\gamma^5 B(E2) \quad (2.21)$$

$$T(E3) = 5.71e10^2 E_\gamma^7 B(E3) \quad (2.22)$$

$$T(M1) = 1.76e10^{13} E_\gamma^3 B(M1) \quad (2.23)$$

$$T(M2) = 1.36e10^7 E_\gamma^5 B(M2) \quad (2.24)$$

$$T(M3) = 6.31E_\gamma^7 B(M3) \quad (2.25)$$

Transition multipolarity and selection rules

With gamma-ray transition energy E_γ [29], multiple orders of the multipole expansion may contribute to possible electromagnetic transition modes. Whether a transition of a given multipolarity is allowed or forbidden depends on if the final and initial quantum numbers fulfill the selection rule

$$|I_1 - I_2| \leq L \leq I_1 + I_2 \quad (2.26)$$

where L is the change in the angular momentum $L = I_2 - I_1$ [29]. The parity π of a state depends upon the orbital angular momentum l forming it such that $\pi = (-1)^l$. Provided the selection rule in equation 2.26 is fulfilled, when the parity change $\Delta\pi$ for a transition is equal to -1 , E1, M2, E3, M4 alternating multipolarities are allowed. If $\Delta\pi = 1$ then M1, E2, M3, E4 multipolarities are allowed [29].

2.5 Coulomb Excitation

Coulomb excitation (Coulex) has historically been used as a tool to populate these excited states for study [39]. Coulex is the electromagnetic excitation of a nucleus in an inelastic collision with another nucleus. Coulex interactions are a particularly effective means to populate low-lying excited nuclear states for study because at Coulomb barrier kinetic energies these states are strongly populated and at sufficiently low kinetic energies Coulex reactions are well theoretically described enabling robust and model independent extraction of nuclear observables such as the deduction nuclear excitation energies and electromagnetic transition matrix elements from gamma-ray decay spectra [39]. Indeed the first nuclear gamma rays identified as originating from transitions between excited states populated in Coulomb excitations were recorded in proton induced reactions with light nuclei in 1952 [40].

2.5.1 Safe Coulex

The forces governing Coulex reactions are composed of an electromagnetic and a nuclear component [39] At projectile kinetic energies below the Cline-condition energy E_{cline} in equation 2.27 the nuclear surfaces cannot come within a 5 fm distance of one another

before the projectile is deflected and so the nuclear contribution to the excitation cross section is small and can therefore be safely neglected [39].

$$E_{cline} = 1.44 \frac{A_1 + A_2}{A_2} \cdot \frac{Z_1 Z_2}{1.25(A_1^{\frac{1}{3}} + A_2^{\frac{1}{3}}) + 5} \quad (2.27)$$

Here E_{cline} is the maximum kinetic energy for safe, electromagnetically dominated Coulex depending upon the atomic mass and number of the projectile (A_1, Z_1) and target (A_2, Z_2) [39]. The motion of the projectile traveling at a velocity v in the Coulomb field of the nucleus can be characterised by the Sommerfeld parameter

$$\eta = \frac{Z_1 Z_2 e^2}{4\pi\hbar v} \gg 1 \quad (2.28)$$

In Coulomb excitations at low kinetic energies η is much larger than one. This implies the kinematics of the inelastic Coulomb excitation collisions can be described classically [39].

2.5.2 Semi-classical approach

In the semi-classical description the differential cross section for Coulomb excitation from an initial $|I_i\rangle$ to an excited final state $|I_f\rangle$ is

$$\left(\frac{d\sigma}{d\Omega}\right)_f = \left(\frac{d\sigma}{d\Omega}\right)_{Ru} \cdot P_{if} \quad (2.29)$$

where $(d\sigma/d\Omega)_{Ru}$ is the Rutherford scattering cross section and the probability of a particular excitation from an initial state I_i to a final state I_f , P_{if} , is summed over all initial state magnetic substates M_i and summed over all final state magnetic substates M_f forming final state excitation amplitudes b_f [39].

$$P_{if} = (2I_i + 1)^{-1} \sum_{M_i M_f} |b_f|^2 \quad (2.30)$$

2.6 Production of rare isotope beams

In order to produce rare isotope beams for study in gamma-spectroscopy experiments and in the case of Coulex experiments for excitation, RIB facilities can employ abrasion-fission reactions with stable beams [36]. Alternatively a combination of abrasion fission reactions and nucleon knockout reactions directly exciting nuclear states can be employed [41].

2.6.1 Abrasion fission

In abrasion-fission reactions heavy stable beams such as ^{238}U are impinged at high energies on light targets such as ^9Be . As illustrated in figure 2.8, in an abrasion-fission reaction part of the incoming heavy projectile breaks off from the original nucleus in

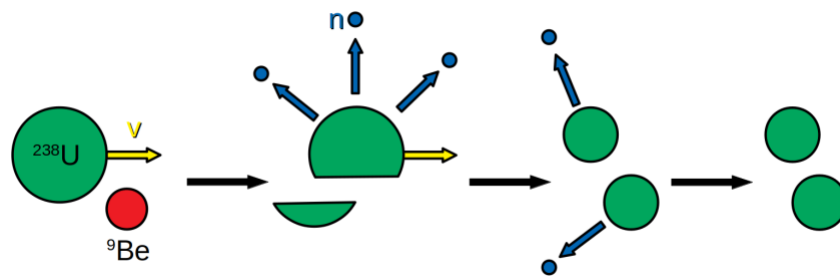


Figure 2.8: Illustration of abrasion fission reaction between heavy ^{238}U projectile and light ^9Be target from [42].

a collision with the target and gains excitation energy. Depending upon the resulting reaction product and its excitation energy, neutron evaporation may then occur before an in-flight fission into lighter mass residues occurs. These residues can themselves then undergo neutron evaporation until more stable products remain [36].

2.6.2 Knockout reactions

In a knockout reaction a projectile is similarly impinged on a light target and only a few nucleons are removed from the nucleus leaving the remaining nucleus in an excited state. As illustrated in the single-nucleon knockout reaction in figure 2.9, the excited nucleus can then gamma-decay. In in-flight gamma spectroscopy experiments gamma-rays emitted in in-flight transitions between the excited states of the nucleus carrying nuclear structure information are studied [41].

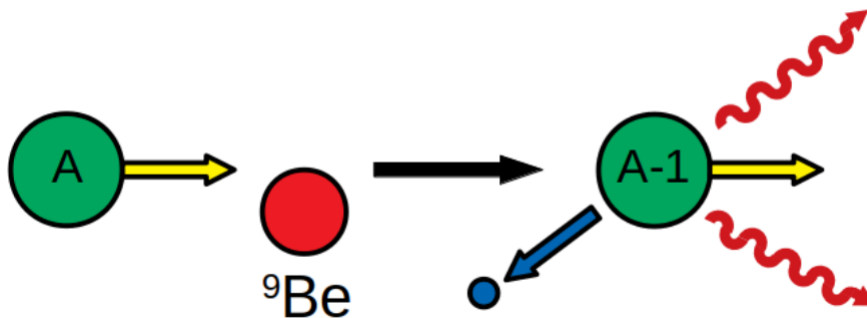


Figure 2.9: Illustration of single nucleon knockout reaction between projectile and ^9Be target showing subsequent gamma-decay of excited product nucleus [42].

Chapter 3

Excited States of ^{130}Cd

3.1 HiCARI Experiments

In 2020 the excited states of ^{130}Cd were studied in HiCARI in-flight gamma spectroscopy experiments performed at the RIKEN (Institute of Physical and Chemical Research) Rare Isotope Beam Factory (RIBF) in Japan [43]. In the 2020 autumn term RIBF189 accelerator run a 60 pnA ^{238}U primary beam was generated by the RIBF Super Conducting Electron Cyclotron Resonance Ion Source (ECRIS) [44][45]. As illustrated in figure 3.1 the ECRIS beam is accelerated through the RIKEN heavy-Ion Linear Accelerator (RILAC) and 4 cyclotrons, the RIKEN Ring Cyclotron (RRC), Fixed-frequency Ring Cyclotron (fRC), Intermediate-stage Ring Cyclotron (IRC) and Superconducting Ring Cyclotron (SRC) before delivery to the BigRIPS magnetic fragment separator at 345 MeV/u. [44][45][46][47][48][49].

3.2 BigRIPS-ZeroDegree particle identification

Before entering BigRIPS the ^{238}U primary beam is impinged on a ^9Be production target illustrated in orange at F0 in figure 3.2. In this production target a wide range of radioactive nuclei are produced in abrasion-fission reactions [36]. The BigRIPS spectrometer is comprised of a series of dipole and quadrupole magnets which steer ions of interest through in F0-F7 focal planes illustrated in figure 3.2 [50]. In this case the BigRIPS magnets were tuned for optimal transmission of ^{130}Cd ions. After traversing BigRIPS detectors and ion-optical elements designed to identify passing ions (such as the 1.5 mm and 5 mm Al degraders in F1 and F5 focal planes), the cocktail beam of secondary products reaches a secondary target in F8 with approximately 220 MeV/u. In the 6mm ^9Be secondary target in F8 some nuclei engaged in knockout reactions producing excited nuclei. The in-flight gamma-decays of which are detected in the HiCARI High-Purity Germanium (HPGe) detection array that surrounds the secondary target [41]. As some of the incoming nuclei engage in knockout reactions the secondary reaction products are then identified in the ZeroDegree magnetic spectrometer in F8-F11 [51]. The ZeroDegree spectrometer's magnets were tuned for optimal transmission and

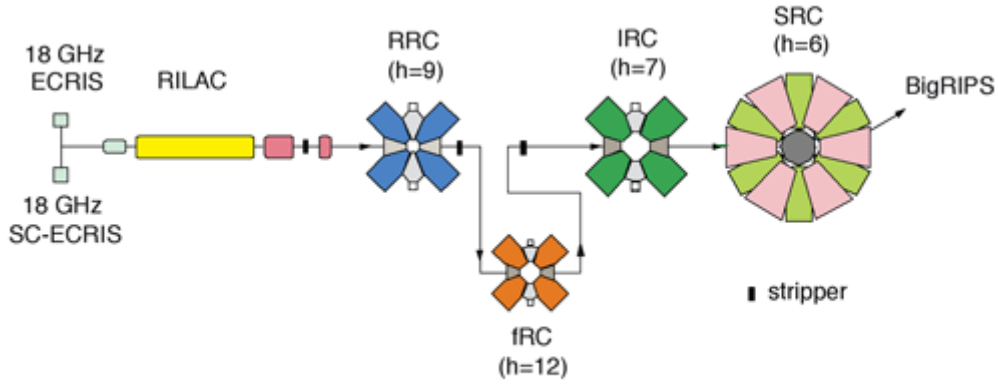


Figure 3.1: RIBF189 ^{238}U primary beam acceleration scheme showing ECRIS ion source, RILAC, RRC, fRC, IRC and SRC cyclotrons [49].

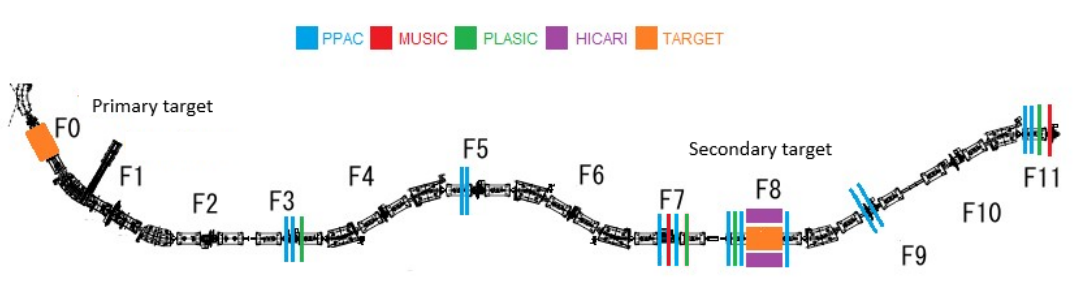


Figure 3.2: Illustration of BigRIPS and ZeroDegree magnetic fragment separators illustrating primary and secondary targets, PPAC, Music, Plastic scintillator and HiCARI detectors. Edited version of diagram from [51].

separation of ^{129}Ag ions.

3.2.1 Particle identification with the $TOF - B\rho - \Delta E$ method

In order to identify particles in BigRIPS and ZeroDegree the time-of-flight (TOF) of ions between when they are registered as travelling through the F3, F7, F8 and F11 focal planes is measured. The path length L taken by ions as they separate and bend through trajectories depending upon their mass-charge ratio $\frac{A}{Q}$ is also reconstructed from the positions in the XY plane. They are recorded as traversing in parallel plate avalanche counters at F3, F5, F7, F8, F9 and F11 with velocities β [52][53].

$$TOF = \frac{L}{\beta c} \quad (3.1)$$

By equating the electromagnetic force on an ion travelling at a velocity β through a perpendicular magnetic field B to the force required to accelerate it through a circular trajectory with radius ρ , a relation for $\frac{A}{Q}$ ratio can be obtained [52].

$$\frac{A}{Q} = \frac{B\rho}{\beta\gamma} \frac{c}{m_u} \quad (3.2)$$

where γ is the Lorenz factor and m_u is the atomic mass unit. As shown in figure 3.2 a MUSIC (Multi-sampling ionization chamber) detector is also positioned before and after the target in F7 and F11 [54]. As expanded upon in section 3.2.4 by comparing the energy deposited by an ion in the known thickness of a MUSIC detector travelling at a velocity β reconstructed from the TOF measured between plastic scintillators and the path length traversed between PPACs, an ions atomic number can be reconstructed. By means of the $TOF - B\rho - \Delta E$ method the atomic number of ions in the F7 and F11 focal planes (Z_7 and Z_{11}) and the A/Q ratio of ions across the F3-F5, F5-7, F8-F9 and F9-F11 focal planes $\left(\frac{A}{Q}\right)_{35}$, $\left(\frac{A}{Q}\right)_{57}$ and $\left(\frac{A}{Q}\right)_{911}$ can be reconstructed

$$\left(\frac{A}{Q}\right)_{35} = \frac{B\rho_{35} c}{\beta_{35}\gamma_{35} m_u} \quad (3.3)$$

$$\left(\frac{A}{Q}\right)_{57} = \frac{B\rho_{57} c}{\beta_{57}\gamma_{57} m_u} \quad (3.4)$$

$$\left(\frac{A}{Q}\right)_{911} = \frac{B\rho_{911} c}{\beta_{911}\gamma_{911} m_u} \quad (3.5)$$

3.2.2 Charge state changes

If the charge state of an ion does not change, its $\frac{A}{Q}$ ratio should be constant. With a constant $\frac{A}{Q}$, the amount deflected ρ due to an external magnetic field B should be constant (i.e $\Delta B\rho = 0$) [52]. The $\Delta B\rho_{if}$ between the dipole magnets deflecting the beam before $B\rho_i$ and after $B\rho_f$ the target can therefore be constructed with

$$\Delta B\rho_{if} = \frac{B\rho_i - B\rho_f}{B\rho_f} \quad (3.6)$$

reflecting if an ion has picked up or lost an electron in the target and therefore changed its charge state and $\frac{A}{Q}$.

3.2.3 PPAC detectors

BigRIPS-ZeroDegree PPACs (such as shown in figure 3.3) consist of pairs of parallel electrode plates through which a voltage is applied forming anode and cathode pairs. The volume between the electrodes is filled with an 3-50 Torr ionisation gas such as isobutene (C_4H_{10}) or Octafluoropropane (C_3F_8) [53]. When ions traverse the gaseous volume they ionise electrons producing avalanches of charged electron-ion particle pairs which flow toward the charged plates. The cathode plate is attached to a delay line so that when charge is deposited on a particular segment the time difference (with a unique delay for each segment) between charge detection at either end of the PPAC can be studied to reconstruct positions within the 240mm x 150mm horizontal plane with root-mean-squared resolution of 0.25mm. The high electron mobility and small distance between plates results in a short signal rise time which following waveform analysis enables PPAC hit timings with precision on the order of nanoseconds to be extracted [49].

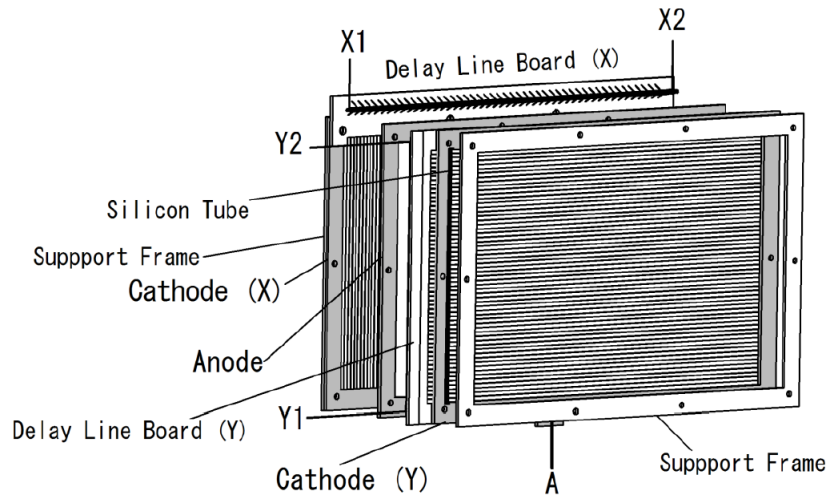


Figure 3.3: Diagram of PPAC showing charged anode/cathode plates enclosing ionization gas volume connected to delay line [53].

BigRIPS-ZeroDegree PPACs are positioned in sets of two or three along the beamline maximising detection efficiency and enabling the trajectory of ions to be interpolated between them. As the timing of PPAC charge signals are read out from either end of the delay line, events with a time difference $T_{sum} = T_1 + T_2$ inconsistent with the expected behaviour of the PPAC delay line (such as multi-hit events and events in which δ -rays are generated) can be removed [52]. As shown in figure 3.4 these abnormal events manifest as tails to a T_{sum} Gaussian distribution which can be removed by selecting an interval containing the Gaussian component of the distribution.

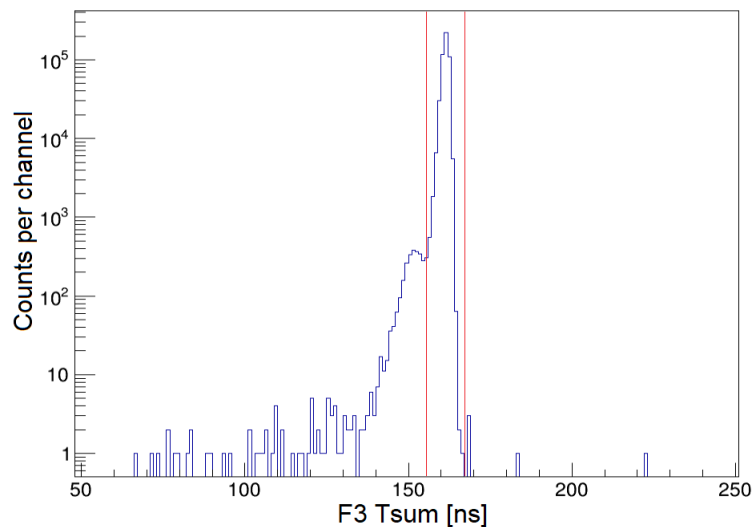


Figure 3.4: T_{sum} histogram for BigRIPS F3 PPACs demonstrating BigRIPS-ZeroDegree background suppression selection. Red interval showing suppression of inconsistently detected ion events.

3.2.4 MUSIC detectors

BigRIPS-ZeroDegree MUSIC detectors (such as the ones illustrated in figure 3.5) consist of stacks of 24 alternating anode-cathode plates tilted to 30 deg from the beamline which are positioned with 20mm gaps between each plate [54].

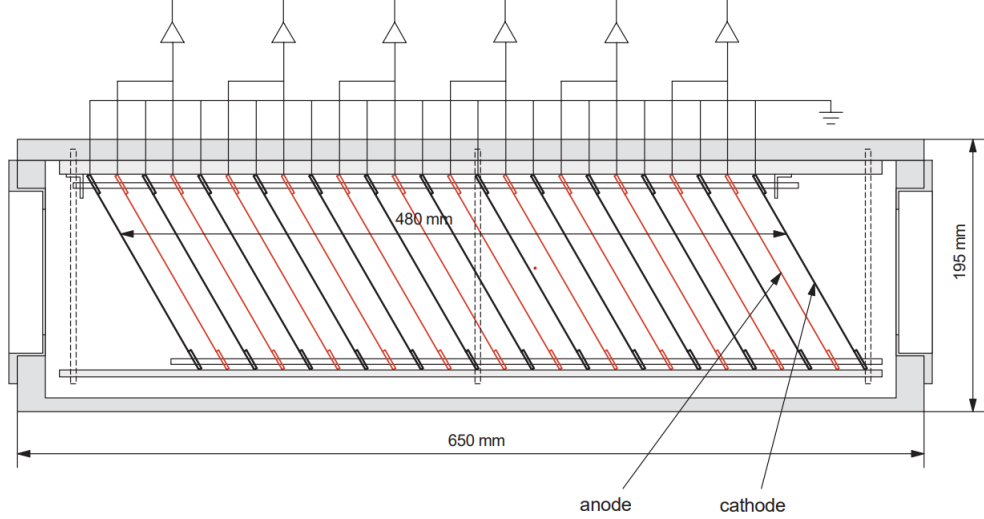


Figure 3.5: Cross-sectional diagram of tilted electrode gas ionization chamber MUSIC detector used by BigRIPS and ZeroDegree. Diagram from [54].

Similarly to the PPACs the gaps between the plates are filled with ionization gas so that traversing ions can ionise the gaseous atoms to create charged electron-ion pairs for collection by the charged plates. The plates are tilted to minimise signal losses due to the recombination of electron-ion pairs. The energy deposited dE by an ion as it penetrates a distance dx depending upon its atomic number z and its velocity β in accordance with the Bethe-Bloch equation [55].

$$-\frac{dE}{dx} = \frac{4\pi}{m_e c^2} \cdot \frac{n z^2}{\beta^2} \cdot \left(\frac{e^2}{4\pi\epsilon_0} \right)^2 \cdot \left[\ln \left(\frac{2m_e c^2 \beta^2}{I_e \cdot (1 - \beta^2)} \right) - \beta^2 \right] \quad (3.7)$$

where n is the electron number density of the material, I_e is the mean excitation energy and ϵ_0 is the vacuum permittivity. Using equation 3.7 the atomic number of passing ions can therefore be determined using the energy deposited in the known thickness of the stacked MUSIC plates. The achievable atomic number resolution of the MUSIC detectors has been determined to be $\Delta z = 0.2 - 0.3$ for a ^{40}Ar beam at 95 MeV/u. The ionisation gas is a mixture of Argon and Methane yielding a signal rise time of $0.3\mu\text{s}$. This enables the MUSIC detectors to achieve ion detection rates of up to 1 MHz [54].

3.2.5 Plastic scintillators

The BigRIPS-ZeroDegree plastic scintillators illustrated in green in figure 3.2 consist of 0.2mm thick optically transparent plastic blocks attached to a pair of PhotoMultiplier Tubes (PMTs) on their horizontal sides [52][56]. When ions traverse the plastic block a splash of scintillation light is emitted isotropically which travels to the PMTs and is converted into many electrons [56]. The charge of the electron signal is then processed enabling the timing of the passage of ions to be determined to with a resolution of 40ps. The charge-integrated signal q_1 and q_2 induced by the deposition of scintillation light in the left or right end PMT depends upon the horizontal position through which the ion passed x , within the width of the detector L

$$q_1 = q_0 \exp\left(-\frac{L+x}{\lambda}\right) \quad (3.8)$$

$$q_2 = q_0 \exp\left(-\frac{L-x}{\lambda}\right) \quad (3.9)$$

where λ denotes the attenuation length of light in the scintillation material and q_0 denotes the total charge signal emitted [50]. Rearranging equation 3.8 and 3.9 for a position x , one obtains

$$x = -\frac{\lambda}{2} \ln \frac{q_1}{q_2} \quad (3.10)$$

Similarly the position through which the ion traversed the scintillation block can be determined using the timing of the arrivals of the charge signals t_2 and t_1 in the left and right PMT's

$$x = -\frac{V}{2}(t_2 - t_1) \quad (3.11)$$

where V is the speed of light in the scintillation material [52]. With two independent measurements of hit positions, events which are detected with inconsistent correlations of charges and timings can be removed by plotting $\ln \frac{q_1}{q_2}$ against $t_2 - t_1$ [52]. Figure 3.6 is a 2-dimensional histogram of $\frac{q_1}{q_2}$ and $t_2 - t_1$ detected in the F3 plastic scintillator, demonstrating how events with inconsistently detected charges and registered timings can be excluded.

3.2.6 A/Q correction coefficients

As shown in equations 3.3, 3.4 and 3.5, the A/Q ratio reconstructed for ions in BigRIPS and ZeroDegree depends upon the TOF measured between plastic scintillators determining the ion velocity and the trajectories reconstructed between PPACs [52]. The reconstructed A/Q is therefore correlated with ion x , y , A and B as measured in the PPACs and the volume of charge q collected in the scintillators depending upon the incident velocity. The precision of the reconstructed A/Q ratio R_0 can therefore be improved by introducing a series of x , y , A , B and q correlation correction coefficients a_i to second order such that

$$R_{corr} = R_0 + a_0x + a_1x^2 + a_2y + a_3y^2 + a_4A + a_5A^2 + a_6B + a_7B^2 + a_8q + a_9q^2 \quad (3.12)$$

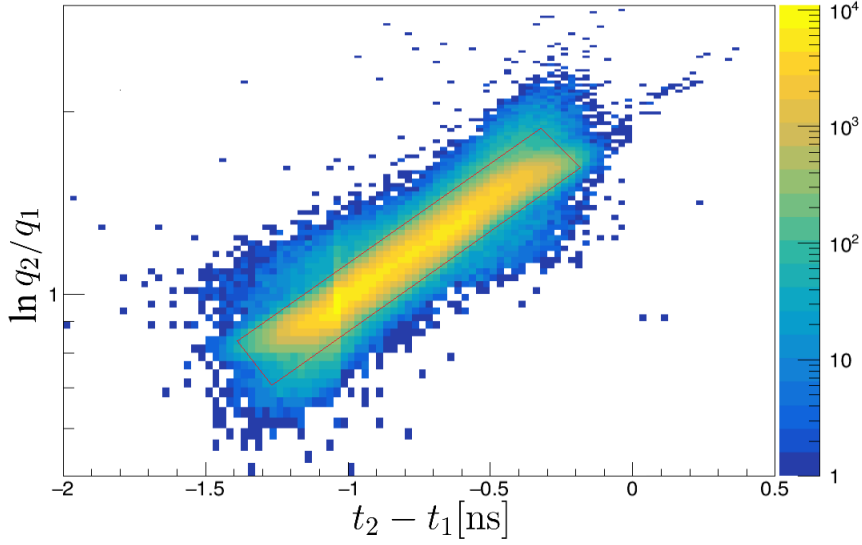


Figure 3.6: Histogram showing F3 plastic scintillator $\ln \frac{q_1}{q_2}$ to $t_2 - t_1$ correlation. Labelled with graphical selection on correlation of positions reconstructed using timings and charge methods.

where R_{corr} is the corrected A/Q ratio. The A/Q against Z histograms in figures 3.7 and 3.8 show the precision of the A/Q BigRIPS particle identification before the application of the correlation correction and after respectively. By fitting the A/Q spread of ^{130}Cd in figures 3.7 and 3.8 the BigRIPS A/Q resolution was found to improve by 21.4% from $\frac{\Delta A/Q}{A/Q} = 0.002489$ to $\frac{\Delta A/Q}{A/Q} = 0.001956$ after the application of the correction coefficients.

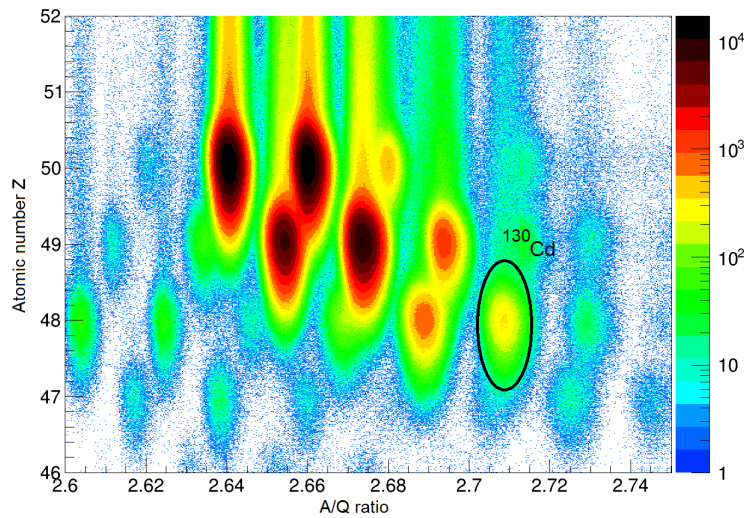


Figure 3.7: BigRIPS Z vs A/Q histogram labelled with incoming ^{130}Cd ions before application of correction coefficients.

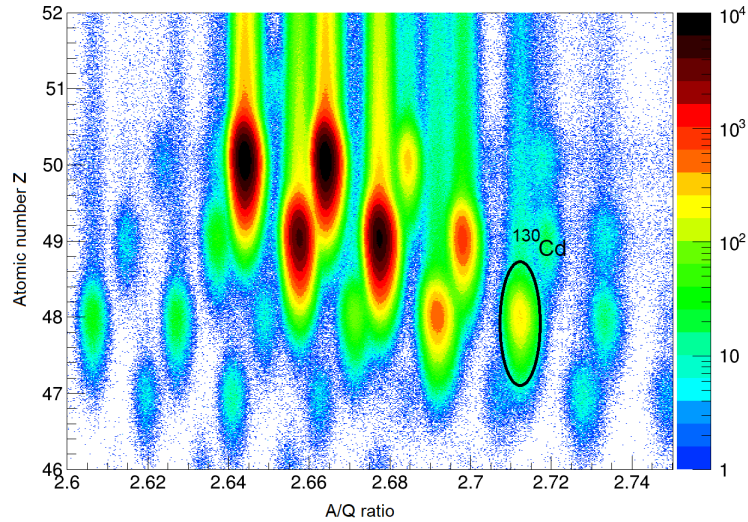


Figure 3.8: BigRIPS Z vs A/Q histogram labelled with incoming ^{130}Cd ions after application of correction coefficients.

RIBF189 particle identification

As shown in figure 3.9 the $\Delta B\rho_{if}$ constructed around the secondary target in equation 3.6 indicates a small ions changed charge state. The 6mm secondary ^9Be target is the thickest material encountered by the beam as it travels between the dipole magnets before and after the target where $\Delta B\rho_{if}$ was constructed and likely therefore facilitated most of the changes in charge state.

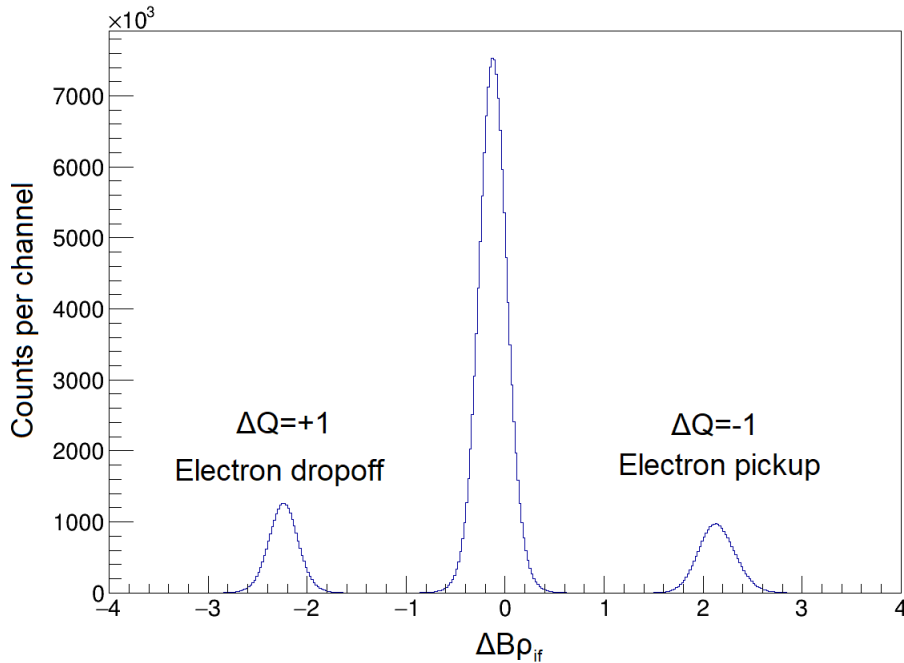


Figure 3.9: $\Delta B\rho_{if}$ histogram demonstrating separation of ions that change charge state from between the dipole magnets before and after the F8 target and those that do not.

If all ions were combined in one Z-A/Q plot such as in figure 3.8 for the BigRIPS separator, the A/Q separation of isotopes in the Zerodegree spectrometer would be reduced as some ions would shift in A/Q ratio. Particle identification is therefore achieved after the target by separating ions into those that increase charge state, decrease charge state or remain unchanged. Figures 3.10, 3.11 and 3.12 show the A/Q-Z histograms obtained for these groups respectively after unique correlation correction coefficients are applied in each case. The outgoing ^{130}Cd ions of interest are labelled in black in each case.

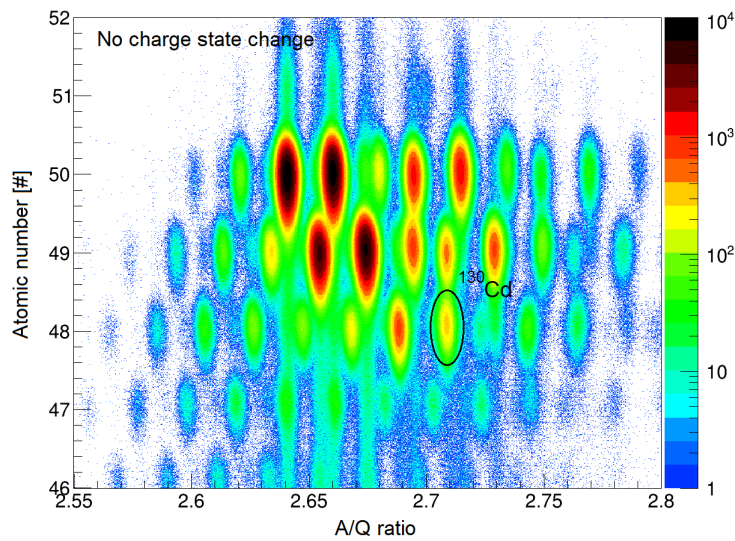


Figure 3.10: ZeroDegree ZvsA/Q histogram showing ions that did not change charged state with labelled ^{130}Cd ions.

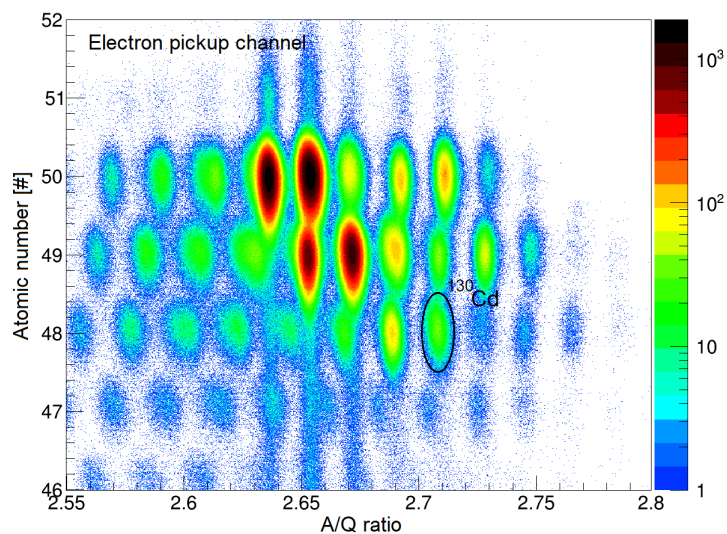


Figure 3.11: ZeroDegree ZvsA/Q histogram showing electron pickup charge state channel with labelled ^{130}Cd ions.

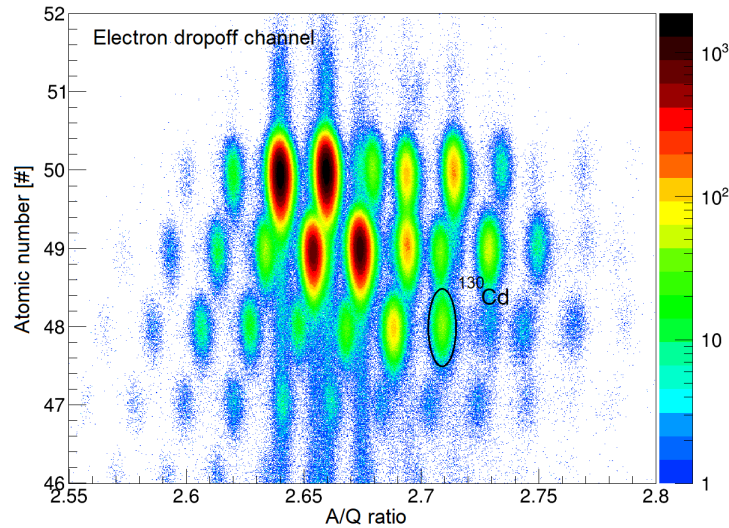


Figure 3.12: ZeroDegree $ZvsA/Q$ histogram showing electron drop-off charge state channel with labelled ^{130}Cd ions.

3.2.7 Reaction channels statistics

By selecting ions entering the secondary target from the BigRIPS spectrometer in figure 3.8 and selecting ions exiting the target into the ZeroDegree spectrometer in figures 3.10, 3.11 and 3.12 the total number of ions in relevant knockout reaction channels are summarised in table 3.1. As shown table 3.1 a total of 171523 ^{131}In ions were produced in proton knockout reactions from ^{132}Sn and a total of 121447 ^{130}Cd ions were produced in proton knockout reactions from ^{131}In . As shown in figures 3.8 and 3.10, 3.11 and 3.12, many other incoming and outgoing isotopes in the ^{132}Sn region were also produced, however the analysis of these isotopes and their correlated in-flight gamma-decays are not the focus of this thesis and are not presented.

Reaction channel	Number of ions
$^{132}\text{Sn} \rightarrow ^{131}\text{In}$	171523
$^{131}\text{In} \rightarrow ^{130}\text{Cd}$	121447

Table 3.1: Table of ^{131}In and ^{130}Cd ions produced in proton knockout reactions in the secondary HiCARI target.

3.3 HiCARI HPGe array

In order to detect gamma-rays emitted in the in-flight gamma-decays of the excited states of ^{130}Cd nuclei produced in the secondary target, the HiCARI HPGe detector array was positioned around the target.

3.3.1 High-purity Germanium detectors

The primary reason HPGe detectors were used is because they have excellent gamma-ray energy resolution of a few keV depending upon the gamma-ray energy such as $\Delta E_{intr} \sim 1.9$ keV FWHM at 1332.5 keV [55]. A energy resolution of a few keV is favourable then for targeting gamma-rays emitted in transitions with energies on the order of 100 keV-2 MeV predicted by the shell model calculations in table 2.2 as the intrinsic energy resolution is small compared to the gamma-ray energy. Furthermore, crystalline germanium has a small 0.7 eV bandgap, meaning even low energy gamma-rays can generate large charge signals due to the small amount of energy required to create each electron-hole charge carrier pair. This means that strong detector signals for even low energy gamma-rays are attainable [56]. HPGe crystal volumes are typically disk or coaxial cylinder in shape through which a central hole can be partially drilled with the surrounding angular section segmented into electrically isolated parts. Miniball detectors such as the one illustrated in figure 3.13 are segmented into six parts [59]. A voltage is applied through the central hole surface inducing an anode-cathode structure between the central and outer segment structures. As expanded upon in section 4.7.7, incident photons deposit energy in the Ge semiconductor structure, resulting in the emission of electrons which flow through an externally applied electric field to the anode for detection.

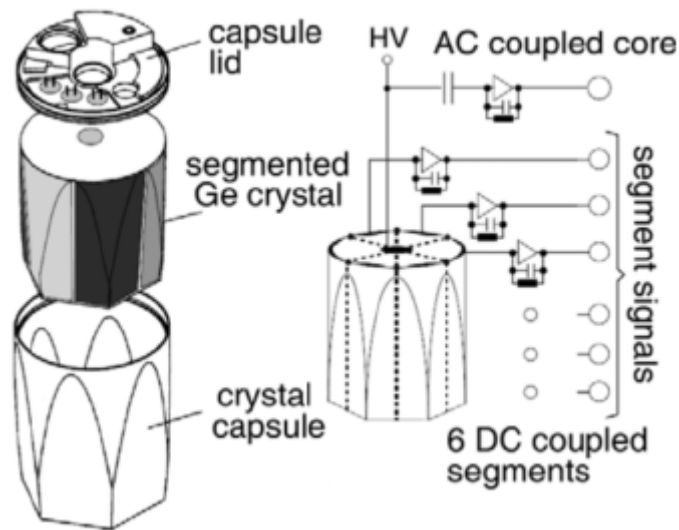


Figure 3.13: Illustration Miniball HPGe crystal segmented into 6 sections surrounding a central core [59].

With such a small semi-conductor band gap room temperature thermal fluctuations are sufficient to liberate electrons. At room temperature, charge signals produced by gamma-rays of interest are downed out by thermal noise. HPGe detectors such as the Miniball detector pictured in figure 3.14 therefore house cryogenic dewars containing coolants (such as liquid nitrogen) which cool the HPGe crystal and parts of the electronics in order to avoid this noise [51][52].

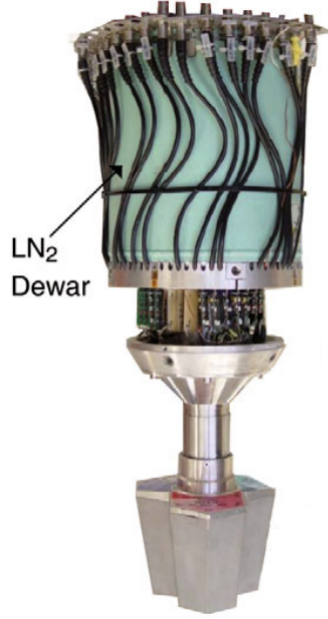


Figure 3.14: Picture of Miniball detector showing LN₂ Dewar which cool the HPGe crystals and parts of the electronics below [59].

3.3.2 Doppler correction in HiCARI in-flight decay spectroscopy experiments

The HiCARI HPGe array consists of 6 Miniball clusters [59], four Supercover [60] detectors as well as a LBNL P3 and a RCNP Quad detector which hereafter are together referred to as the tracking detectors [60]. As ions are delivered to the secondary target at relativistic velocities, gamma-rays emitted in transitions between their excited states are detected at Doppler shifted energies in the stationary HiCARI array [61]. The energy measured in the stationary detector reference frame E_γ depends upon the rest frame energy E_0 and the emission angle θ_γ of the gamma-ray from the ions direction of flight at a velocity β .

$$E_\gamma = E_0 \frac{\sqrt{1 - \beta^2}}{1 - \beta \cos \theta_\gamma} \quad (3.13)$$

In order to extract the the rest frame gamma-ray energies from the measured, the emission angle and velocity of the ion at the point of emission must therefore be reconstructed. The resolution ΔE_0 with which rest frame gamma-ray energies can be obtained following a correction for the Doppler shift depends upon the $\Delta\theta_\gamma$ angular resolution, the $\Delta\beta$ velocity resolution and the intrinsic energy resolution of the detector ΔE_{intr} for a gamma-ray emitted at an angle θ_γ from an ion at velocity β [61].

$$\left(\frac{\Delta E_0}{E_0}\right)^2 = \left(\frac{\beta \sin \theta_\gamma}{1 - \beta \cos \theta_\gamma}\right)^2 (\Delta\theta_\gamma)^2 + \left(\frac{\beta - \cos \theta_\gamma}{(1 - \beta^2)(1 - \beta \cos \theta_\gamma)}\right)^2 (\Delta\beta^2) + \left(\frac{\Delta E_{intr}}{E_\gamma}\right)^2 \quad (3.14)$$

3.3.3 Emission angle and velocity reconstruction

The secondary target illustrated in orange in figure 3.15 is a passive target. As a passive target is used in HiCARI experiments, no information regarding where within the

target the reaction of interest occurred is available. As the location of the reaction is not measured on an event-by-event basis, it can only be assumed to occur at an average depth through the target. This is significant because the site of the emission of a gamma-ray in a transition from an excited state of an ion populated in a secondary target reaction to another state is also not measured. The gamma-ray emission site is therefore assumed to be the same as the average reaction location.

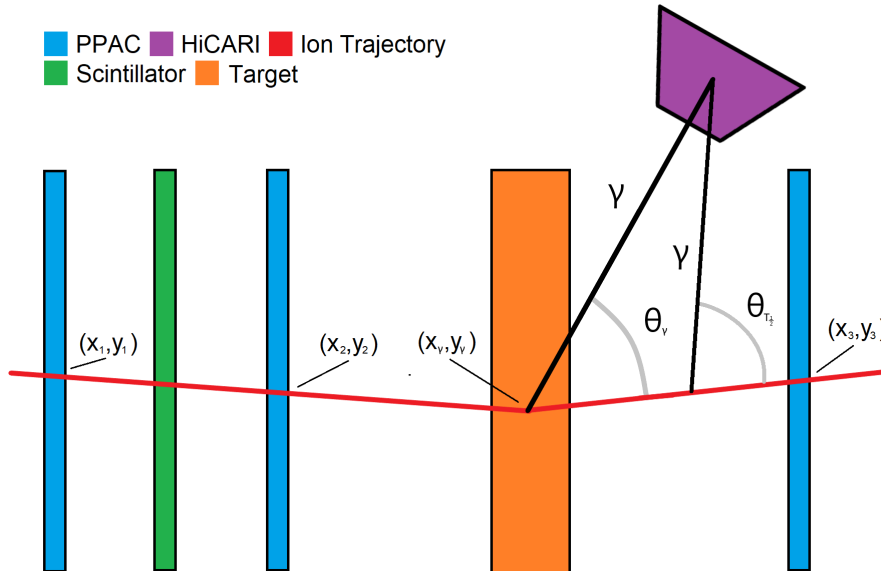


Figure 3.15: Illustration of HiCARI Doppler reconstruction of ion trajectory through F8 PPACs to mid-target and reconstruction of gamma-ray emission angles from mid-target position and half-life delayed emission site.

In order to determine where within the target nuclear reactions on average occur, the cross section for the absorption of incident ^{131}In ions as they penetrate the target and slow was calculated with DWEIKO [62]. The cross sections calculated for the absorption of ^{131}In ions in nuclear reactions as they penetrate the 6mm ^9Be target are approximately constant as shown in figure 3.16. The fraction of ^{131}In ions remaining unabsorbed in the target as a function of penetration depth was calculated using these cross sections and is shown in figure 3.17. As shown in figure 3.17 the number of ^{131}In ions remaining to engage in secondary reactions and populate excited state of interest reduces by 12.7% by the end of the target. The mean penetration depth before an ion engages in a reaction is therefore near the mid-point of the target at 2.8mm.

Emission angle reconstruction

As illustrated in figure 3.15, the positions through which incoming ions pass through the F8 PPACs (x_1, y_1) and (x_2, y_2) before the target is recorded and the trajectory of incoming ion through these positions is extrapolated to the middle of the target. At this mid-target location (x_γ, y_γ) the reactions are assumed to occur and gamma-rays are assumed to be emitted. The direction of ions when a gamma-ray is emitted is taken as the direction

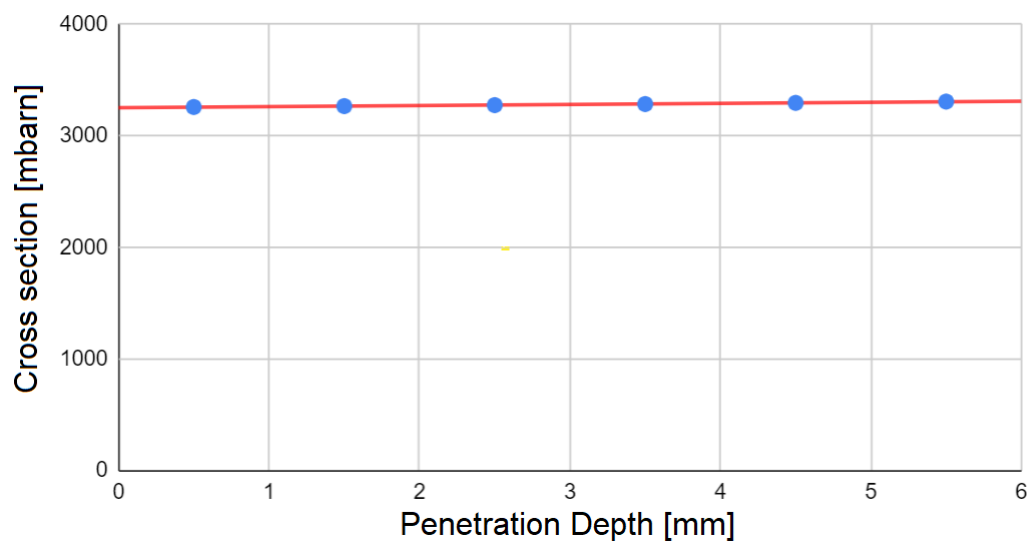


Figure 3.16: Plot of DWEIKO computed ^{131}In ion nuclear absorption cross section as they penetrate 6mm ^9Be target and lose kinetic energy [62].

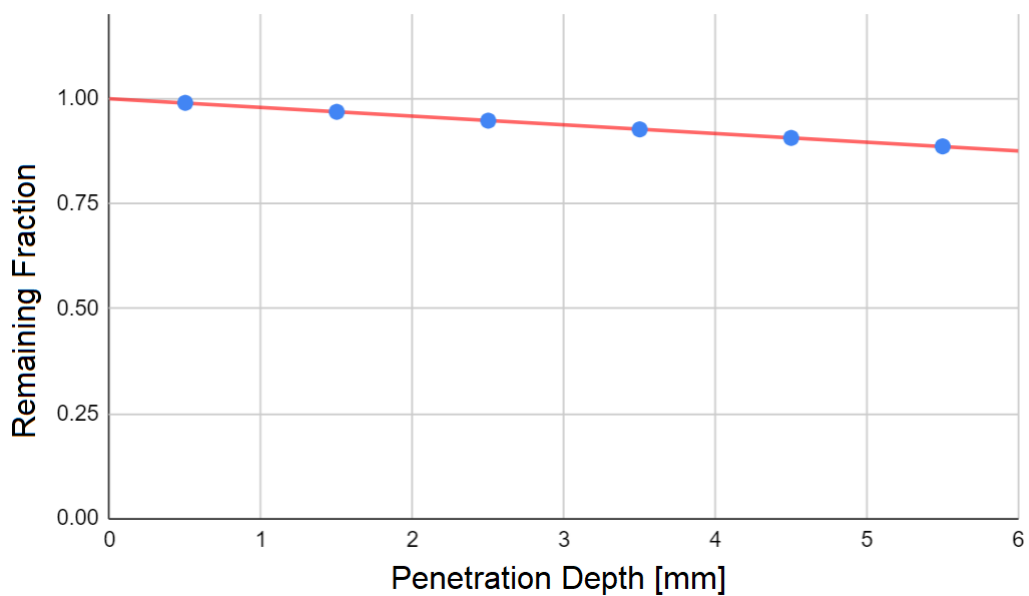


Figure 3.17: Plot of ^{131}In ions remaining un-absorbed in nuclear reactions as they penetrate 6mm ^9Be target. Absorption cross sections computed with DWEIKO [62].

along which it scatters from the mid-target location to the position with which it is recorded in the final F8 PPAC after the target (x_3, y_3). The gamma-ray emission angle θ_γ used in the Doppler correction is taken as the angle between the ions scattering direction and the direction from the mid-target location and the position at which the gamma-ray is detected in the HiCARI array.

Ion velocity reconstruction

The mid-target velocity β_{mid} used in the Doppler correction is reconstructed by measuring the after target velocity for each ion and comparing this to the average after target velocity $\bar{\beta}_{aft}$. The ratio by which an events velocity exceeds the average after the target is approximately the same by which it exceeds the average mid-target velocity $\bar{\beta}_{mid}$. This average mid-target velocity was determined in a LISE++ calculation for the velocity an ion must have had in the middle of the target to be slowed in the second half of the target to the average after target velocity [64]. The mid-target velocity for each ion β_{mid} was thereby reconstructed with the following equation

$$\beta_{mid} = \bar{\beta}_{mid} \cdot \left(1 + \frac{\beta_{aft} - \bar{\beta}_{aft}}{\bar{\beta}_{aft}}\right) \quad (3.15)$$

3.3.4 HiCARI array geometry

The average mid-target velocity for ions in the $^{131}\text{In} \rightarrow ^{130}\text{Cd}$ reaction channel was $0.56c$. In figure 3.16 the contributions of the angular, velocity and intrinsic energy uncertainty to $\frac{\Delta E_0}{E_0}$ are plotted as a function of θ_γ for the Miniball and tracking detectors at $\beta = 0.55c$. As shown in figure 3.16, at $\beta = 0.55c$ the energy uncertainty due to the angular uncertainty term is maximum at 56° where the contribution of the velocity term is minimum. If the tracking detectors are positioned close to the target at a distance of 130mm, the tracking detectors can achieve a position resolution of 0.15% (σ) [65]. The Miniball detectors at 200mm achieve a less good position resolution of 1.03-1.52% (σ). As the positions of hits in the tracking detectors can be precisely reconstructed they have low $(\Delta\theta_\gamma)^2$ angular uncertainty. The tracking detector $\frac{\Delta E_0}{E_0}$ is therefore dominated instead by the velocity uncertainty, resulting in a $\frac{\Delta E_0}{E_0}$ minimum at 56° . The less position sensitive Miniball detectors however have a larger $(\Delta\theta_\gamma)^2$ angular contribution to $(\frac{\Delta E_0}{E_0})$ which as shown in figure 3.18 results in optimal $(\frac{\Delta E_0}{E_0})$ at low angles and wide angles outside of 56° . Figure 3.19 shows the number of gamma-rays detected by detected by Miniball (green), Superclover (red) and tracking detectors (blue) in a simulation of the HiCARI array geometry as a function of the polar angle at which crystals were ultimately positioned from the nominal direction of the beam. As shown in figure 3.19, the Miniball detectors were positioned at low angles below 56° down to 20° . The tracking detectors were positioned at wider, $56 - 85^\circ$ angles which as shown in figure 3.18 is close to the $(\frac{\Delta E_0}{E_0})$ minima. The Superclovers were positioned were positioned at $50 - 95^\circ$ angles from the nominal direction of the beam. This simulation was produced using the UHiCARI

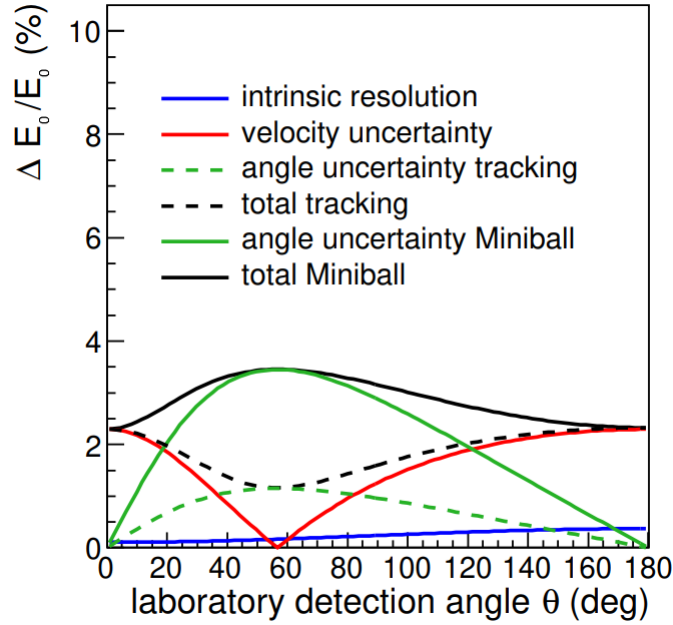


Figure 3.18: Proposed angular, velocity and intrinsic energy contributions to total Doppler corrected energy uncertainty for Miniball (solid line) and tracking (dashed line) detectors. Edited version of figure in proposal from [106].

(University of California HiCARI) Geant4 simulation package developed by the HiCARI collaboration which is based on the UCGRETINA package developed for the GRETINA HPGe array [63].

Lineshape analysis of Doppler corrected gamma-ray energies

After an excited state is populated in the target, there is a delay before a transition from that state occurs depending upon the strength of the transition. This results in an offset between the assumed site of emission in the middle of the target and site of the emission of the gamma-ray depending upon the velocity of the ion and the time before the transition. As illustrated in figure 3.15, this can result in an erroneously larger reconstructed emission angle $\theta_{T_{1/2}}$. As investigated in [61], erroneously larger emission angles result in a low energy tail in the Doppler corrected transition energy distribution which lowers the centroid of the distribution. By analysing the shape and position of the transition energy peak, the strength of the transition required to produce it can be inferred. In the analysis of HiCARI data, UCHiCARI simulations of gamma-ray energy distributions assuming half-lives, excitation energies and level schemes for the excited states of nuclei are compared to experimentally observed distributions. The nuclear structure of these nuclei is then inferred from the simulated gamma-ray energy distribution that best reproduces the experimentally observed distribution.

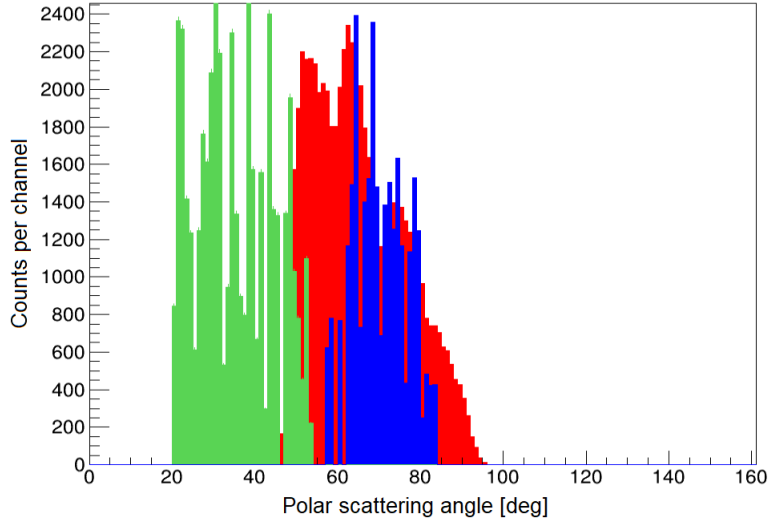


Figure 3.19: Reconstructed polar emission angle hits in tracking (red), Superclover (blue) and Miniball (green) from UCHiCARI simulation.

3.4 Analysis of HiCARI experiment

3.4.1 Experimental energy calibration

Before the BigRIPS spectrometer was focused on ^{130}Cd isotopes in the main experiment the HiCARI HPGe array was calibrated by positioning ^{60}Co and ^{152}Eu radioactive sources in the F8 target position in the middle of the array. By studying the raw channel numbers N_{chan} recorded in crystals at which gamma-rays with known energies occur, a pair of linear calibration coefficients A and B can be introduced, transforming the raw numbers into calibrated energies E_{calib} .

$$E_{calib} = A \cdot N_{chan} + B \quad (3.16)$$

These gamma-rays were identified on the basis of the observed relative intensities of the transitions. The residual difference between the known transition energies and the energy reconstructed by the calibrated energy from the raw channel numbers for each detector is shown in figure 3.20. As shown in figure 3.20 the energy resolution achieved by each HPGe crystal in the HiCARI array varied from $\sim 1 - 4$ keV.

3.4.2 Simulated HiCARI HPGe energies

The intrinsic resolutions achieved for each crystal were then implemented into their simulated UCHiCARI counterparts. A UCHiCARI simulation of a ^{152}Eu source was produced and in figure 3.21 the simulated gamma-ray energy distribution in red are compared to the experimentally observed ^{152}Eu energies in blue. As shown in figure 3.20 the energy and widths of the simulated gamma-rays well reproduces the energies and widths of the experimentally observed ^{152}Eu energy peaks. The energy peaks in the experimental distribution sit atop a layer of background noise which is not included

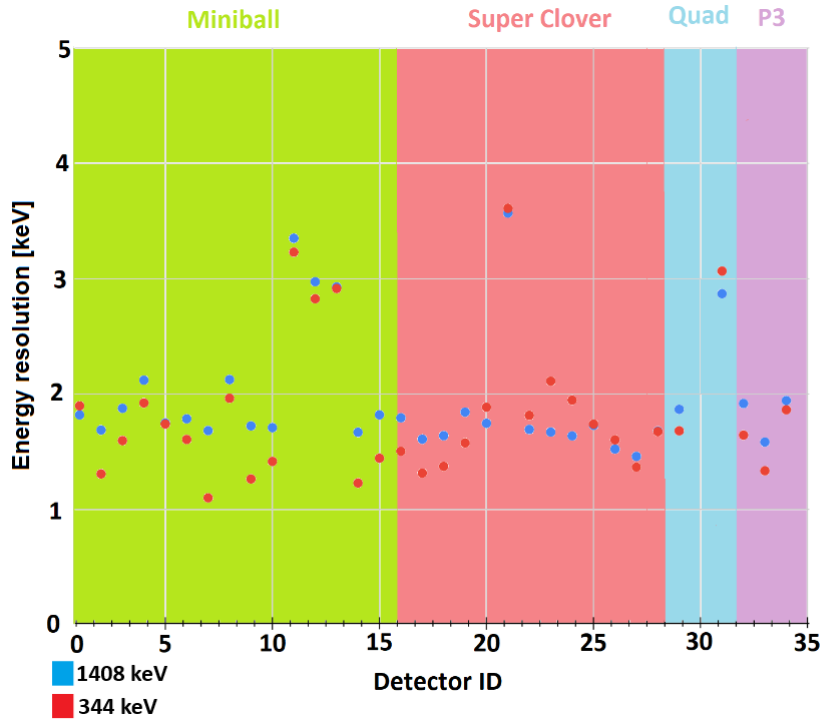


Figure 3.20: Residual energy between linear calibration of HiCARI raw channel energies and known ^{152}Eu source gamma-rays at 344 keV and 1408 keV for HiCARI HPGe crystals.

in the UCHiCARI ^{152}Eu simulation. The origin of backgrounds commonly seen in HPGe detectors includes, but is not limited to, cosmic rays, natural environmental radiations and electronic noise [57]. In order to compare UCHiCARI simulations to the experimentally observed distributions these backgrounds are accounted for as in section 3.4.5 rather than simulated.

3.4.3 Detector Efficiency

Experimental efficiency

The absolute detection efficiency of the HiCARI array was determined by counting the number of gamma-rays detected with known transition energies from the ^{60}Co and ^{152}Eu radioactive source data. The number of gamma-rays at each energy was then compared to the number that would have emitted over the course of the data acquisition time by the sources based on their recorded activity. As shown in figure 3.24 the absolute experimental detection efficiency declines for all detectors as a function of energy. The detection efficiency also drops at low energies because an electronic threshold was applied to the detectors in order to exclude low energy noise.

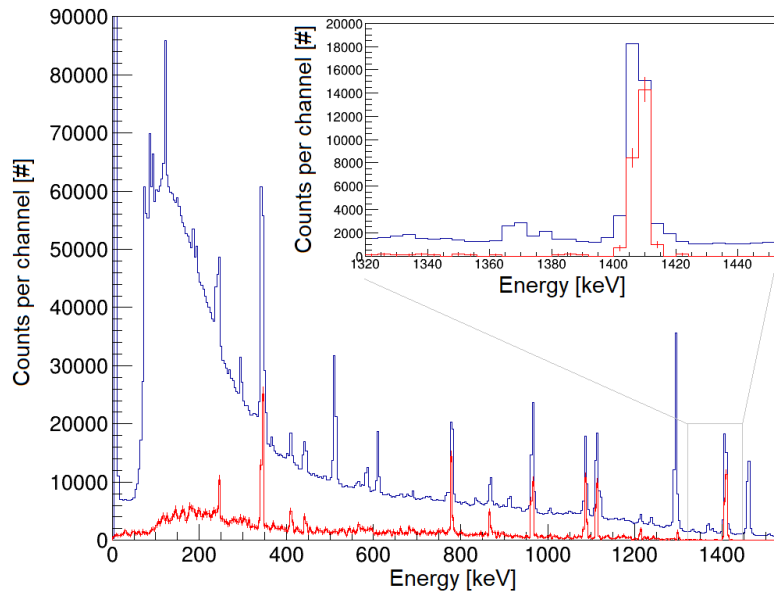


Figure 3.21: Comparison of experimental observed ^{152}Eu source gamma-ray energies (blue) to UCHiCARI simulated ^{152}Eu source energies (red) demonstrating consistency of simulated gamma-ray energy peak positions and widths with experimental.

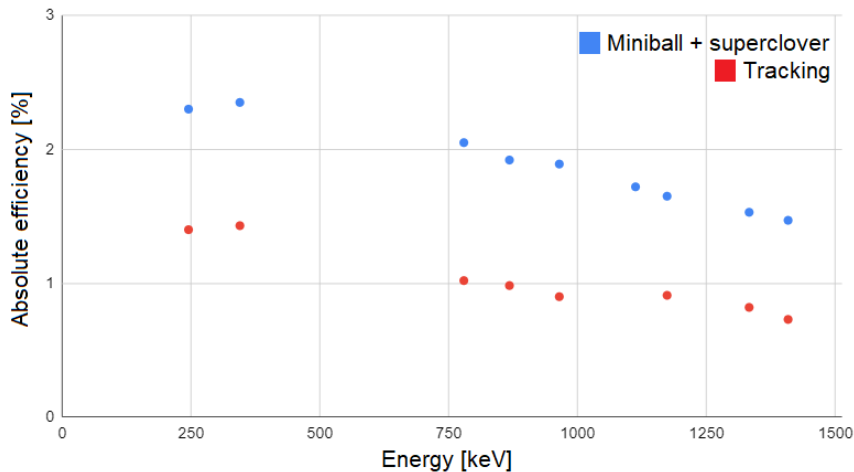


Figure 3.22: Absolute efficiency of HiCARI array measured as a function of gamma-ray energy for Miniball and superclover detectors as well as tracking detectors using the ^{60}Co and ^{152}Eu source data.

Simulated efficiency

The simulated detection efficiency of the HiCARI array was determined by simulating the isotropic emission of gamma-rays within a relevant range of energies from the center of the simulated array and comparing the number of gamma-rays detected to the number simulated. As shown in figure 3.22 the absolute simulated efficiency of the array declines as a function of energy, dropping at low energies similarly to the experimental efficiency due to the applied simulated detector thresholds.

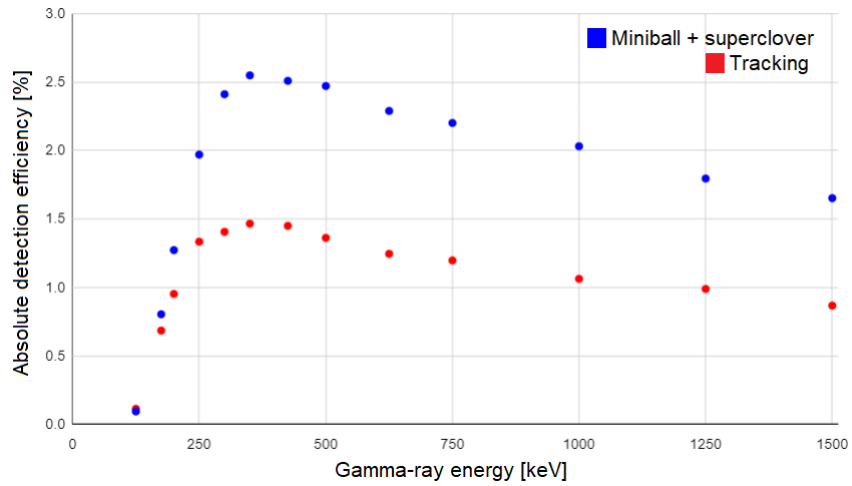


Figure 3.23: Absolute simulated HiCARI gamma-ray detection efficiency measured as a function of gamma-ray energy for the Miniball and superclover detectors combined and the tracking detectors from the UHiCARI simulations.

3.4.4 Comparison of simulated and experimental detection efficiency

In figures 3.24 and 3.25 the experimental absolute detection efficiency of Miniball, Superclover and tracking detectors is compared to their simulated counterparts. As shown in figures 3.24 and 3.25 the simulated and experimental efficiencies follows the same trend, however the simulated efficiency consistently and increasingly over-predicts the absolute efficiency towards higher energies. This suggests that while the experimental efficiencies are generally well reproduced, extraction of information particularly sensitive to the simulated detection efficiencies must account for this difference. One example is the extraction cross sections for the population of states in knockout reactions from the observed intensities of transitions. The extraction of cross sections for the $^{131}\text{In} \rightarrow ^{130}\text{Cd}$ proton knockout channel is in future intended to be pursued however is not presented in this work.

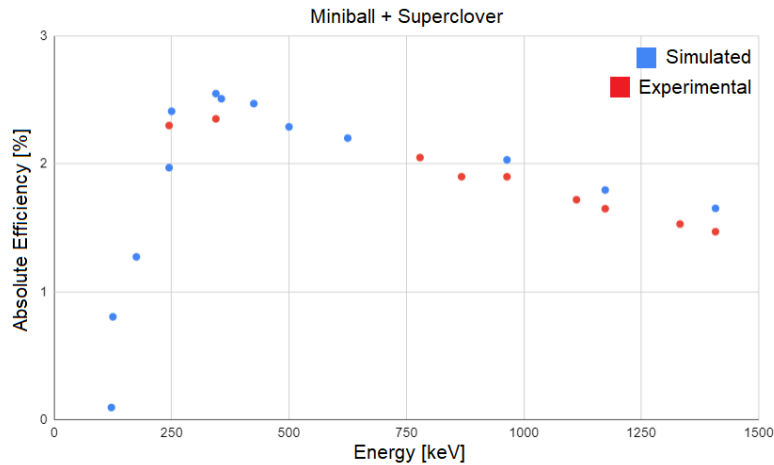


Figure 3.24: Combined Miniball and superclover absolute detection efficiency as a function of gamma-ray energy comparing experimentally measured detection efficiency from radioactive ^{152}Eu and ^{60}Co source data and UCHiCARI simulations.

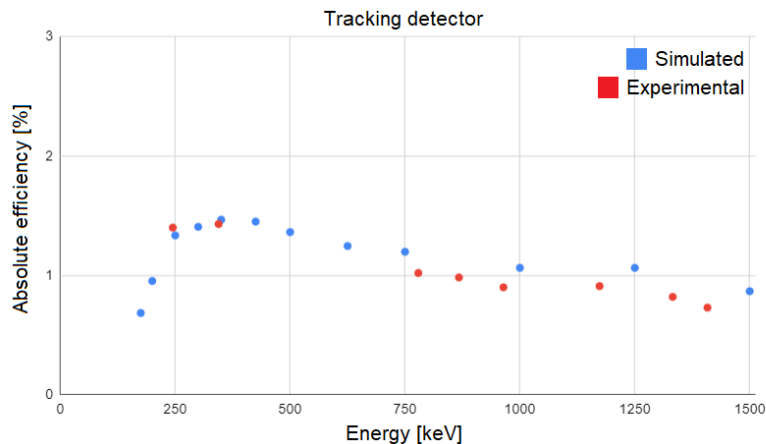


Figure 3.25: Tracking detector absolute detection efficiency as a function of gamma-ray energy comparing experimentally measured detection efficiency from radioactive ^{152}Eu and ^{60}Co source data and UCHiCARI simulations.

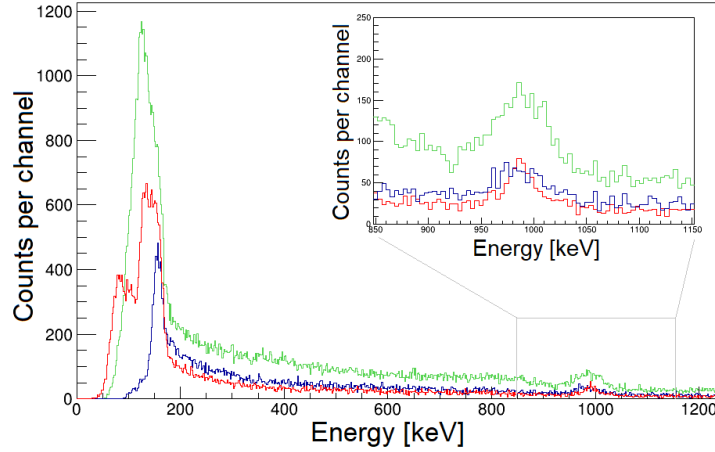


Figure 3.26: Experimentally reconstructed rest-frame gamma-ray energy histogram showing ^{131}In , $J^\pi = \frac{3}{2}^-$ 988 keV gamma-decay energy alignment in Miniball (green), Superclover (blue) and tracking detector (red).

3.4.5 Validation of energy-lifetime extraction with ^{131}In

As shown in figure 3.26 the Doppler corrected gamma-ray energy spectrum for gamma-rays detected in coincidence with ions in the $^{132}\text{Sn} \rightarrow ^{131}\text{In}$ reaction channel have energy peaks at 988 ± 1.5 , 986 ± 2.3 and 986 ± 1.8 keV for the tracking detectors, Miniball and Superclovers respectively. This gamma-ray energy peak is similar in energy to a previously measured 987.8 keV ($3/2^- \rightarrow 1/2^-$) ^{131}In transition observed in a previous experiment [66]. In accordance with the selection rules in section 2.4.1 this transition is of dominantly M1 multipolarity with a fast transition rate related in equation 2.23. This fast transition rate implies a short lifetime for the ($3/2^-$) state depending on the $B(M1; \frac{3}{2}^- \rightarrow \frac{1}{2}^-)$. This means that the 987.8 keV gamma-rays are emitted shortly after the state is populated. The alignment of the gamma-ray energy peaks across all three detector subsystems near to the known energy suggests a short lifetime for the state. This is because as established in section 3.3.4 the longer the lifetime the further the assumed emission point at the assumed mid-target reaction vertex is from the real emission point. As the observed transition energy is not strongly shifted from the known transition energy the ($3/2^-$) lifetime may be short. As the ($3/2^-$) half life is short and the energy of transition is known, this ^{131}In state forms an excellent test case for validating the extraction of state energies and lifetimes from experimental HiCARI gamma-ray energy spectra with UCHiCARI simulations.

Low energy background subtraction

The ^{131}In energy spectrum in figure 3.26 is dominated by (primarily Bremsstrahlung) background at low energies below ~ 200 keV [67]. The ions are assumed to spend the first half of the target as ^{132}Sn and the second half as ^{131}In . The distribution of this low energy background can therefore be taken as the sum of the background produced in the $^{132}\text{Sn} \rightarrow ^{132}\text{Sn}$ channel and $^{131}\text{In} \rightarrow ^{131}\text{In}$ channel. By extracting the shape

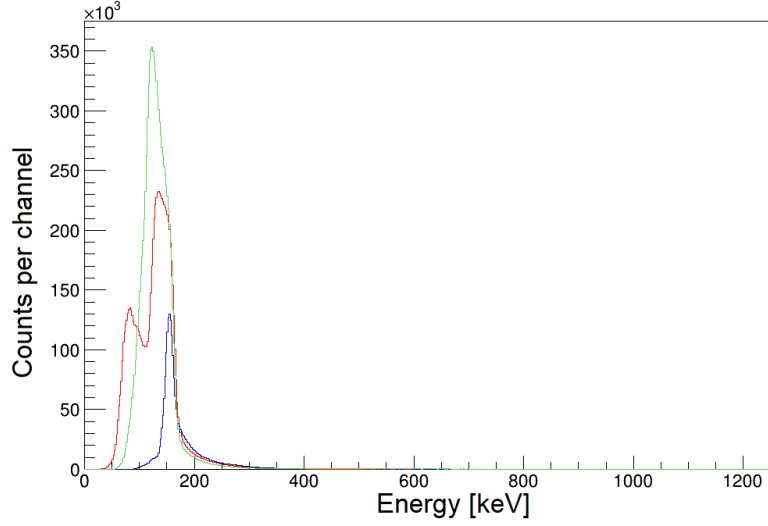


Figure 3.27: $^{131}\text{In} \rightarrow ^{131}\text{In}$ channel gamma-ray energy distribution showing tracking detector energies (red), Superclover energies (blue) and Miniball energies (green).

of the $^{132}\text{Sn} \rightarrow ^{132}\text{Sn}$ and $^{131}\text{In} \rightarrow ^{131}\text{In}$ Doppler corrected energy spectra and subtracting it from the $^{132}\text{Sn} \rightarrow ^{131}\text{In}$ energy spectra in proportion to the number of ions much of this low energy background can be removed. This leaves predominantly gamma-rays emitted from the deexcitation of excited states of populated in the reaction of interest. The $^{131}\text{In} \rightarrow ^{131}\text{In}$ Doppler corrected energy spectrum for all three detectors is shown in figure 3.27. Following the proportionate subtraction of this energy distribution and the $^{132}\text{Sn} \rightarrow ^{132}\text{Sn}$ distribution from figure 3.26, the remaining $^{132}\text{Sn} \rightarrow ^{131}\text{In}$ Doppler corrected Miniball energy distribution is plotted in figure 3.28 in blue.

Fitting experimental gamma-ray energy spectra with simulations

In order to compare the experimental energy distribution to the simulated energy distribution, the intensity of the remaining background N_{bkg} is fit with a double exponential as a function of gamma-ray energy E_{gam} with $k_i = k_0, k_1, k_2$ and k_3 fitting parameters with

$$N_{bkg} = k_0 e^{-k_1 \cdot E_{gam}} + k_2 e^{-k_3 \cdot E_{gam}} \quad (3.17)$$

shown in green in figure 3.28. The simulated Miniball ^{131}In Doppler corrected energy spectrum shown in purple is then fit on top of this background to the experimental distribution such as in figure 3.28. The intensity of this combined N_{comb} background N_{bkg} and simulated N_{sim} distribution is scaled by a smoothed-step function in order to reproduce the downward tapering of the experimental intensity N_{exp} at low energies introduced by Miniball detector thresholds such that

$$N_{comb} = k_4 \cdot \text{Erf}\left(\frac{E_{fit} - k_5}{k_6}\right) \cdot (N_{bkg} + k_7 N_{sim}) \quad (3.18)$$

with an additional four $k_i = k_4, k_5, k_6$ and k_7 fitting parameters. A χ^2 fitting test for a combination of k_i fitting parameters is then performed. As shown in equation 3.19

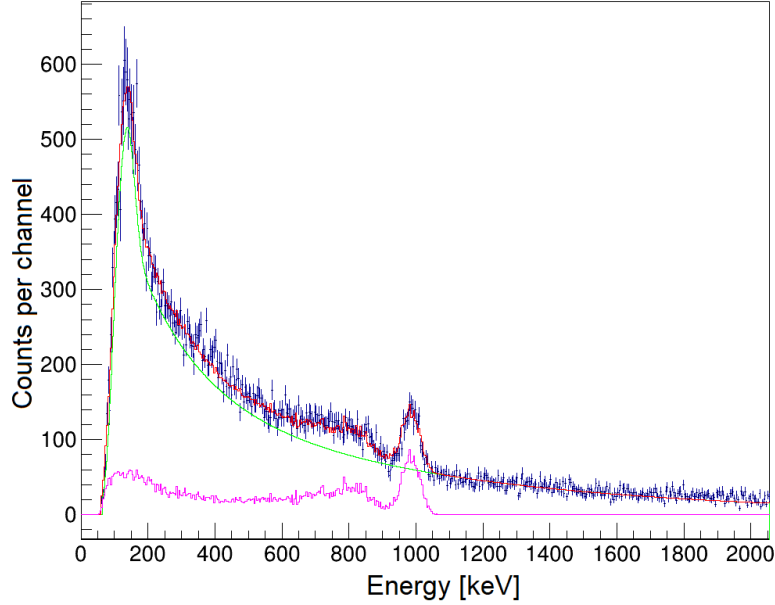


Figure 3.28: Reconstructed Miniball rest-frame gamma-ray energy distribution showing experimental energies (blue), simulated $^{131}\text{In } \frac{3}{2}^- \rightarrow \frac{1}{2}^-$ transition (purple) assuming a $T_{1/2} = 0.2\text{ps}$ half-life, fitted experimental background (green) and combined fit (red).

the χ^2 is defined as the sum of squares of the number of counts in the experimental distribution and the simulation-background combination.

$$\chi^2 = \sum_i \frac{(N_{exp} - N_{comb})^2}{N_{comb}} \quad (3.19)$$

The χ^2 therefore depends upon the fitted N_{comb} energy distribution determined by the chosen excitation energies and half-lives of states within the simulated level scheme. By varying the energy and half-life of the $(3/2^-)$ ^{131}In state the χ^2 for the separately fitted Miniball, Superclover and tracking detector gamma-ray energy distributions, the χ^2 energy half-life matrices in figures 3.29, 3.30 and 3.31 respectively were obtained. As summarised in table 3.3, the energy half life minima $(E_{min}, T_{\frac{1}{2},min})$ obtained for the Miniball, Superclover and tracking detector fits were $(E_{min}, T_{\frac{1}{2},min}) = (986.5, 1.2), (990.0, 5.0), (986.5, 1.0)$ respectively with uncertainties extracted in the following section.

Uncertainty analysis

There are a number sources of uncertainty associated with the energies and lifetimes which can be obtained by comparison of experimental gamma-ray energy spectra to simulated. These uncertainties can be categorised into those that either contribute to the experimental energy distribution N_{exp} or the simulated N_{sim} energy distribution which combines with the fitted background to form N_{comb} in 3.19. Equation 3.14 shows the uncertainty with which Doppler corrected gamma-ray energies can be obtained depends upon the intrinsic energy uncertainty of the detectors, the angular uncertainty

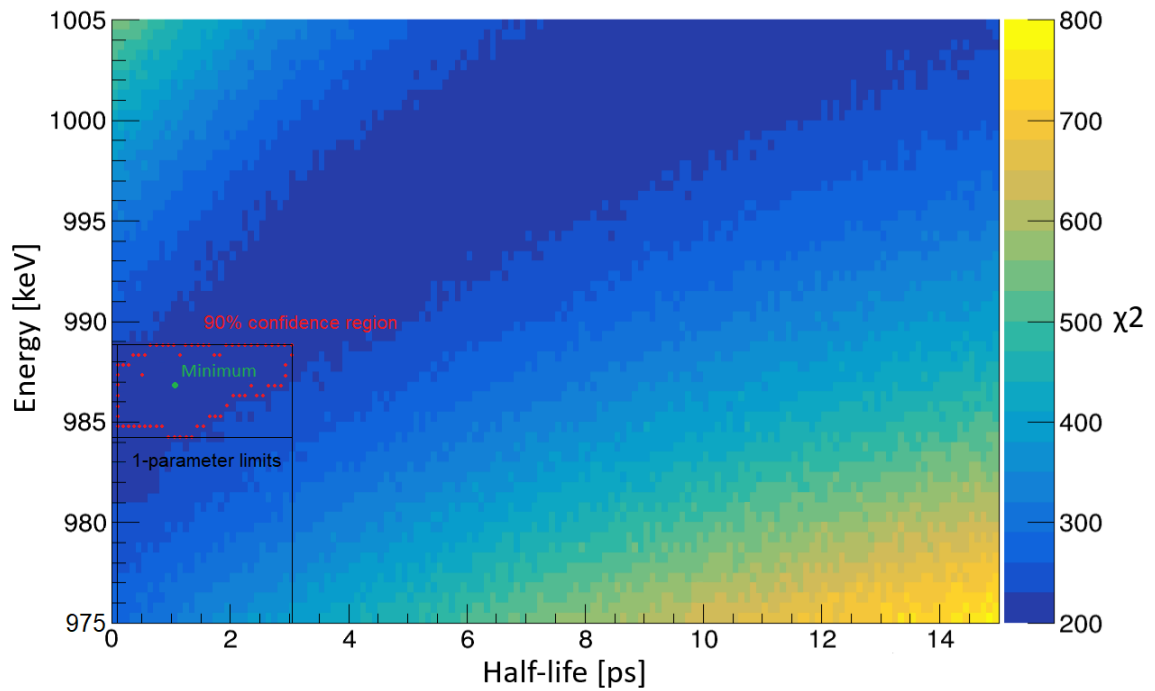


Figure 3.29: χ^2 Miniball histogram as a function of ^{131}In , $J^\pi = \frac{3}{2}^-$ UCHiCARI simulation excitation energy and half-life fitted to experimental energy distribution. Labelled with χ^2 minimum (red).

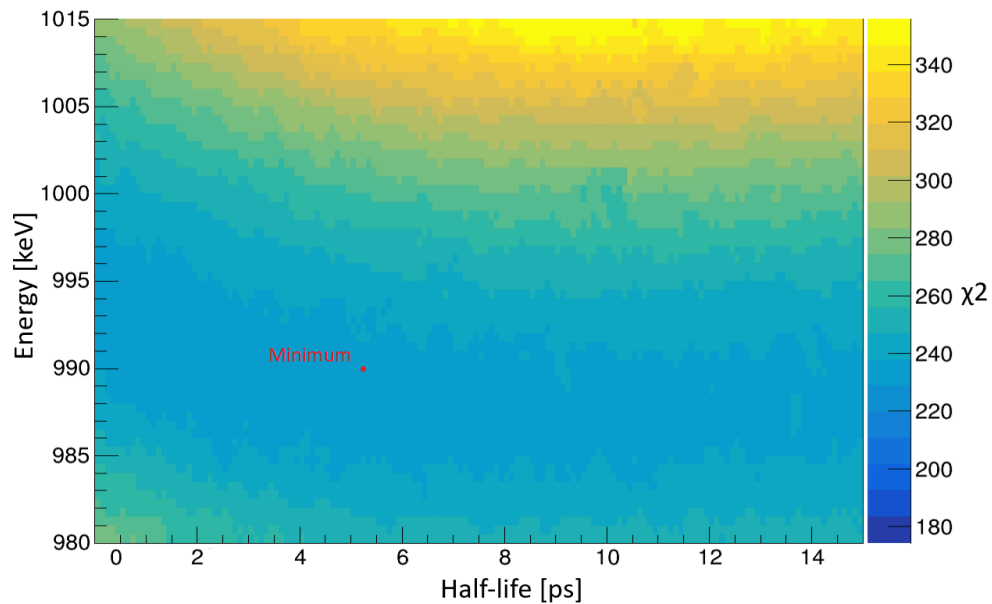


Figure 3.30: χ^2 Superclover histogram as a function of ^{131}In , $J^\pi = \frac{3}{2}^-$ UCHiCARI simulation excitation energy and half-life fitted to experimental energy distribution. Labelled with χ^2 minimum (red).

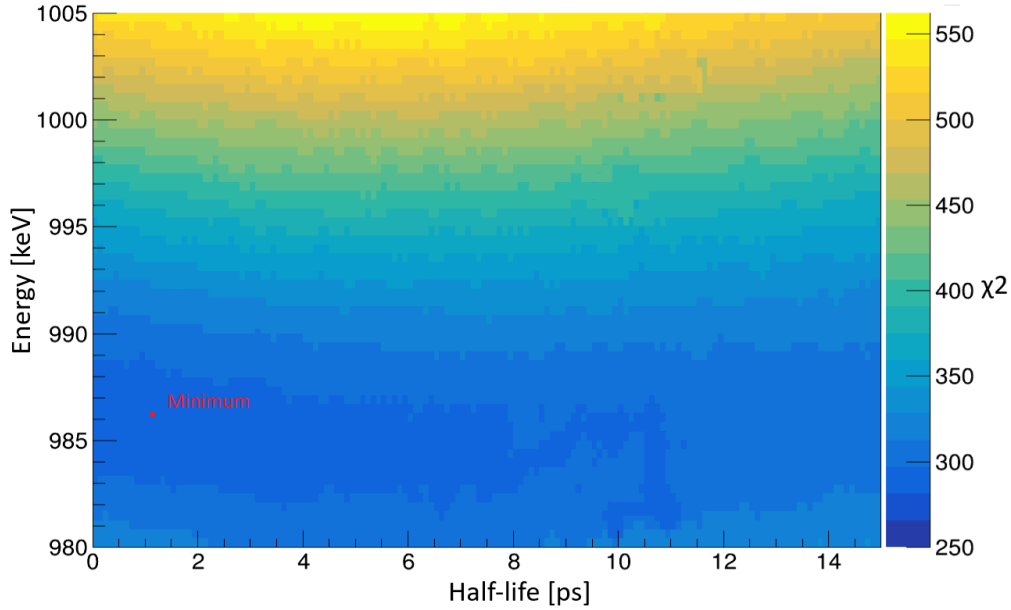


Figure 3.31: χ^2 tracking detector histogram as a function of ^{131}In , $J^\pi = \frac{3}{2}^-$ UCHiCARI simulation excitation energy and half-life fitted to experimental energy distribution. Labelled with χ^2 minimum (red).

and the velocity uncertainty. The intrinsic energy uncertainty of the HiCARI array was studied in section 3.4.1 by analysing radioactive source data. There are however many experimental contributions to $\Delta\theta$ and $\Delta\beta$. The precision of the longitudinal positioning of the secondary target within F8 for example would contribute to the uncertainty in the emission angle, shifting the reaction vertex at which the gamma-ray emission vertex is assumed. Similarly the accuracy with which the mid-target ion velocity is reconstructed from the extrapolation into the target from the velocity measured after the target on the basis of the LISE++ simulations would contribute to the velocity uncertainty [64]. By varying the average mid-target velocity used to reconstruct the mid-target velocity of each ion and the longitudinal position of the assumed mid-target reaction depth used to reconstruct the emission angle, the sensitivity of χ^2 fitting solutions to these potential sources of systematic uncertainty can be studied. As shown in figures 3.32 and 3.33, the χ^2 obtained for fitting simulated Miniball detector energies to the experimental as a function of assumed mid-target position and velocity takes a parabolic shape for all three detector subsystems. By fitting parabolas to these χ^2 distributions their minima were found and are summarised in table 3.2.

Parameter	Miniball	Superclover	Tracking
Velocity [c]	0.5595 ± 0.003	0.5638 ± 0.007	0.5624 ± 0.006
Target position [mm]	10.01 ± 0.64	9.96 ± 0.65	10.09 ± 0.59

Table 3.2: Table of χ^2 minima showing sensitivity of fitting solutions to average mid-target velocity and target position.

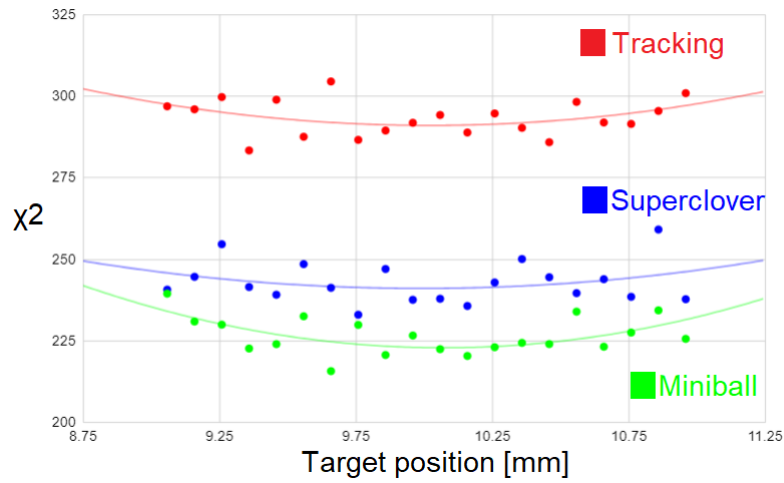


Figure 3.32: χ^2 goodness-of-fit between experimental Doppler corrected ^{131}In gamma-ray energy distribution and combined fitted background and simulated ^{131}In energy distribution from UCHiCARI simulation as a function of longitudinal beamline position from central F8 HiCARI array target position.

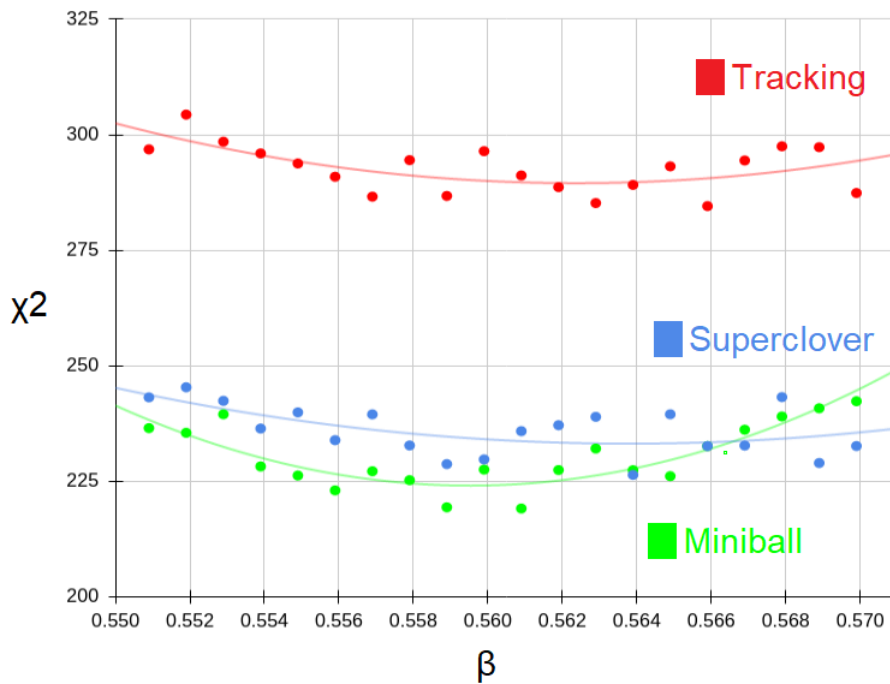


Figure 3.33: χ^2 goodness-of-fit between experimental Doppler corrected ^{131}In gamma-ray energy distribution and combined fitted background and simulated ^{131}In energy distribution from UCHiCARI simulation as a function of average mid target velocity from reconstructed from measured after target velocity and LISE++ simulations. Tracking detector fit in red, Superclover fit in blue, Miniball fit in green.

Target position sensitivity

Before the experiment the target position was measured to be 9.8 mm from the F8 focal point. By fitting the results of the χ^2 fitting tests for simulations using different target positions in figure 3.32 with parabolas, the χ^2 target position minima for each detector fit were obtained. By studying the steepness of these parabolas, 90% confidence interval limits describing the sensitivity of these solutions to different target positions were constructed and as listed along with the minima for each detector fit in table 3.2 [68]. Table 3.2 shows that the target position χ^2 minima are consistent with the measured 9.758mm target position within their 90% confidence limits. This suggests that the target position could shift as much as 0.64mm, 0.65mm or 0.59mm for each detector group respectively and the resulting χ^2 shift from the wrongly reconstructed emission angles (which relies on the assumed target position) could still be explainable as a statistical fluctuation within the 90% confidence intervals.

Mid target velocity sensitivity

The $^{132}\text{Sn} \rightarrow ^{131}\text{In}$ mid-target velocity was reconstructed to be 0.5619c. The χ^2 sensitivity of fits for each detector using different mid target velocities was studied and is plotted in figure 3.33. Similarly, by fitting these results with a parabola, the χ^2 velocity minima and 90% confidence intervals were obtained and are listed in table 3.2 for each detector. Table 3.2 shows that the χ^2 mid target velocity minima are consistent with the reconstructed 0.5619c mid-target velocity within their 90% confidence limits. This suggests that the target position could shift as much as 0.003c, 0.007c or 0.0069c for each detector group respectively and the resulting χ^2 shift from the wrongly reconstructed event based mid-target velocities, which rely on the assumed average mid-target velocity in equation 3.15, could still be explainable as a statistical fluctuation within the 90% confidence intervals.

Fitting uncertainty

Another contribution to the uncertainty with which energies and half-lives can be obtained is the sensitivity of the χ^2 fitting minima to the assumed nuclear structure parameters, determining N_{comb} . By studying the χ^2 matrices in figures 3.29, 3.30 and 3.31 a 2-parameter 90% confidence region can be constructed around the minimum χ^2 solutions. This region is illustrated in red in figure 3.29. While the 2-parameter correlated uncertainty of energy and half-life of the ^{131}In fit is contained within the red region, it is often useful to compress this information into a 1 dimensional single parameter uncertainty by taking upper and lower limits of the surface in each parameter illustrated in black in figure 3.29 [68]. The fitting uncertainties obtained by this method are summarised in table 3.3. These black 1-parameter limits therefore conservatively overestimate the 90% confidence 2-parameter region they contain [68]. The energy and half-life minima obtained in table 3.3 are consistent with the experimentally measured

$\frac{3}{2}^- \rightarrow \frac{1}{2}^-$ 987.8 keV from the previous experiment [65]. The half-lives obtained in each case in table 3.3 are consistent with the prediction of a short lifetime. The consistency of the transition energy obtained with previous results and the alignment of the half-life with expectation suggests the same method may be applied to obtaining transition energies and half-lives in other nuclei within the sample.

Parameter	Miniball	Superclover	Tracking	Combined
Energy [keV]	986.5[+1.5, -2.5]	990.0[+1.0, -5.0]	986.5[+2.0, -2.5]	987 (2)
Half-life [ps]	1.2[+1.8, -1.2]	5[+2, -5]	1[+5.0, -1.0]	<3.2

Table 3.3: Table of energy/half-life χ^2 minima with 1 parameter fitting uncertainty limits and averaged values.

3.5 Studies of the excited states of ^{130}Cd

By expanding the method established and validated in section 3.45, the excited states of ^{130}Cd were studied in the $^{131}\text{In} \rightarrow ^{130}\text{Cd}$ proton knockout reaction channel.

3.5.1 Observed transitions

The Doppler corrected energy spectrum of gamma-rays correlated with ions in the $^{131}\text{In} \rightarrow ^{130}\text{Cd}$ proton knockout reaction channel is plotted in figure 3.34. Transitions are observed in this figure at ~ 1320 keV, ~ 505 keV, ~ 430 keV and ~ 270 keV. In this figure the energy spectrum for each detector subgroup is plotted separately. The ~ 270 keV transition is observed with highest intensity in the forward angle ($22 - 55^\circ$) Miniball detectors. Transitions occurring with significant delay after ^{130}Cd ions are first produced in the secondary target occur further along the outgoing ion trajectory. Gamma-rays which are emitted later in the target or beyond it are emitted closer to the forward angle Miniball detectors and consequently are more efficiently detected. The enhanced intensity of the ~ 270 keV transition in the forward angle Miniball detectors compared to the wider angle Superclover and tracking detectors suggests these gamma-rays may have been emitted after a delay. As illustrated in figure 3.18, for the purpose of reconstructing rest-frame gamma-ray energies, gamma-rays are assumed to be emitted from the middle of the secondary target. If the gamma-rays are instead emitted later or beyond the secondary target the constructed emission angle is erroneously widened. Equation 3.13 shows a wider emission angle results in a lower reconstructed energy. This results in a low energy tail to the observed transitions and a downward shift in the energy centroid as studied in [61].

3.5.2 Constructing the ^{130}Cd level scheme

In a previous experiment 1325 keV and 539 keV transitions were tentatively assigned to $(2^+) \rightarrow (0^+)$ and $(4^+) \rightarrow (2^+)$ transitions between the low lying (2^+) and (4^+) ^{130}Cd excited states [33]. The ~ 1320 keV and ~ 505 keV transitions observed in figure 3.34 are candidates for these previously observed transitions, with the downward shift in energies arising as a consequence of delayed emissions due to the lifetimes of the states. When a high spin states is populated, it can deexcite through a series subsequent gamma-decays each increasingly delayed by the lifetime of the intermediate states. Gamma-rays emitted in these decay cascades thereby exhibit an effective half-life which manifests as multiple, increasingly delayed, lower energy tails. Of the remaining transitions the ~ 430 keV transition is tall and sharp while the ~ 270 keV transition has a long low energy tail. The absence of a low energy tail to the ~ 430 keV transition suggests no connected higher spin states were populated that decay through it. The long low energy tail ~ 270 keV transition however suggests an effective half-life due to a higher-lying connected state and/or a long half-life. The ~ 430 keV and ~ 270 keV transitions were therefore tentatively assigned to $(4^-) \rightarrow (5^-)$ and $(5^-) \rightarrow (4^+)$ transitions connected to newly observed (4^-) and (5^-) states in $\pi(g9/2, p1/2)$ configuration, the next lowest excitation energy states predicted by the shell model calculations in table 2.2. The level scheme suggested by these shell model calculations is illustrated in figure 3.37 next to an experimentally proposed level scheme containing (0^+) , (2^+) , (4^+) , (5^-) and (4^-) states. It is possible that the (5^-) state decays to the previously measured (and lower lying) (6^+) state, forming a second decay branch, however no additional transitions were observed where the shell model excitation energies predict the transition may occur (77 keV). Figure 3.34 shows the energy spectra is dominated by background at these low energies, therefore such a transition may be present but cannot be identified among the present background noise. If the proposed levels are connected as in figure 3.35, transitions between these levels might be observed in time coincidence as multiple gamma-rays are emitted in gamma-decay cascades as ion de-excite to their ground states. The energies of gamma-rays observed in nanosecond time coincidences were studied. There was however inadequate statistics to make conclusions regarding the connection of states on this basis.

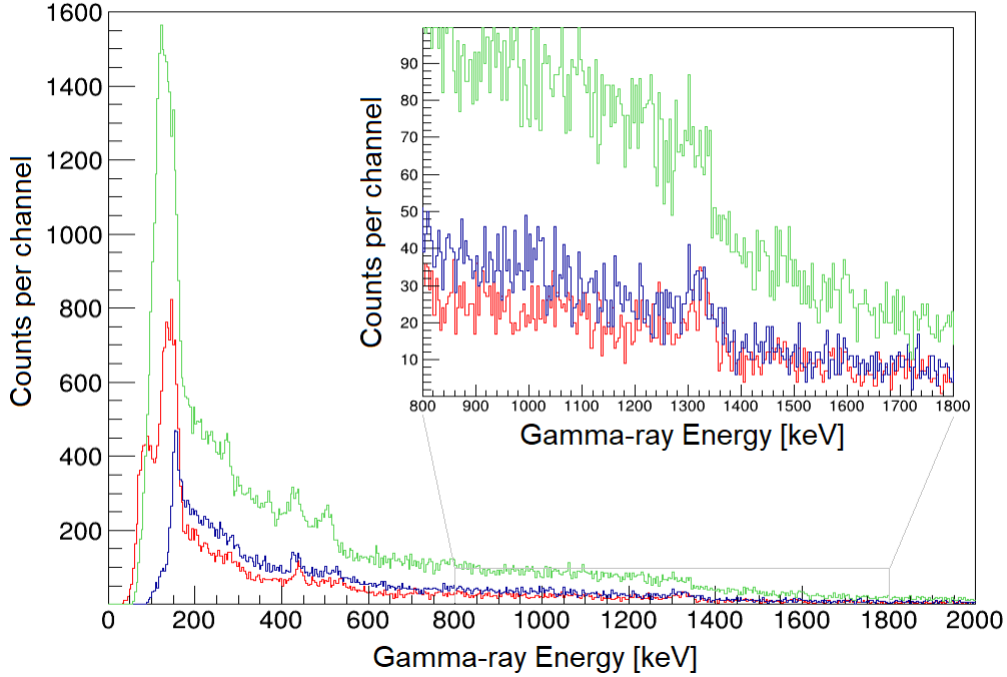


Figure 3.34: Doppler corrected gamma-ray energy histogram for Miniball detectors (green), Superclovers (blue) and tracking detectors (red).

^{130}Cd state population cross sections

In a $^{131}\text{In} \rightarrow ^{130}\text{Cd}$ proton knockout reaction, excited ^{130}Cd nuclei may be produced in a set of n possible excited states [41]. If these excited states are connected in a linear series of decays such as in figure 3.35, a cascade of decays such as

$$n \rightarrow n - 1 \rightarrow n - 2 \rightarrow \dots \rightarrow 1 \rightarrow 0 \quad (3.20)$$

are possible. For a number of populated excited states $N_0, N_1 \dots N_i$ one observes that the decay rate of a given state \dot{N}_i at a time t after the reaction at $t=0$ would depend upon its lifetime τ_i , its population N_i and the population and lifetime of the state above τ_{i+1} and N_{i+1}

$$\dot{N}_i(t) = -\frac{1}{\tau_i}N_i(t) + \frac{1}{\tau_{i+1}}N_{i+1}(t) \quad (3.21)$$

As established in section 3.5.2 the observed transitions in figure 3.34 are likely therefore made up of gamma-rays emitted from the direct population of relevant states and their subsequent decay after a mean lifetime of τ_i as well as subsequent decays delayed by the lifetimes of the states above. In order to extract the half-life and energy of the underlying states from the lineshape of the observed transitions, full decay cascades must be simulated and the cross dependency of state energies and lifetimes studied.

3.5.3 ^{130}Cd decay cascade fitting function

Simulations of the energy distributions ($N_{2+}, N_{4+}, N_{5-}, N_{4-}$) reconstructed from gamma-rays detected in the HiCARI HPGe array due to gamma-decay cascades, arising as

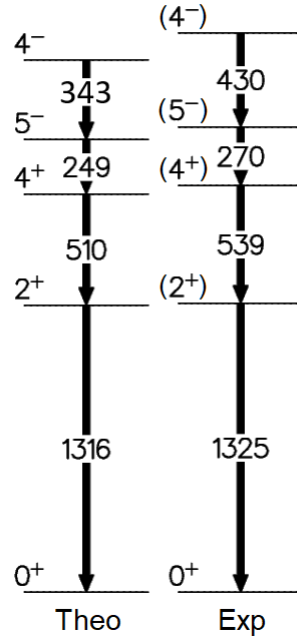


Figure 3.35: ^{130}Cd level scheme constructed on the basis of theoretical calculations (left) and experimental observations of gamma-ray energy peaks (right).

a consequence of the population of simulated (2^+ , 4^+ , 5^- , 4^-) states were produced. These simulations were fitted to the experimental gamma-ray energy histogram by extending equations 3.17 and 3.18 with additional degrees of freedom for the population amplitudes (j_0, j_1, j_2, j_3) of the gamma-ray energy distributions associated with each simulated decay cascade.

$$N_{comb} = k_4 \cdot \text{Erf}\left(\frac{E_{fit} - k_5}{k_6}\right) \cdot (N_{bkg} + j_0 N_{2^+} + j_1 N_{4^+} + j_2 N_{5^-} + j_3 N_{4^-}) \quad (3.22)$$

Here k_i is restricted to $k_i = k_0, k_1, \dots, k_6$. N_{4^-} for example is the simulated energy distribution of Doppler corrected gamma-rays emitted from the decay of the 4^- state, followed by the delayed emission of gamma rays from the 5^- state, 4^+ state and 2^+ state.

Fitted population amplitudes

The population amplitudes (j_0, j_1, j_2, j_3) with which the simulated decay cascade energy distributions are multiplied by in equation 3.22 are obtained with the Minuit fitting algorithm [69]. The population amplitudes fitted in figures 3.38, 3.39 and 3.40 were (j_0, j_1, j_2, j_3) = (60(6), 78(7), 67(14), 100(8)), (60(10), 83(13), 96(24), 100(11)) and (67(10), 97(11), 147(21), 100(11)) for the Miniball, Superclover and tracking detectors respectively. In future investigations state population cross sections are intended to be extracted in this manner by comparing the intensities of simulated gamma-ray energy distributions to experimental intensities. Furthermore, there is an uncertainty associated with the ability of the fitting algorithm to find (j_0, j_1, j_2, j_3) parameters optimal for the fitting the

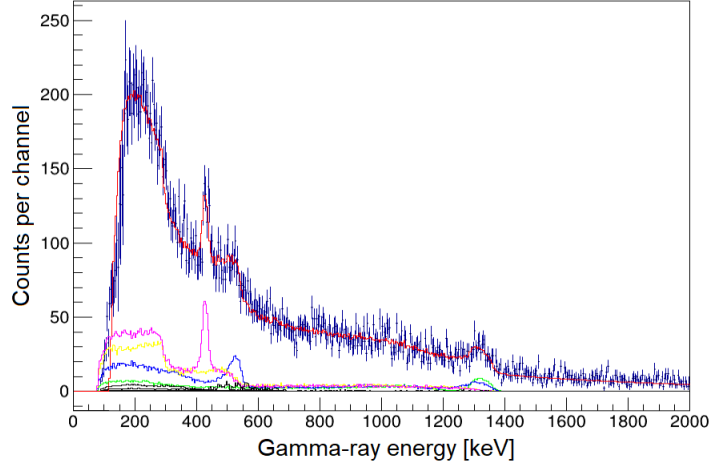


Figure 3.36: ^{130}Cd Doppler corrected gamma-ray energy distributions fitted with combined fitted-backgrounds and simulations of direct population of (2^+) (green), (4^+) (blue), (5^-) (yellow), (4^-) (purple) states for Superclover detectors.

experimental energy distributions to simulated. In future investigations the contribution of uncertainties to the extraction of state energies and half lives is intended to be comprehensively studied and propagated into final results.

3.5.4 Initial parameters for ^{130}Cd gamma-ray energy spectrum fitting

The experimental Miniball, Superclover and tracking detector ^{130}Cd gamma-ray energy spectra were initially fitted by manually fixing the excitation energies of the (2^+) , (4^+) , (5^-) and (4^-) states such that the simulated transition energies were equal to their experimental counterparts. The half-life of each state was then independently and iteratively increased, introducing low energy tails to each simulated transition and reducing the centroid of the energy, while the excitation energies were increased until the lineshape of each transition closely matched the experimentally observed lineshape. The combination of excitation energies and half-lives minimising the χ^2 between the (blue) experimental energy distributions in figures 3.36-3.38 and the fitted (red) distributions was selected as a starting point. The local χ^2 surface in excitation-energy half-life parameter space for each considered state was then independently and systematically studied. The combination of excitation energies and half-life minimising χ^2 for each subgroup of detector and averaged. The results of this systematic and independent search for excitation energy half-life χ^2 minima are the fits shown in figures 3.36-3.38. The reduced chi square (with ν degrees of freedom)

$$\chi^2_{\nu} = \frac{\chi^2}{\nu} \quad (3.23)$$

of these fits were $\chi^2_{\nu_{super}} = 1.08$, $\chi^2_{\nu_{mini}} = 1.53$ and $\chi^2_{\nu_{track}} = 1.22$ in the Superclover, Miniball and tracking detector cases.

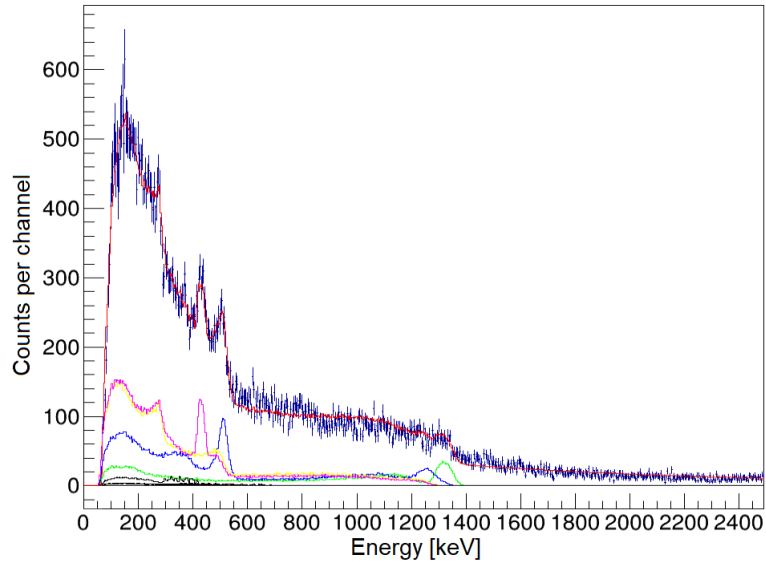


Figure 3.37: ^{130}Cd Doppler corrected gamma-ray energy distributions fitted with combined fitted-backgrounds and simulations of direct population of 2^+ (green), 4^+ (blue), 5^- (yellow), 4^- (purple) states for Miniball detectors.

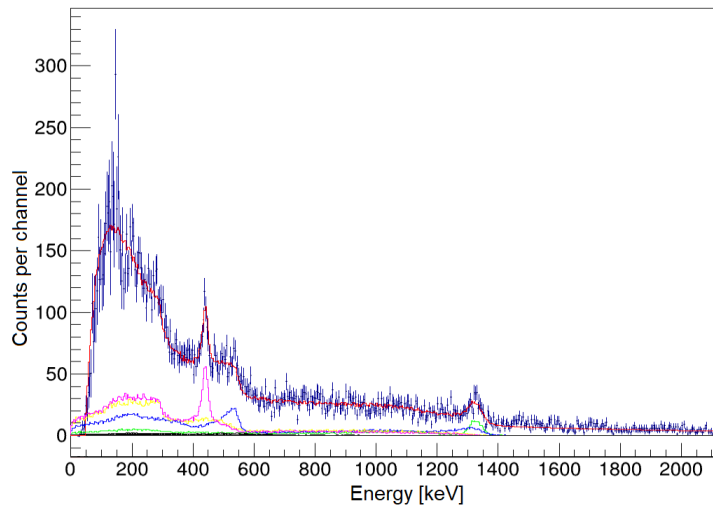


Figure 3.38: ^{130}Cd Doppler corrected gamma-ray energy distributions fitted with combined fitted-backgrounds and simulations of direct population of 2^+ (green), 4^+ (blue), 5^- (yellow), 4^- (purple) states for tracking detectors.

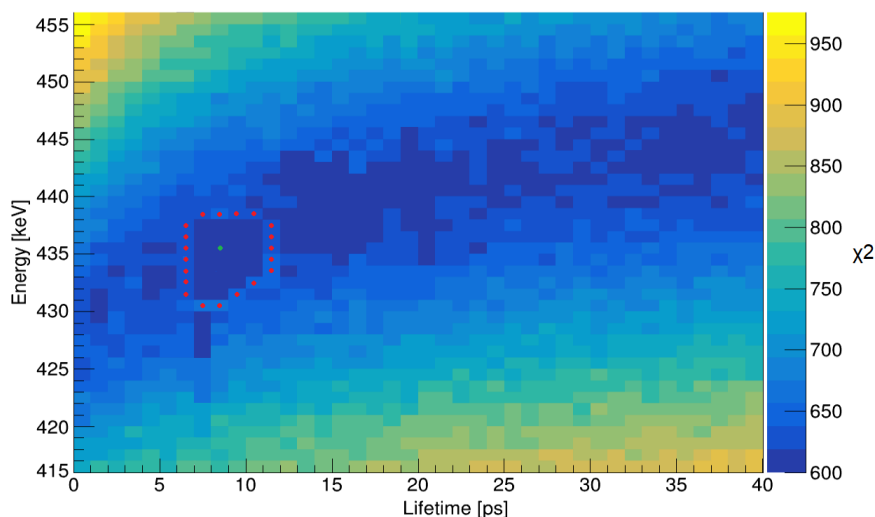


Figure 3.39: χ^2 Miniball fit histogram as a function of ^{130}Cd , $J^\pi = 4^-$ UCHiCARI simulation transition energy and half-life fitted to experimental energy distribution. Labelled with 90% confidence region (red) and χ^2 minimum (green).

3.5.5 Interdependent ^{130}Cd gamma-ray energy spectrum fitting

In the ^{130}Cd level schemes in figure 3.35 there are four states (N_{2^+} , N_{4^+} , N_{5^-} , N_{4^-}) which were considered to be populated with four associated excitation energies (E^{2^+} , E^{4^+} , E^{5^-} , E^{4^-}) and half-lives ($T_{1/2}^{2^+}$, $T_{1/2}^{4^+}$, $T_{1/2}^{5^-}$, $T_{1/2}^{4^-}$). Fixing E^{2^+} and E^{4^+} to 1325 keV and 1864 keV from the previously measured values, these eight degrees of freedom can be reduced to six [33]. As the (4^-) state is assumed to be at the top of the level scheme, no higher lying states was in this case considered to contribute delayed gamma-ray energy components to the gamma-ray energy peak associated with the (4^-) \rightarrow (5^-) transition. The energy E^{4^-} and the half-life $T_{1/2}^{4^-}$ of the (4^-) state are therefore independent of the other nuclear structure parameters and so can be obtained independently of them by varying only E^{4^-} and $T_{1/2}^{4^-}$ and extracting the χ^2 minimum such as in section 3.4.5. Plots of the χ^2 obtained when fitting simulated decay cascades with different combinations of $4^- \rightarrow 5^-$ transition energy and 4^- half-life are shown in figures 3.38-40 for the Miniball, Superclover and tracking detectors respectively. The results of this search summarised in table 3.4. This reduces the interdependent degrees of freedom to (E^{5^-} , $T_{1/2}^{4^+}$, $T_{1/2}^{5^-}$, $T_{1/2}^{2^+}$). As all detector subsystems are fitted independently and the smallest simulated detection efficiency is shown to be $< 1.5\%$ in figure 3.23 for the tracking detectors, UCHiCARI simulations of large numbers of ions and emitted gamma-rays are necessary for adequate numbers of gamma-rays to be detected in each simulated detector for comparison to experimental spectra. If a 100 keV transition energy range was studied in steps of 1 keV around the E^{5^-} excitation energy and 50 ps half-life ranges were studied in steps of 1ps around the remaining ($T_{1/2}^{4^+}$, $T_{1/2}^{5^-}$, $T_{1/2}^{2^+}$) half-life parameters, then 1.25×10^9 UCHiCARI simulations would need to be produced. The computational challenge this presents was logistically unachievable in the available analysis time-frame for a single modern personal computer to perform in a series of simulations therefore the GSI Green-cube

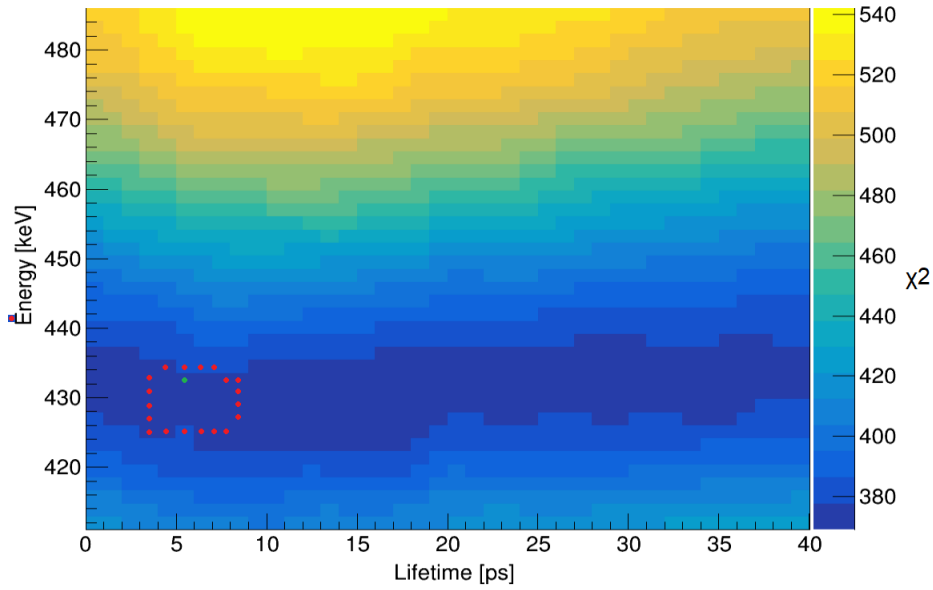


Figure 3.40: χ^2 Superclover fit histogram as a function of ^{130}Cd , $J^\pi = 4^-$ UCHiCARI simulation transition energy and half-life fitted to experimental energy distribution. Labelled with 90% confidence region (red) and χ^2 minimum (green).

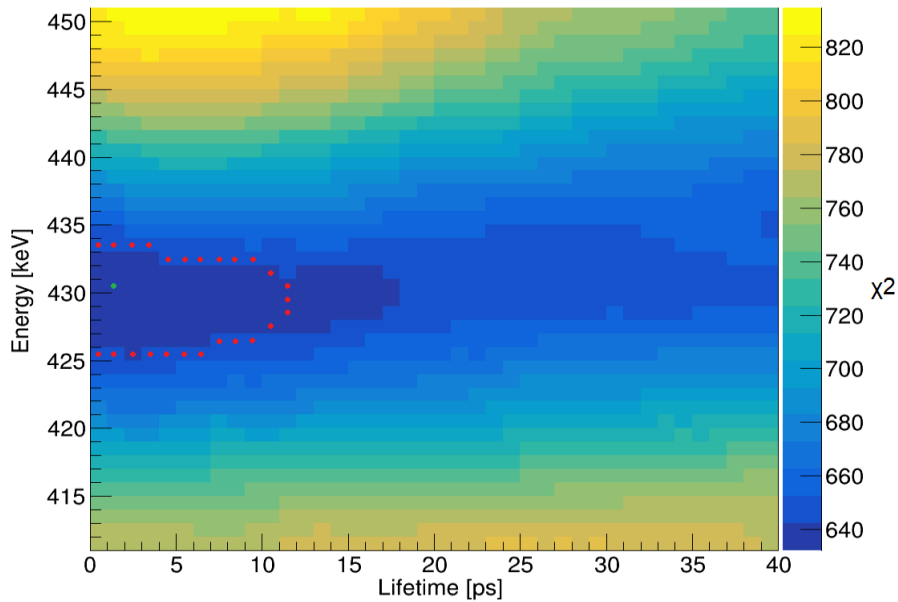


Figure 3.41: χ^2 tracking detector fit histogram as a function of ^{130}Cd , $J^\pi = 4^-$ UCHiCARI simulation transition energy and half-life fitted to experimental energy distribution. Labelled with 90% confidence region (red) and χ^2 minimum (green).

Spin state	Miniball excitation energy [keV]	Superclover excitation energy [keV]	Tracking excitation energy [keV]	Combined excitation energy [keV]
2^+	-	-	-	1325 ^a
4^+	-	-	-	1864 ^a
5^-	2155[+6, -8]	2160[+24, -4]	2163[+14, -10]	2158(5)
4^-	2592[+3, -5]	2588[+1, -4]	2588[+2, -4]	2590(3)
Spin state	Miniball half-life [ps]	Superclover half-life [ps]	Tracking half-life [ps]	Combined half-life [ps]
2^+	1[+1, -1]	5[+2, -5.0]	0[+7, -0.0]	< 2
4^+	160[+60, -40]	100[+100, -100]	60[+100, -20]	117(40)
5^-	480[+40, -120]	430[+140, -80]	460[+60, -180]	463(70)
4^-	8[+2, -1]	5.2[+2, -5]	1[+11, -1]	7(2)

Table 3.4: Table of energy/half-life χ^2 minima with 1 parameter fitting uncertainty limits. ^a excitation energies from [33].

high performance computing cluster was employed to perform these simulations in parallel [69]. The (E^{5^-}, E^{4^-}) , $(T_{1/2}^{2^+}, T_{1/2}^{4^+}, T_{1/2}^{5^-}, T_{1/2}^{4^-})$ minima obtained by independently studying the energy half-life χ^2 surface in section 3.5.4 were (2157, 2591) keV and $\sim (1, 200, 400, 10)$ ps. The $T_{1/2}^{2^+}$ obtained from $(E^{2^+}, T_{1/2}^{2^+})$ parameter space search was 200 times smaller than the $T_{1/2}^{4^+}$ half life obtained from the $(E^{4^+}, T_{1/2}^{4^+})$ parameter space search. The shape of the delayed components of the simulated $(2^+) \rightarrow (0^+)$ transition are therefore dominated by the effective half-life rather than $T_{1/2}^{2^+}$ itself. Consequently the shape of the simulated $(4^-) \rightarrow (5^-) \rightarrow (4^+) \rightarrow (2^+) \rightarrow (0^+)$, $(5^-) \rightarrow (4^+) \rightarrow (2^+) \rightarrow (0^+)$ and $(4^+) \rightarrow (2^+) \rightarrow (0^+)$, decay cascade energy distributions in the $(2^+) \rightarrow (0^+)$ transition energy region (~ 1325 keV) of figure 3.36 (blue, yellow and purple respectively), are relatively insensitive to $T_{1/2}^{2^+}$. $T_{1/2}^{2^+}$ was therefore assumed to be independent of the other parameters. The $\chi^2(E^{2^+}, T_{1/2}^{2^+})$ matrix is shown in figure 3.42 for the Miniball fit. The $T_{1/2}^{2^+}$ half-life minima was extracted from this matrix with 90% confidence 1-parameter limits. The same process was applied to the counterpart Superclover and tracking detector matrices and all the results of all three are combined and summarised in table 3.4 at $T_{1/2}^{2^+}$ was < 2 ps.

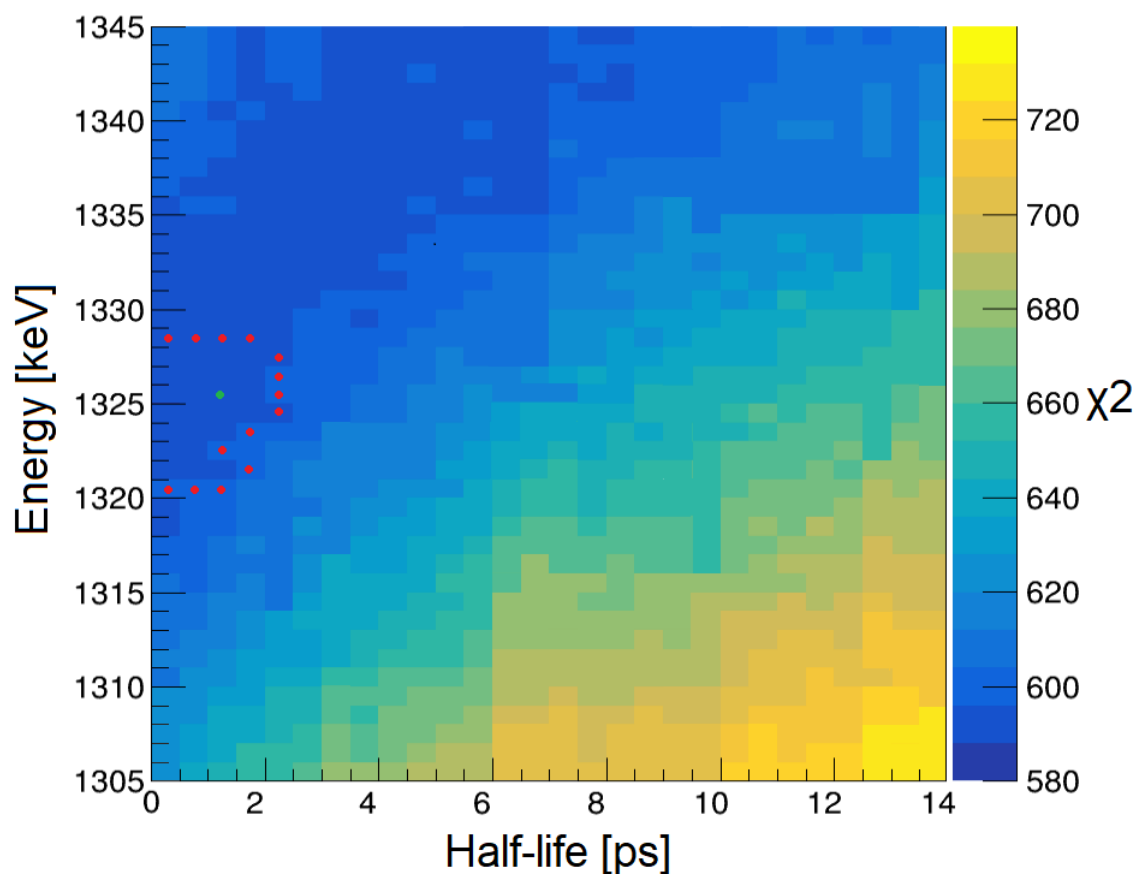


Figure 3.42: χ^2 (2^+) energy half-life matrix for fit of simulated ^{130}Cd UCHiCARI Doppler corrected energy distribution to experimental energy distribution. Labelled with 90% confidence region (red) and χ^2 minimum (green).

3.6 Results of studies of ^{130}Cd

It is difficult to visualise the 4 dimensional volume containing the $(\chi^2, E^{5^-}, T_{1/2}^{4^+}, T_{1/2}^{5^-})$ parameter space studied in the interdependent parameter search. The method of obtaining a 1-parameter uncertainties in section 3.4.5 can however be expanded to 4 dimensions in the ^{130}Cd case. By taking the upper and lower 1-parameter limits surrounding the 4-parameter 90% confidence hyper-surface around the minima, the parameters minimising the χ^2 difference between the UChiCARI simulation and the experimentally obtained ^{130}Cd gamma-ray energy spectra were obtained with uncertainties and are summarised in table 3.4. The independently obtained $T_{1/2}^{2^+}$ minima and the independently obtained $(E^{4^-}, T_{1/2}^{4^-})$ combination minima are also summarised in table 3.4 with corresponding fitting uncertainties. By taking the average of the parameters obtained for each detector weighted by their uncertainties, final excitation energies and half-lives for the (2^+) , (4^+) , (5^-) , (4^-) states were obtained and are summarised in table 3.4 [70]. The errors in table 3.4 for the ^{130}Cd case for each detector group are asymmetrical in nature. For convenience of presentation these asymmetrical errors are symmetrised using the method presented in [71]. Using these combined excitation energies and half-lives a new ^{130}Cd level scheme was constructed and is plotted in figure 3.43 and is combined with the result for the previously observed $J^\pi = (2^+), (4^+), (6^+), (8^+)$ states [33].

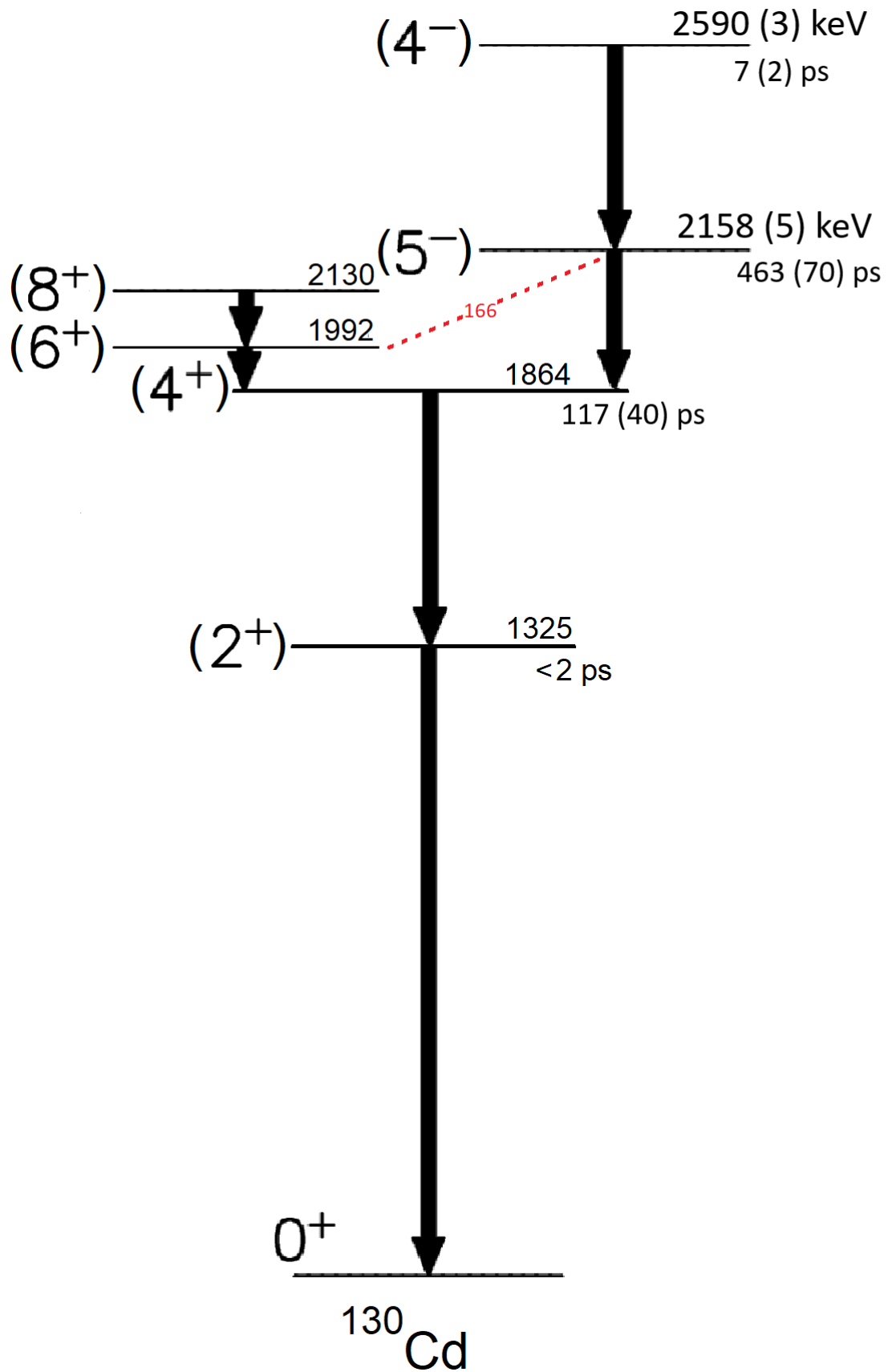


Figure 3.43: Proposed ^{130}Cd level scheme including excitation energies for (2^+) , (4^+) , (6^+) , (8^+) states from previous experiment [33]. Excitation energies for (4^-) , (5^-) states and (2^+) , (4^+) , (4^-) , (5^-) half-lives from averaged solutions in table 3.4. Unobserved 166 keV $(5^-) \rightarrow (6^+)$ transition labelled in red.

Experimental transition	$B(E/M\lambda)$ [$e^2 fm^{2\lambda} / \mu_N^2 fm^{2\lambda-2}$]	$B(E/M\lambda)/B(E/M\lambda)_{s,p}$ [Wu]
$B(E2; (2^+) \rightarrow 0^+)$	> 62	> 1.76
$B(E2; (4^+) \rightarrow (2^+))$	$106[+47, -25]$	$2.72[+1.2, -0.64]$
$B(E1; (5^-) \rightarrow (4^+))$	$4.2[+0.66 - 0.5] \times 10^{-4}$	$2.6[+0.4, -0.3] \times 10^{-6}$
$B(M1; (4^-) \rightarrow (5^-))$	$0.37[+0.08, -0.06]$	$0.21[+0.03, -0.05]$

Table 3.5: Table of experimental ^{130}Cd reduced transition probabilities based on proposed level scheme in figure 3.45.

Theoretical transition	$B(E/M\lambda)$ [$e^2 fm^{2\lambda} / \mu_N^2 fm^{2\lambda-2}$]	$B(E/M\lambda)/B(E/M\lambda)_{s,p}$ [Wu]
$B(E2; 2^+ \rightarrow 0^+)$	143.0	3.66
$B(E2; 4^+ \rightarrow 0^+)$	161.4	4.13
$B(E1; 5^- \rightarrow 4^+)$	-	-
$B(M1; 4^- \rightarrow 5^-)$	0.2439	0.136

Table 3.6: Table of theoretical ^{130}Cd reduced transition probabilities calculated in Oxbash [34].

3.6.1 Strengths of transitions between excited states of ^{130}Cd .

By substituting the energies half-lives of the transitions in table 3.4 into equations 2.2, 2.21 and 2.23, and assuming purity of the lowest order multipolarity (i.e pure E1, M1 and E2 in each case) the reduced transition probabilities in table 3.5 were calculated. In order to interpret these reduced transition probabilities it can be useful to convert them into Weisskopf units for the strength of a single-particle transition $B(E/M\lambda)_{s,p}$ between an initial I_i and a final I_f state for electric and magnetic single particle transitions of λ multipolarity respectively at $A = 130$ for ^{130}Cd [73].

$$B(E\lambda; I_i \rightarrow I_f) = \frac{(1.2^{2\lambda})}{4\pi} \left(\frac{3}{\lambda+3}\right)^2 A^{2\lambda/3} e^2 (fm)^{2\lambda} \quad (3.24)$$

$$B(M\lambda; I_i \rightarrow I_f) = \frac{10}{\pi} (1.2)^{2\lambda} \frac{3}{\lambda+3}^2 A^{2\lambda-\frac{2}{3}} \mu_N^2 (fm)^{2\lambda-2} \quad (3.25)$$

By evaluating these equations for the relevant E1, M1 and E2 transitions

$$B(E1; I_i \rightarrow I_f) = 0.06446 A^{2/3} e^2 fm^2 \quad (3.26)$$

$$B(E2; I_i \rightarrow I_f) = 5.94 \times 10^{-2} A^{4/3} e^2 (fm)^4 \quad (3.27)$$

$$B(M1; I_i \rightarrow I_f) = 1.79 \mu_N^2 \quad (3.28)$$

the reduced transition strengths in table 3.5 in each case were calculated.

3.7 Discussion of ^{130}Cd results

3.7.1 Excitation energies

In a previous experiment 1325 keV and 539 keV transitions were tentatively assigned to $(2^+) \rightarrow (0^+)$ and $(4^+) \rightarrow (2^+)$ ^{130}Cd transitions [33]. In this experiment newly observed transitions ~ 270 keV and ~ 430 keV were tentatively assigned to $(5^-) \rightarrow (4^+)$ and $(4^-) \rightarrow (5^-)$ transitions. By combining these experimental transition energies and constructing the level scheme in figure 3.45, the excitation energies of ^{130}Cd (2^+) , (4^+) , (5^-) , (4^-) states can be compared to the theoretical excitation energies presented in table 2.2 [34]. In these Oxbash shell model calculations an inert ^{132}Sn core was assumed and excited states of ^{130}Cd in the $\pi(f_{7/2}, p_{3/2}, p_{1/2}, g_{1/2})$ and $\nu(g_{7/2}, d_{5/2}, d_{3/2}, s_{1/2}, h_{11/2})$ orbital model space were computed in the presence of this core with the Na22 interaction [33]. Of particular importance are the $\pi(g_{9/2})$ and $\pi(p_{1/2})$ orbitals which form $J^\pi = 2^+, 4^+, 5^-, 4^-$ states with excitation energies of residual energy difference +9, +39, +84 and +173 keV respectively from the experimental energies. The Na22 interaction contains effective nucleon-nucleon matrix elements first applied in [74] based on the realistic CD-Bonn nucleon-nucleon potential using the methods outlined in [74][75]. As shown in figure 2.7, the single particle energies originally used in [33] have since been updated to include the newly measured $(\pi f_{7/2})$ single particle energy [38]. The calculations well reproduce the excitation energies of the previously observed (2^+) and (4^+) $\pi(g_{9/2}, g_{9/2})$ states and under-predict the excitation energies of the higher lying (5^-) and (4^-) $\pi(g_{9/2}, p_{1/2})$ states. The enhanced accuracy of the predicted 2^+ and 4^+ excitation energies compared to the (5^-) and (4^-) states could therefore be due to the fact that the $\pi(g_{9/2}, g_{9/2})$ interaction has been modified in view of other experimentally observed $\pi(g_{9/2}, g_{9/2})$ states while the interaction of $\pi(g_{9/2}, p_{1/2})$ orbitals where spectroscopic information is sparse has not since the interaction was originally developed [33][73].

3.7.2 Transition strengths

In the Oxbash shell model calculations an effective proton and neutron charge of 1.5e and 0.5e respectively were used (as in [33]) to account for the contributions of orbitals outside the considered model space. With these effective charges $B(E2; 2^+ \rightarrow 0^+)$, $B(E2; 4^+ \rightarrow 2^+)$, $B(E1; 5^- \rightarrow 4^+)$ and $B(M1; 4^- \rightarrow 5^-)$ were computed and are summarised in table 3.6 [34]. By comparing table 3.5 and 3.6 one observes that the experimentally determined reduced transition probabilities are well reproduced for the $B(E2; 2^+ \rightarrow 0^+)$ and $B(E2; 4^+ \rightarrow 2^+)$ transitions between the $\pi(g_{9/2}, g_{9/2})$ 2^+ and 4^+ states. The reduced transition probability for the $B(M1; 4^- \rightarrow 5^-)$ transition meanwhile is less well reproduced, differing from the experimentally determined value, but still within the order of magnitude. With only the 1-body electromagnetic operator the experimental $B(E1; 5^- \rightarrow 4^+) = 2.6[+0.4, -0.3] \times 10^{-6} e^2 f m^2$ from table 3.5 is an l-forbidden transition. This transition may therefore be best interpreted in the context of other $E1((5^-) \rightarrow (4^+))$ transitions in proximity to the closed ^{132}Sn core

instead of the shell-model calculations in which these transitions are not allowed. A $B(E1, 5^- \rightarrow (4^+)) = 3.6 \times 10^{-6} e^2 fm^2$ reduced transition strength for example has been observed in ^{130}Sn [76] and a $B(E1, 5^- \rightarrow (4^+)) = 8.4 \times 10^{-5} e^2 fm^2$ was also observed in doubly magic ^{132}Sn [77]. The newly observed $B(E1(5^- \rightarrow 4^+))$ reduced transition probability in ^{130}Cd is within the range of these considered $B(E1)$ transitions suggesting it is of similar strength to previously observed transitions within the region.

Interpretation of (2^+) and (4^+) excitation energies.

The ratio of the excitation energies of the first (2^+) and (4^+) excitation energies in even-even nuclei is significant because it can be used as a metric to gauge the degree of collectivity of a nucleus [29]. The neutron capture cross section is also particularly sensitive to the degree of quadrupole deformation a nucleus exhibits with low cross sections for low quadrupole collectivity [78]. This is especially relevant for ^{130}Cd as an r-process waiting point nucleus, as the nature of its collectivity and its neutron capture cross section determines the rate at which the r-process proceeds through it. Nuclei engaging in collective motions have $E(4^+)/E(2^+) \sim 2$ and $E(4^+)/E(2^+) \sim 3.3$ for vibrational and rotational motions respectively [79]. The excitation energies in table 3.4 for the tentatively assigned 2^+ and 4^+ states from prior experiments have $E(4^+)/E(2^+) = 1.4$. This ratio suggests ^{130}Cd is a spherical nucleus exhibiting neither a vibrational nor rotational characteristics.

3.7.3 Summary of ^{130}Cd results

Comparison of newly determined $B(E2; 2^+ \rightarrow 0^+)$ and $B(E2; 4^+ \rightarrow 2^+)$ reduced transition probabilities to shell model calculations show good agreement. Comparison of the strength of a newly observed $(4^-) \rightarrow (5^-)$ transition involving $\pi(g_{\frac{9}{2}}, p_{\frac{1}{2}})$ configurations to the strength predicted by this model also shows agreement. The newly observed $(4^-) \rightarrow (5^-)$ transition meanwhile was shown to have a similar strength to comparable E1 transitions in surrounding nuclei [76][77]. As expected, the excitation energies predicted for the 4^- and 5^- ^{130}Cd states in $\pi(g_{\frac{9}{2}}, p_{\frac{1}{2}})$ configurations show less agreement with experimentally determined values than the energies of 2^+ and 4^+ states in $\pi(g_{9/2}, g_{9/2})$ configurations for which there is a wealth of experimental information available with which to construct the Na22 interaction [73][33]. Analysis of the $E(4^+)/E(2^+)$ ratio suggests ^{130}Cd is a spherical nucleus with no evidence of quadrupole collectivity. The shell model Na22 interaction is very successful in describing the excited states of ^{130}Cd . This is demonstrated in the accurate prediction of the properties of the previously observed energies of low-lying ^{130}Cd states and the newly determined excitation energies of (4^-) and (5^-) excited states and $(4^-) \rightarrow (5^-)$ and $(5^-) \rightarrow (4^+)$ transition strengths. The nuclear structure of ^{130}Cd is therefore well theoretically understood, with possible adjustments to the $\pi(g_{9/2}, p_{1/2})$ interaction justified by the less good theoretical agreement with the experimentally determined excitation energies of (4^-) and (5^-) $\pi(g_{\frac{9}{2}}, p_{\frac{1}{2}})$ states than the 2^+ and 4^+ $\pi(g_{\frac{9}{2}}, g_{\frac{9}{2}})$ states.

Chapter 4

Simulations for HISPEC Slowed Down Beam Campaign

4.1 Slowed down beam experiments at FAIR

The Facility for Antiproton and Ion Research (FAIR) facility is a new accelerator facility designed to facilitate research in the fields of nuclear, hadronic, particle, atomic and anti-matter physics [80]. The construction of the FAIR facility began with upgrades to the existing UNILAC linear accelerator and ion source at GSI in 2004, increasing available ion beam currents from hydrogen to Uranium up to 10^{12} p/s $^{238}\text{U}^{28+}$ beams in the heavy mass range [81]. The higher beam intensities provided by the upgraded UNILAC will feed a new heavy ion synchrotron (SIS100) capable of accelerating heavy ion beams to higher energies with many times lower beam intensity loss than achievable with the current GSI synchrotron. Elements as heavy as Uranium can be produced by the GSI ion source [82]. These accelerated beams can then be delivered to the SuperFRS (Superconducting magnetic FRagment Separator) with GeV/u energies depending on the ion species and charge state [12]. In the SuperFRS these high energy and high intensity primary beams can be impinged on production targets undergoing reactions such as abrasion-fission to produce rare-isotope beams [36]. The SuperFRS at FAIR will thereby provide the wide range of globally preeminent rare-isotope beam intensities illustrated in figure 4.1 [83]. High-Resolution In-Flight Spectroscopy (HISPEC) Slowed Down Beam (SDB) experiments are gamma-spectroscopy experiments designed to study the nuclear structure of rare-isotope beams delivered by the SuperFRS [12][83]. SDB experiments will target light and dark green nuclei in figure 4.1 which can be produced with $10^4 - 10^7$ p/s beam intensities. This includes nuclei in singly and doubly magic mass regions up to $N=126$ with particular emphasis on neutron-rich nuclei for which spectroscopic information is scarce aside from ground state and decay properties. In multi-step coulomb excitations the nuclear structure of these rare-isotope beams can be excited for study and in direct and fusion evaporation reactions more exotic secondary products can be produced and studied [84]. By detecting the gamma-decays of these nuclei in the AGATA (Advanced GAMMA Tracking Array) HPGe array the excitation

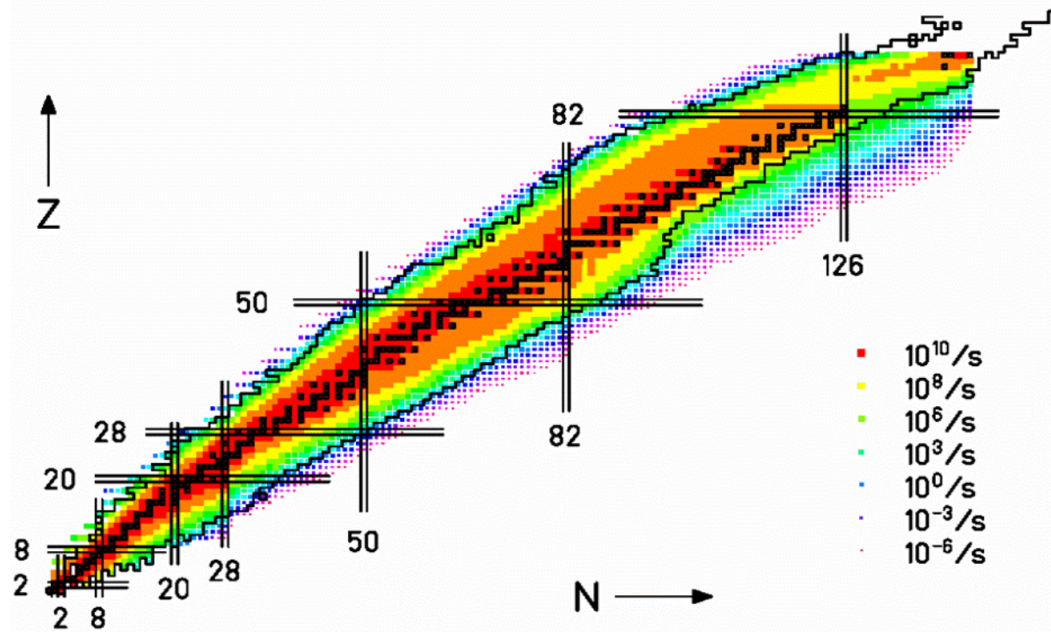


Figure 4.1: Plot of atomic number and atomic mass of beam species available for study in HISPEC experiments coloured by achievable beam intensity [83]

energies of excited states and the strengths of transitions between them can be measured [85]. From this information the underlying single particle structure and deformation degrees of freedom which drive structural evolution can be studied [84]. In this chapter the feasibility of SDB in-flight gamma-spectroscopy experiments studying the excited states of nuclei in multi-step Coulomb excitation interactions is evaluated and the required performance of SDB detectors for a future SDB experiments are investigated.

4.1.1 Low energy coulomb Excitation

As shown in figure 4.2 the cross section for an example case of the single 2^+ and multi-step 4^+ coulomb excitation of a ^{74}Zn projectile with a ^{208}Pb target is maximised just below the coulomb barrier [86]. This is because, as explained in section 2.5.1, at beam energies well below the Cline-condition energy in equation 2.27, the nuclear surfaces of colliding nuclei cannot come close enough for nuclear processes such as fusions to begin competing with Coulomb excitations [39]. SDB multi-step Coulomb excitation experiments are therefore optimised to target this enhanced cross section at low energies [84].

4.2 Slowing down ions in SDB experiments

The SuperFRS can only produce, magnetically separate and transport rare-isotope beams with minimum kinetic energies of a few hundred MeV/u [12]. Once delivered to SDB experiments, these SuperFRS beams must be therefore slowed down to the targeted Coulomb barrier energies [87]. As shown in figure 4.3 the beam (entering left) is first

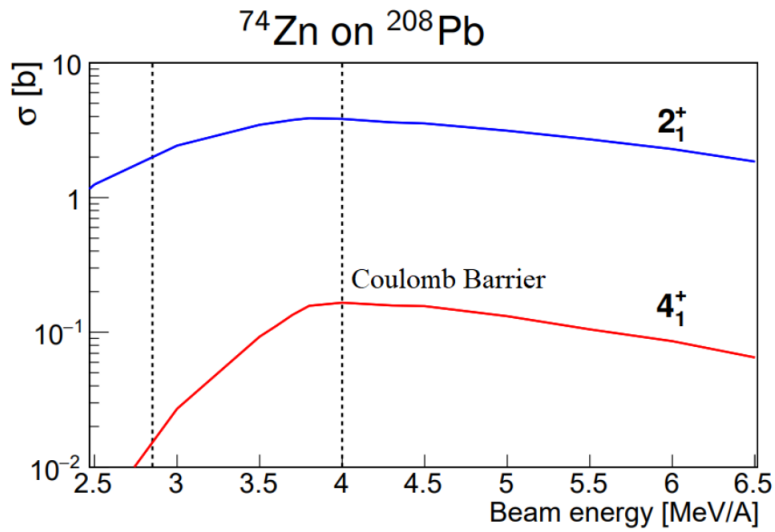


Figure 4.2: Single and multi step Coulomb projectile excitation cross section of ^{74}Zn on a ^{208}Pb target. Modified version of plot from [86].

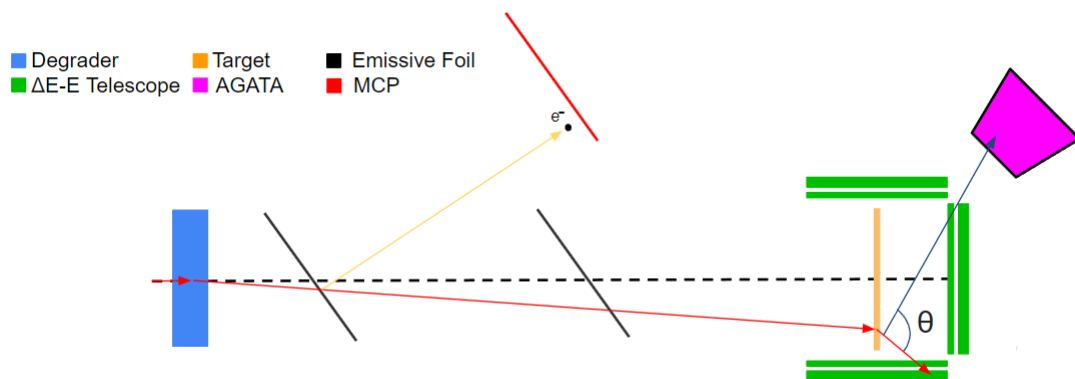


Figure 4.3: Illustration of SDB experiment including degrader (blue), two emmissive foils (black), from which secondary electrons and knocked into tracking detectors (red) as well as DSSSD $\Delta E - E$ telescope (green), target (gold) and a AGATA crystal (purple). Gamma-ray emission angle between ion scattering angle from target into DSSSD and AGATA gamma-ray hit position.

therefore impinged on the thick (typically 3000-4000 mg/cm² Al) degrader shown in blue [87]. In the ^{74}Zn projectile ^{208}Pb target case the Coulomb barrier is 3.4MeV/u. The sharp deceleration of in this case ^{74}Zn ions from hundreds of MeV/u to 3.4MeV/u is important for SDB experiments as the slowing process introduces many challenges which must be addressed with special effort.

4.3 Particle identification in SDB experiments

As ions slow down in the thick degrader they can engage in secondary reactions, meaning they must be identified after the degrader so that detected gamma-rays from which nuclear structure information can be extracted can be correlated with ions of known species [76]. For this purpose a procedure for identifying the atomic mass and atomic number of post-degrader ions is presented in this section.

4.3.1 Mass reconstruction

In order to reconstruct the mass of post-degrader ions, ions next travel through the pair of thin foils illustrated in black in figure 4.3 after the degrader. As ions traverse these foils, they knockout secondary electrons (yellow) which are accelerated by a grid of electrostatic wires into a drift volume [87]. This drift volume is enclosed by a homogeneous and longitudinal magnetic field which drives the electrons in tight helical spirals through the volume to the surface of Micro-Channel Plate (MCP) detectors illustrated in red [88]. Using the timings and energies of charge deposited by electrons in the electronically segmented surface of the MCPs, the timings and the positions of the passage of the original ions through the thin foils can be reconstructed. By taking the magnitude of the path length $|\vec{X}|$ traversed between these positions and the time taken $t_2 - t_1$ between the hits, the velocity of ions through the foils β_{foil} can be reconstructed with

$$\beta_{foil} = \frac{|\vec{X}|}{c(t_2 - t_1)} \quad (4.1)$$

After travelling through the secondary target (illustrated in gold) and engaging the Coulomb excitations, the ions scatter into a doubly layered array (illustrated in green) of Double-Sided Silicon Strip Detectors (DSSSDs) in which they are fully stopped and their total kinetic energy is recorded [56]. By comparing the total kinetic energy E_{DSSSD} absorbed in the DSSSDs (coloured green in figure 4.3) to an extrapolation of the velocity reconstructed from the MCPs through the target β_{ext}

$$m_0 = \frac{2E_{DSSSD}}{c^2\beta_{ext}^2} \quad (4.2)$$

the rest mass m_0 of post-degrader ions is reconstructed. The target is intended to be thin at a few mg/cm^2 [87]. The velocity lost by ions travelling through the target is therefore small however β_{loss} correction using stopping powers from a LISE++ simulation is still

applied [65]. This takes into account the total thickness traversed by the ion on its incoming and outgoing target scattering angles with

$$\beta_{ext} = \beta_{foil} - \beta_{loss} \quad (4.3)$$

4.3.2 Atomic number reconstruction

The Bethe-Bloch equation in equation 3.7 shows that the energy deposited by an ion in a given thickness of a material depends upon its velocity and its atomic number. The SDB DSSSD array consists of two layers, a thin 20 μm layer which samples the kinetic energy deposited by traversing ions and a thick 300 μm layer that fully stops ions and captures their remaining kinetic energy. In accordance with equation 3.7, ions with different atomic number (and therefore stopping power dE/dX) take on distinct and separable curves in $(\Delta E - E)$ space. The atomic number of ions can therefore be identified by with a $\Delta E - E$ selection in the $\Delta E - E$ method [87].

4.4 SDB kinematics and Doppler correction

Another challenge exacerbated by the slowing down process is the kinematic reconstruction of post-degrader ions necessary for reconstruction of rest-frame gamma-ray energies from the Doppler shifted energies detected in the laboratory-frame by AGATA [87].

4.4.1 Reconstructing emission angles

As illustrated in figure 4.3 ions engaging in Coulomb excitations are scattered into the DSSSD array at wide Rutherford scattering angles in the semi-classical approximation established in section 2.5 [39]. At low (Coulomb barrier) energies, excited states with short lifetimes gamma-decay within or shortly thereafter the target. Gamma-rays in transitions between these states are detected in the surrounding AGATA array. In order to reconstruct rest-frame gamma-ray energies E_0 from the Doppler shifted energy in the laboratory-frame that gamma-rays are detected with in AGATA, the emission angle θ_γ with which each gamma-ray is emitted must be reconstructed. θ_γ is reconstructed by taking the angle between the direction from the point of emission to the position with which the gamma-ray is recorded as hitting AGATA and the direction from the emission vertex to the position with which an ion is recorded as hitting the DSSSDs.

4.4.2 Measuring transition strengths in SDB experiments

With a $3.86\text{mg}/\text{cm}^2$ (2 μm) ^{197}Au target such as might be used in a SDB experiment, the excitation site can be assumed midway through the target with only a maximum 1 μm longitudinal offset from the real reaction vertex. Similarly there is an offset between where the ion is excited and the gamma-ray emission vertex, depending upon how long

lived the state is before it gamma-decays. At Coulomb barrier energies an example ^{64}Ni projectiles travelling at $0.0949c$ and which is excited to its first 2^+ or 4^+ excited state would travel $30.9\mu\text{m}$ or $16.5\mu\text{m}$ respectively before half would gamma-decay with 1.086ps and 1.73ps half-lives respectively [89][90][91]. If states with short half-lives like these are populated, the emission vertex is therefore very close to the reaction vertex. If the emission vertex were also assumed to be in the middle of the target, the offset from the real emission vertex is likely to be small, meaning θ_γ is close to accurate and the gamma-ray energy is reconstructed at the rest-frame energy. A fictitious state with a 100ps half-life would travel 2.8mm however, offsetting the real emission vertex from the assumed and resulting in the shifting and warping of the gamma-ray energy peak in accordance with equation 3.13. The half-life dependence on the shape and position of gamma-ray energy peaks is advantageous because it can be exploited similarly as presented in section 3.4.5 in HiCARI experiments in order to extract the strength of the transitions the gamma-rays are emitted in.

4.4.3 Angular straggling

Detector and target positioning

As incident ions slow in degrader they encounter angular straggling and the beam becomes defocused [87]. The most immediate problem is the separation between the degrader and the target in figure 4.3. As the target is positioned 2-3 m downstream from the degrader, the defocused beam can spread out and the target must be therefore be positioned close enough to ensure it captures sufficient ions for Coulomb excitations. The dominant contribution to this length is the separation between the emissive foils in black in figure 4.3. The absolute uncertainty in the velocity reconstructed from the MCP tracking detectors depends upon their separation and the consequent absolute time-of-flight $t_2 - t_1$ and path length $|\vec{X}|$. $\Delta\beta$ precision is important because it ultimately contributes to the energy uncertainty ΔE_0 in equation 3.14 with which rest-frame gamma-ray energies can be reconstructed and the precision with which the rest mass m_0 can be reconstructed from the extrapolated velocity with $1/\beta_{ext}^2$ dependence in equation 4.2. Increased distance between the thin foils is therefore optimal for reducing velocity uncertainty. The SDB target however must be small enough to fit within the radial interior AGATA of the spherical AGATA array with radius of 22.5cm [12]. As the target can only be as big as can fit inside the AGATA array, the target must be brought sufficiently close to the degrader for it to capture the defocused beam for Coulomb excitations. This leads to a competition between the achievable intrinsic position and timing performance of the MCPs, which limits the minimum MCP separation for adequate ion identification and gamma-ray Doppler correction and the number of ions hitting the target which can engage in Coulomb excitations.

SDB kinematic reconstruction for Doppler corrections

In order to reconstruct the mid-target position (and therefore the assumed excitation vertex) traversed by the beam, its trajectory must be reconstructed after the degrader as in section 4.3.1 using the MCPs. The emission vertex is assumed to be the same as the excitation vertex, half way through the target, and therefore a mid-target velocity must also be determined. Similarly to in section 4.3.1, the post-degrader velocity and trajectory are reconstructed from the MCPs, then the velocity is extrapolated only halfway into the target and a correction is made for the energy it would have on average lost on its incoming angle through the target to the longitudinal middle. As shown in equation 3.14, the uncertainty with which rest-frame E_0 gamma-ray energies can be reconstructed depends on the reconstructed ion velocity $\Delta\beta$ and emission angle $\Delta\theta$ uncertainty. The uncertainty additionally depends upon the intrinsic energy resolution of AGATA ΔE_γ as well as the AGATA gamma-ray hit position resolution with which $\Delta\theta$ is constructed. In 2020 the performance of the AGATA array was studied and 1.3 keV energy and 2mm (1-sigma) hit position resolutions were extracted.

4.5 HPGe Background Discrimination

As ions decelerate in the degrader and later the target, part of their kinetic energy is converted into Bremsstrahlung radiation and the remainder is converted as they fully stop in the DSSSDs. In order for gamma-ray energy transition peaks to be identified in the first place they must be discriminated from this Bremsstrahlung radiation as well as other natural background, cosmic or environmental [67][87].

4.5.1 Shielding

As the majority of deceleration occurs in the degrader, the majority of the Bremsstrahlung radiation is emitted from this degrader [87] The erection of a wall of (lead) shielding at outgoing beam angles from the degrader would absorb much of the emitted low energy background, reducing the intensity of Bremsstrahlung radiation reaching the downstream HPGe detectors. The low angles along which ions travel to the target from the degrader cannot be shielded however without blocking the path of the ions. Furthermore, this shielding has a maximum logistically feasible thickness through some radiation will statistically still penetrate. Beyond reducing the intensity of Bremsstrahlung radiation reaching the HPGe detectors, in this section hardware data acquisition conditions during the experiment and software analysis conditions on the collected data are presented which may be capable of suppressing the remaining background.

4.5.2 Timing conditions

Firstly, as the Bremsstrahlung radiation emitted from the degrader travels at the speed of light it arrives in AGATA before gamma-rays of interest are emitted by ions excited in the target which travel at lower velocity from the degrader. A Coulomb barrier ^{64}Ni beam travelling at $0.0949c$ would take 70 ns to traverse a 2m distance such one might separate the degrader and target depending on the thin foil separation. Bremsstrahlung x-rays would however travel a 2 m distance in only 6.7 ns at the speed of light. The timing resolution of modern HPGe detectors is ~ 20 ns therefore x-rays arriving after 6.7ns may be distinguishable from gamma-rays arriving 63.3 ns later. This depends upon the spread of angles over which the Bremsstrahlung radiation and ions are emitted from the degrader. The wider the angle, the longer the path taken to hit the downstream AGATA array directly, or to hit the target, become excited, gamma-decay and wait for the emitted gamma-ray to hit the array in the case of the ions. Depending upon these distributions, degrader-target separation and the velocity of the projectile, an online hardware condition excluding the acquisition HPGe data before a period has elapsed between the passage of ions through a timing detector before the degrader or a thin foil after could be applied. A more stringent software condition could also be applied after the experiment, taking into account angular straggling of the beam in the target and the resultantly increased delay before the arrival of ions in the target.

4.5.3 Ion kinematics conditions

As established in section 2.5, at low (Coulomb barrier) energies excited ions are scattered at large Rutherford scattering angles [39]. By positioning the DSSSDs only at wide scattering angles from the target and choosing only to acquire data in instances where ions are detected in these large angles DSSSDs with a hardware condition, natural backgrounds uncorrelated to the ions of interest would be suppressed leaving only natural backgrounds that are randomly coincident. In addition, a software selection on the energy and scattering angle of detected ions could be applied, suppressing ions which are detected with kinematics inconsistent with having undergone excitations in inelastic collisions.

4.6 Estimated Required Detector performances

Early SDB developments proceeded with simulations and test experiments aimed at estimating required detector performance and the development of suitable detectors on this basis [93][94]. In 2007 the transport of ^{62}Co ions through the GSI FRS and the slowing of these ions to 10 MeV/u in an Al degrader was simulated [94]. These Monte-carlo MOCADI simulations relied upon the ATIMA energy loss and angular straggling code and EPAX cross sections for secondary degrader reactions [95][96]. The accuracy of the simulated angular straggling, secondary reaction cross sections and post-degrader beam energy distribution was validated in comparison to a 2010

Detector	Energy resolution	Timing resolution	Position resolution
MCPs	-	120ps	1mm
DSSSDs	3%	100ps	1mm
AGATA	1.3keV	~ 20ns	2mm

Table 4.1: Table of estimated SDB MCP and DSSSD intrinsic detector performance requirements [87][96]. Achieved AGATA intrinsic energy and position reconstruction performance from [92].

SDB text experiment slowing a ^{64}Ni beam down from 250 MeV/u to 13 MeV/u in a $3.95\text{g}/\text{cm}^2$ degrader [93]. In 2011 detector performance requirements estimated on the basis of these test experiments and simulations were presented and later published in the HISPEC/DESPEC infrastructure report for FAIR. [87][96]. As summarised in table 4.1 by studying the simulated separation of elements achieved by means of the $\Delta E - E$ method it was estimated that a $dE/E = 3\%$ energy resolution would be required of the DSSSDs. At this point it was proposed that post-degrader atomic masses could be reconstructed by combining MCP and DSSSD timings and therefore with a proposed 100 ps timing resolution for the DSSSDs. As justified in future sections due to the small target thickness, relying upon the MCPs solely and extrapolating ion trajectories into the target and correcting for target energy losses is sufficient for atomic mass reconstruction. Assuming a separation of 1.5 m between the MCPs, an MCP timing and position resolution of 120 ps and 1 mm FWHM was estimated as a requirement to limit the velocity broadening of the reconstructed gamma-ray energy peak [87][96].

4.7 Simulations for SDB Experiments

MOCADI simulations operate by separately calculating ion propagation through a series of materials and magnetic matrices, accounting for possible nuclear reactions, energy and angular straggling of ions and preserving the effect this has on their trajectory, energy, species and charge state entering the next ion-optical element [12]. The fundamental limitation of this approach is that it fails to take into account the geometric effects of the shapes and positions of detectors and beamline materials. The electrostatic wire grids covering the MCP emissive foils for example are not included in the MOCADI simulations. This is because a low (4.01MeV/u) energy ^{64}Ni ion beam at Coulomb barrier energies would be fully stopped, slowed and/or widely scattered in the 10-20um diameter gold-plated tungsten wires [87]. MOCADI does not have the capability to account for the shape of the grid and the consequently geometrically correlated transmission of ions through it. The wire grid is therefore necessarily excluded from the simulation resulting in an over estimation of foil transmission. Furthermore MOCADI does not have the capability to simulate Coulomb excitation and the detection of resulting gamma-rays in the HPGe array. Any estimation of required detector performances for the kinematic reconstruction limiting the precision of the

gamma-ray Doppler correction must therefore rely on limiting geometric approximations regarding the HPGe array. In order to more accurately predict required SDB detector resolutions a simulation capable of taking into account these geometrical effects must be performed. In order to study the feasibility of SDB experiments more generally, a simulation would need to take into account Coulomb excitation cross sections in order to estimate the number of Coulomb excitations in future SDB experiments. The feasibility of SDB experiments would then depend upon the precision with which ions could be identified and gamma-ray transitions reconstructed with detectors operating with feasibly achievable performances. Depending upon the performance achieved by detectors in test experiments, the simulation could then inform the design of specific SDB experiments in the FAIR era such as the necessary separation of the MCPs for particle identification and gamma-ray Doppler correction. Furthermore, a geometrical simulation with simulating the Coulomb excitation of ions, their gamma-decays, the detection of these gamma-rays and their Doppler correction could therefore be used similarly to UCHiCARI in section 3.4.5 to infer the transition strength of excited states by comparing the shape of the experimentally Doppler corrected transition peaks to simulated ones as a function of simulated lifetime.

4.7.1 Geant4 simulations for SDB experiments

In order to investigate the feasibility of SDB experiments at the SuperFRS with AGATA and to more accurately estimate the performances that would be required of SDB detectors a simulation fulfilling these requirements was produced. The scope this simulation includes the transport of a test beam through the SuperFRS to the SDB degrader, its propagation through the proposed SDB setup, single and multi-step Coulomb excitation of the test beam and the detection and reconstruction of ions and gamma-ray energies in the proposed detectors with realistic resolutions. A stable ^{64}Ni test beam was selected as the nuclear structure of its low-lying 2^+ and 4^+ excited states is well known from prior Coulomb excitation experiments [89][90][91]. Furthermore, a ^{64}Ni ion beam can be produced at the existing GSI facility and delivered by the FRS at the appropriate energy for tests of the slowing down process in future test experiments [35]. These simulations could be used to plan these future test experiments and in turn the results of these experiments could be used to validate the simulations.

4.7.2 SDB simulation architecture

MOCADI was specifically designed for the simulation of the transport of relativistic heavy ion through the FRS and SuperFRS in mind and was validated in FRS experiments [10]. MOCADI was therefore used to simulate the transport of ^{64}Ni through the SuperFRS until entering the SDB setup is simulated in MOCADI. The beginning of the SDB setup beyond the degrader is a thin iron vacuum window which closes a large vacuum chamber containing the MCPs, target and DSSSDs. Beyond this point the aforementioned geometry of SDB beamline materials and detectors limits the scope over

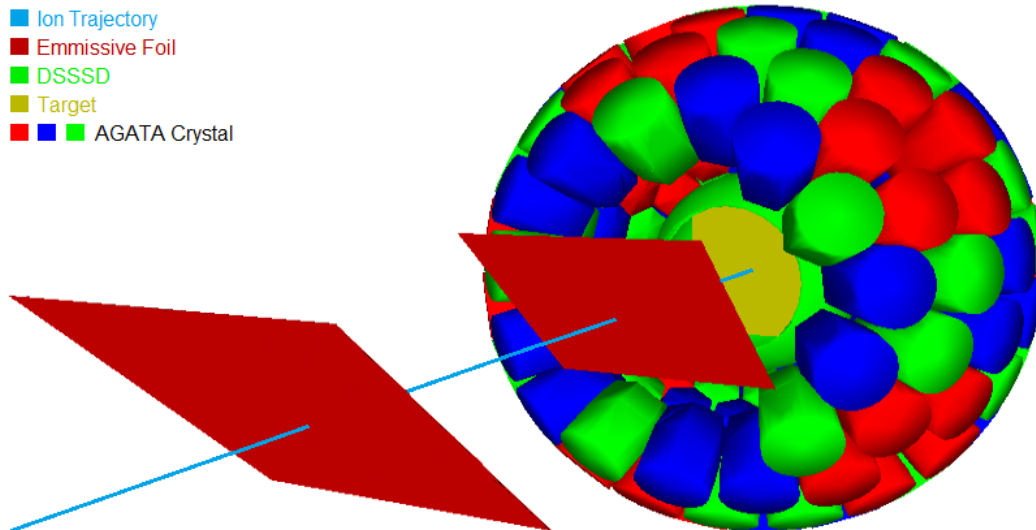


Figure 4.4: *Geant4 Visualisation of HISPEC SDB Experiment Geometry including AGATA (red, blue, green), the thin foils (red), wire grids (black), target (gold) and DSSSD array (green) without vacuum chamber. Thin foils brought closer together (57cm separation) for purposes of illustration.*

which MOCADI simulations can be relied upon before realistic geometric effects (such as the electrostatic wire grids described in section 4.7) must be considered. The Geant4 software framework fulfills this requirement for fully geometric propagation of ions through realistically shaped detector geometries and facilitates the implementation of Coulex physics processes [97].

4.7.3 Geant4 simulated SDB geometry

A Geant4 simulation based on the SDB setup proposed in [87] and illustrated in 4.3 was designed. A visualisation of this geometry including AGATA (red, blue, green), the emmissive foils (red), target (gold) and DSSSD array (green) with and without the vacuum chamber is shown in figures 4.4 and 4.5. The geometry of the AGATA array used in these simulations was generated using AGATA simulation toolkit [98][99]. Not shown are the 10-20um gold-plated tungsten wires behind the emmissive foils [87]. As illustrated in figure 4.6 and shown in figure 4.4 the emmissive foils are tilted to 45 degrees so that secondary electrons can be knocked into a magnetic drift volume connected diagonally to the main vacuum chamber. A CAD drawing showing these diagonal vacuum chambers as they were constructed by University of Koeln workshop is shown in figure 4.7.

4.7.4 Coulomb excitation in Geant4

Natively available Geant4 software C++ classes facilitate the implementation of user built physics processes such as Coulomb excitation applicable to individually simulated ion propagation events. A Geant4 physics process based on the *G4InelasticCoulombScattering* code developed for DSAM experiments in [100] calculates a mean-free-path for nuclear

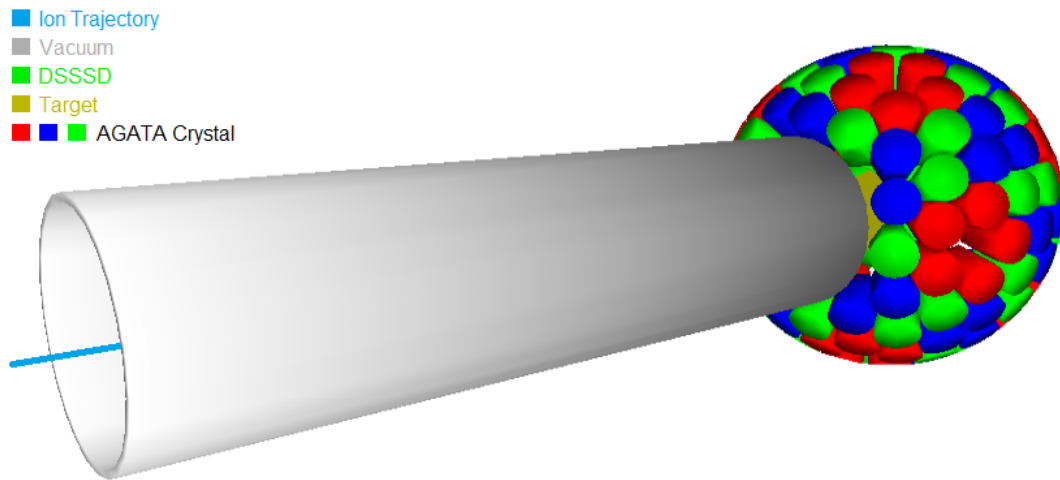


Figure 4.5: *Geant4* Visualisation of HISPEC SDB Experiment Geometry including AGATA (red, blue, green) and vacuum chamber (grey) enclosing the thin MCP foils

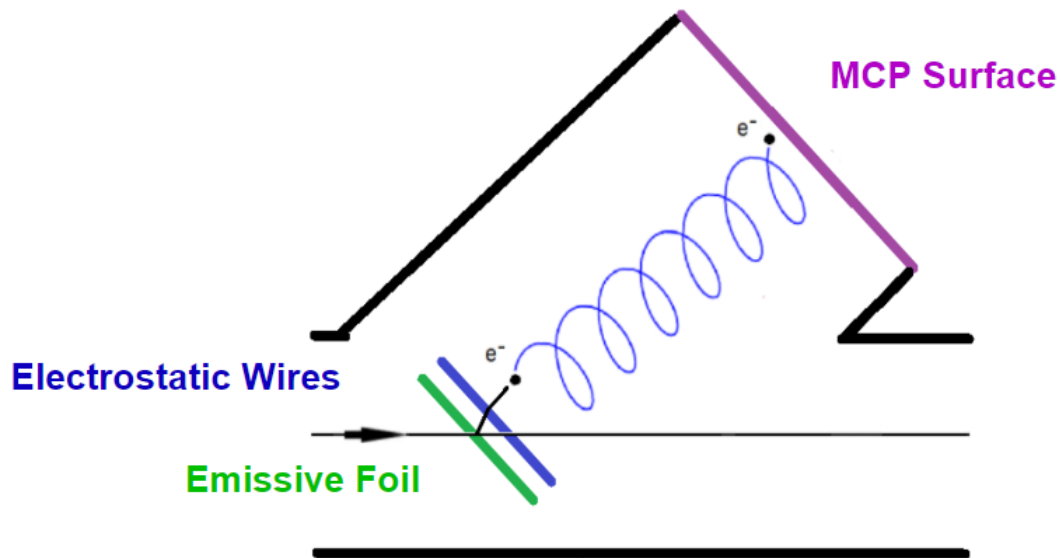


Figure 4.6: *Illustration of MCP detection process. Incident ion enters foil left, knocking out secondary electron. Electron is accelerated by electrostatic wire grid into the diagonal drift volume. Magnet Array along drift volume (not illustrated) provides longitudinal magnetic field along drift volume causing electron to spiral in helical pattern towards surface of the MCP where it is detected.*

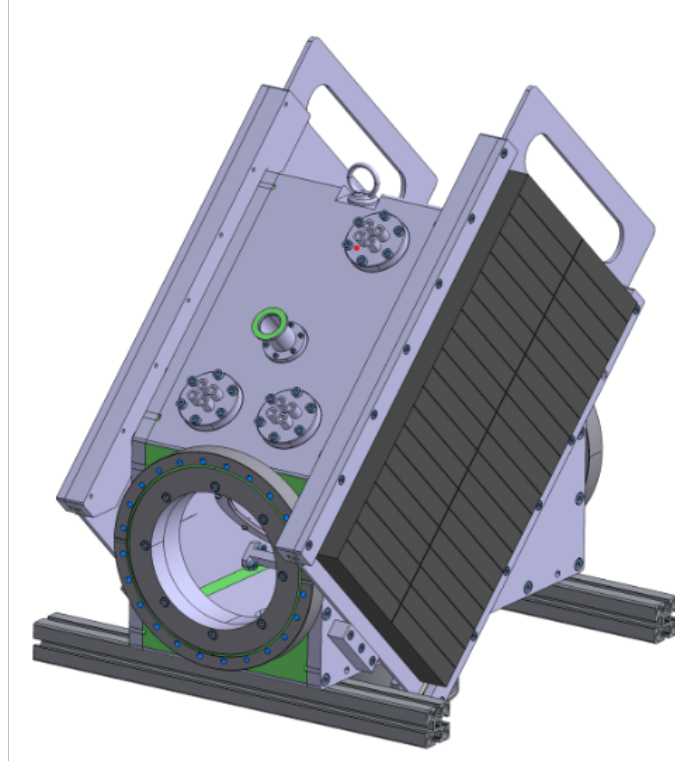


Figure 4.7: CAD drawing of MCP detector system including black magnet array blocks along drift volume length Horizontal volume connected to main SDB vacuum chamber with flanges and encloses a SDB emissive foil. CAD drawing courtesy of University of Koeln workshop.

collisions for projectiles in the target depending upon its density. As the spacial propagation of the projectile ion is simulated through the target this mean-free-path is evaluated with a random number at every spacial step to determine if a scattering occurs, fulfilling the role of the $(\frac{d\sigma}{d\Omega})_{Ru}$ Rutherford scattering cross section in equation 2.29. If a scattering occurs, a further series of random numbers determines the probability P_{if} if an excitation from an initial state i occurs and if so to what final state f . The cross section informing the rate at which excitations occur is read from a file generated prior during runtime. These cross sections are calculated for all user input combinations of projectiles and targets using user supplied nuclear structure information such as nuclear matrix elements and associated reduced transition probabilities and excitation energies. These reduced transition probabilities $B(O_{\lambda}; I_1 \rightarrow I_2)$ can come from experimentally observed de-excitations with transition rate such as those in equations 2.18 and 2.19 as probability of a dexcitation is related to the probability for an excitation with [17].

$$B(E/M\lambda; I_f \rightarrow I_i) = \frac{2I_i + 1}{2I_f + 1} B(E/M\lambda; I_i \rightarrow I_i) \quad (4.4)$$

The ranges of scattering angles and projectile kinetic energies over which cross-sections are calculated are also supplied by the user. Cross sections for projectiles with kinetic energies below E_{cline} in equation 2.27 fulfill the Cline condition for safe electromagnetically dominated Coulex [39]. At these kinetic energies the Coulomb excitation cross section is calculated with the CLX code which is a FORTRAN implementation

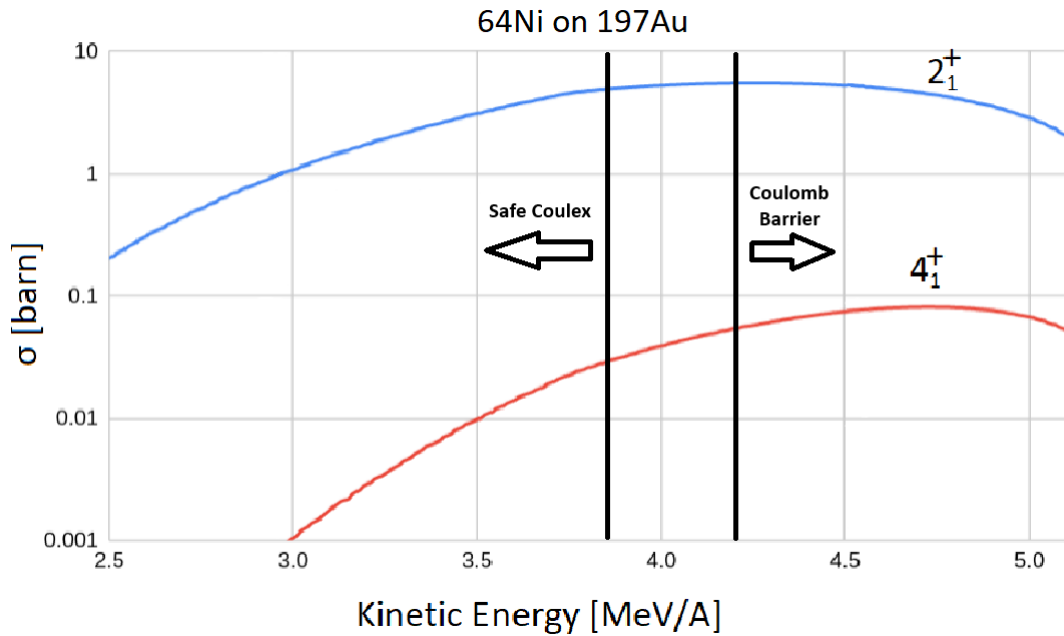


Figure 4.8: Single 2^+ and multi-step 4^+ projectile Coulomb excitation cross sections for ^{64}Ni on ^{197}Au target. Low energy Safe Coulex cross-sections calculated with CLX [101]. High energy cross sections calculated with DWEIKO [63]. Intermediate region is a linear interpolated between the CLX and DWEIKO cross sections.

of electromagnetically dominated Coulomb excitation [101] from [39]. Higher kinetic energies ($\approx > 500\text{MeV}$) are calculated with the DWEIKO code which was designed for intermediate energy Coulomb excitation where nuclear contributions need be included [63]. Cross sections for energies between these ranges are taken as the linear interpolation between the two. Figure 4.8 shows the angle-integrated single and multi-step Coulomb excitation of a ^{64}Ni projectile to its first 2^+ and 4^+ excited states by a ^{197}Au target. The cross section increases to a maximum until just beyond the Coulomb barrier with incident projectile kinetic energy where nuclear reactions such as fusion begin to compete. The calculated Coulex cross section of the 2^+ state is of the order of $10^{-1} - 10^0$ barn, close to that of the 2^+ state Coulex cross section for the similar ^{74}Zn projectile ^{208}Pb target example case in figure 4.2 [86].

4.7.5 ^{64}Ni SuperFRS ion-transport simulations

Beams produced in the SuperFRS production target must be identified before they are delivered to SDB experiments. This enables the strength of the SuperFRS magnets to be tuned for the delivery of ions of interest to SDB experiments. This will be achieved in the SuperFRS (similarly to the BigRIPS and Zerodegree spectrometers in section 3.1.3) with the $TOF - B\rho - \Delta E$ method, separating ions as they are deflected through the SuperFRS's magnets and interact with beamline detectors [12][50]. As the primary beam traverses the beamline detectors and materials necessary for its identification, it slows from an incident 634 MeV/u energy to 233 MeV/u at the SDB degrader. According to

the HISPEC letter of intent, isotopes which can be delivered to SDB experiments with $10^4 - 10^7$ p/s intensity are targeted in SDB experiments [84].

MOCADI degrader thickness simulations

The Coulomb barrier for a ^{64}Ni projectile on a ^{197}Au target is 4.2 MeV/u. The optimal Al degrader thickness for slowing these ions down to the intended energy can be obtained by simulating the number of number of ions at or below the Coulomb barrier after the degrader in MOCADI [10]. In figure 4.9 the number of below Coulomb barrier kinetic energy ^{64}Ni ions after slowing the degrader is plotted against possible degrader thickness.

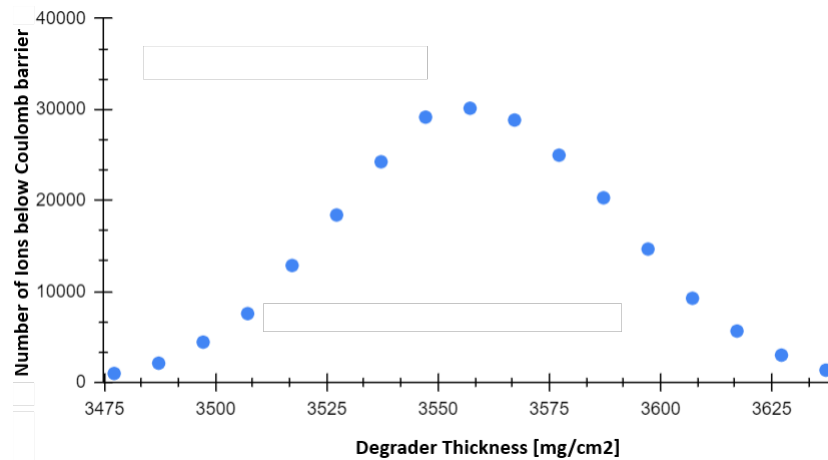


Figure 4.9: Plot of number of sub-coulomb barrier post-degrader ions for chosen Al SDB degrader thickness from MOCADI Simulation of the slowing of an incident 233MeV/u ^{64}Ni primary beam to its Coulomb barrier in ^{197}Au at 4.22 MeV/u.

As shown in figure 4.9 the number of ions at the desired energies is maximised for a degrader of 3558 mg/cm². The origin of this maximum is suggested by the post-degrader energy distribution in figure 4.10. If the thickness of the degrader were decreased, less energy would be lost by passing ions and the mean of the energy distribution in figure 4.10 would shift to higher energies, decreasing the number of ions below the 4.2 MeV/u Coulomb barrier. If the thickness were to increase, the mean of the distribution would shift to lower energies, but the total number of ions stopped at low enough would increase meaning less ions surviving the degrader. As shown in figure 4.9, the competition between increases in the proportion of ions at the targeted energies and the decreases in the number of ions surviving the target as a function of target thickness results in a maximum at 3558 mg/cm².

Beam Quality

As established in sections 4.3 and 4.4, the post-degrader beam purity and spread are important problems that must be overcome in SDB experiments. In order to evaluate the ability of the SDB detectors to handle these problems, post-degrader beam composition,

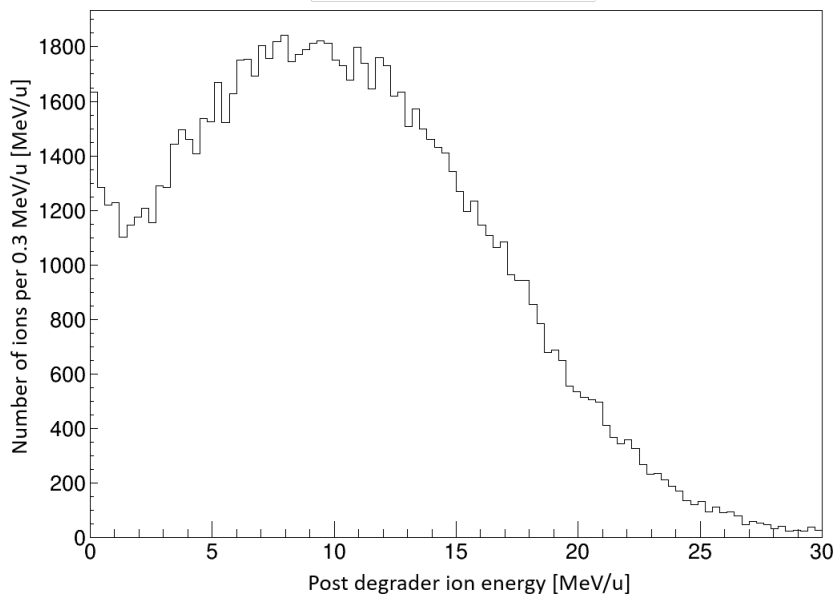


Figure 4.10: Histogram of post-degrader beam energy distribution resulting from the slowing of 233 MeV/u ^{64}Ni beam in a 3558.3 mg/cm² simulated in MOCADI simulation.

Ion	^{64}Ni
x [mm]	0.6 ± 24.6
Y [mm]	-0.2 ± 24.4
A [mrad]	0.1 ± 18.1
B [mrad]	0.2 ± 17.3

Table 4.2: Table of spacial and angular spread of 233 MeV/u ^{64}Ni ions after 3558 mg/cm² Al degrader in MOCADI simulation.

spacial and angular spread was investigated and written as an input file for the later Geant4 simulations to use as a realistic post-degrader beam input. The degree of the spacial and angular straggling in the degrader as the ^{64}Ni SuperFRS primary beam slows down is shown in figures 4.11 and 4.12. As illustrated in the pie chart in figure 4.12, 18.2% of ions are fully stopped in the degrader with a further 6.9% engaging in secondary nuclear reactions leaving 74.9% of incident ^{64}Ni ions remaining. As summarised in table 4.2 post-degrader ^{64}Ni ions have $\Delta x = 24.6$ mm, $\Delta y = 24.4$ mm spacial spread in the XY plane and $\Delta A = 18.1$ mrad, $\Delta B = 17.3$ mrad horizontal and vertical angular spread in the XY plane.

4.7.6 Target spacing

Setting the separation of the MCPs to be 1.4m, bringing all other detectors and beamline materials as close as possible and using the largest target size (transverse to the beam) that fits inside AGATA, the spacial distribution of the beam after it travels through the large SDB vacuum chamber and reaches the target in a Geant4 simulation is shown in

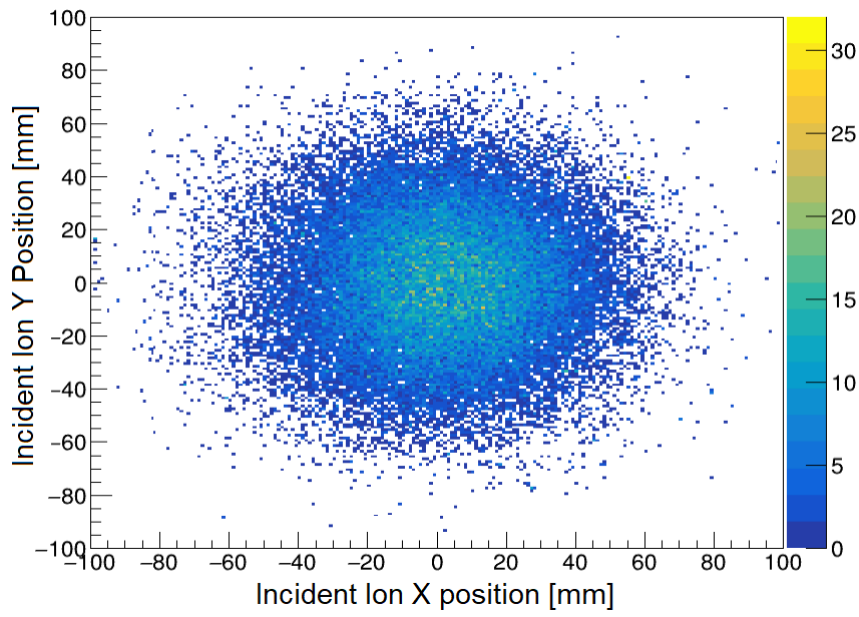


Figure 4.11: Spatial distribution of post-degrader ^{64}Ni ions from MOCADI simulation.

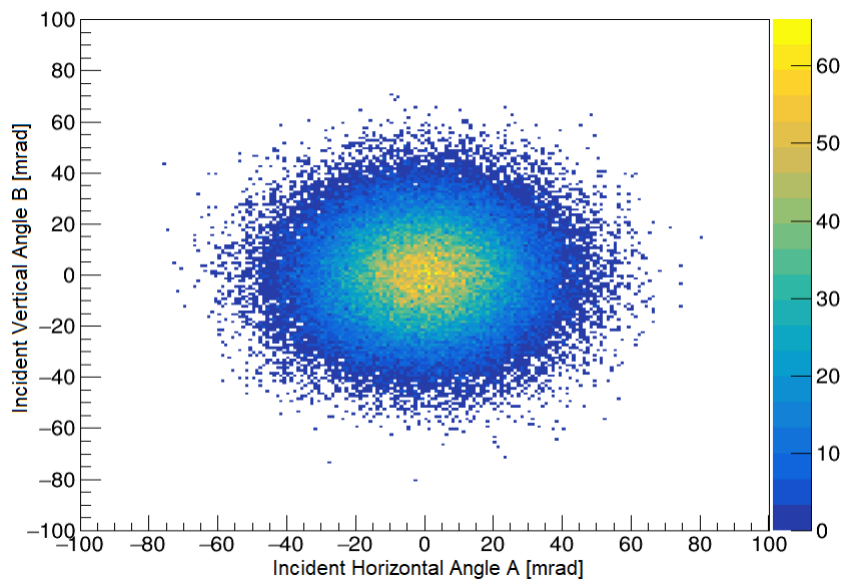


Figure 4.12: Angular distribution of post-degrader ^{64}Ni ions obtained from MOCADI simulation.

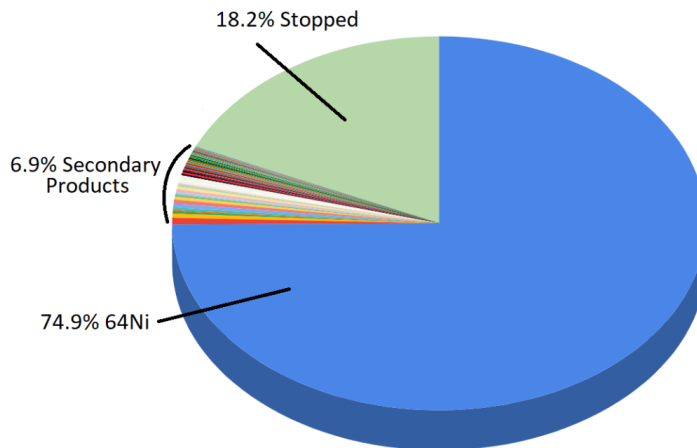


Figure 4.13: Pie chart illustrating the fractions of ions that are fully stopped in the SDB degrader, that underwent nuclear reactions becoming ions other than ^{64}Ni and the remaining ^{64}Ni primary beam fraction. Distribution produced in SuperFRS MOCADI simulation of the slowing of 233 MeV/u ^{64}Ni beam to Coulomb barrier energies in 3888 mg/cm² target.

figure 4.14. In this simulation the realistic post-degrader MOCADI beam was used as an input. The red box shows the region in the XY plane covered by the target. At a 1.4 m MCP separation the target is 1.805 m from the degrader and captures 89.8% of post-degrader ^{64}Ni ions.

4.7.7 Geant4 EM Physics Validation

Essential to the predictive validity of the SDB Geant4 simulation is the accuracy of the simulated electromagnetic physics. Ions must slow down, stop and scatter off of detectors and materials realistically in order for conclusions about the SDB ion kinematics to be made. Gamma-rays must interact with HPGe crystals and shielding realistically so that detection efficiencies and capabilities are reproduced. This is essential for conclusions regarding the ability of SDB detectors to identify transitions from rest-frame gamma-ray energy distributions reconstructed from Doppler shifted energies detected in AGATA to be drawn.

EM ion kinematics validation

Ions in SDB experiments are intended to penetrate thin targets which facilitate Coulomb excitation and deposit identifiable energy deposition curves in silicon DSSSDs. In figures 4.15 and 4.16, LISE++ simulations showing the kinetic energy deposited by a ^{64}Ni beam in a 2 μm ^{197}Au target, and in a 20 μm ^{28}Si target were produced. These targets represent the thin Coulex target and the thin DSSSD layer respectively which are intended to be used in SDB experiments [65]. The amount of energy deposited increases in direct proportion to incident kinetic energy until 1.8 MeV/u for the 20 μm ^{28}Si target and 0.12 MeV/u for the 2 μm ^{197}Au target. In this low-energy regime the beam cannot fully

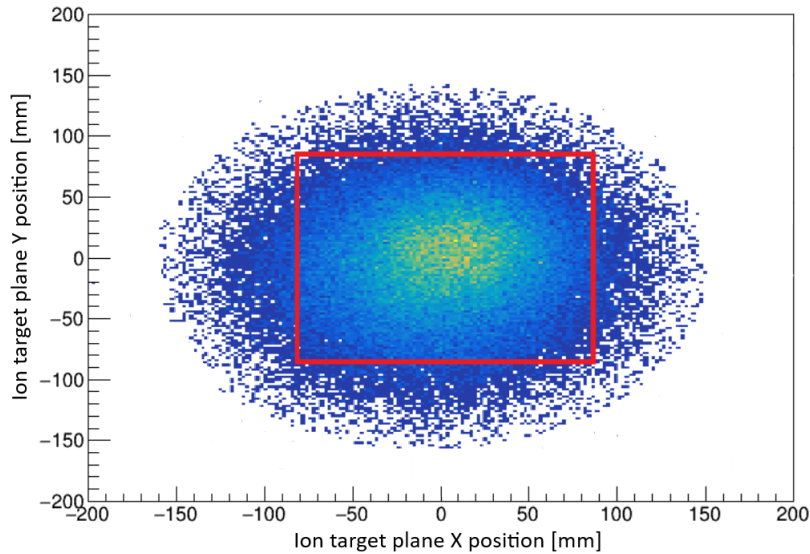


Figure 4.14: *X vs Y histogram of ^{64}Ni beam spread extrapolated from degrader to final SDB DSSSD produced in Geant4 simulation.*

penetrate and so all incident energy is captured. At Kinetic energies beyond this point, known as the *punch through point*, incident ions escape with remaining energy. Equation 3.7 shows the amount of energy deposited per unit length decreases for larger velocities (or higher kinetic energies). The LISE++ simulations in figures 3.15 and 3.16 demonstrate this behavior with the energy deposited continuing to a maximum beyond the punch through point then decreasing thereafter at higher kinetic energies. In 2018 a version of the ATIMA energy loss code called G4AtimaEnergyLossModel was implemented into Geant4 [102]. A Geant4 simulation of the ^{64}Ni projectile on the $2\mu\text{m } ^{197}\text{Au}$ and $20\mu\text{m } ^{28}\text{Si}$ DSSSD across a range of kinetic energies is also plotted in figure 4.15 and 4.16. The average percentage difference between the LISE++ and Geant4 curves was 5.7% for the $20\mu\text{m } ^{28}\text{Si}$ block in figure 4.15 and 1.9% for the $2\mu\text{m } ^{197}\text{Au}$ block in figure 4.16. The LISE++ curve relies upon ATIMA to compute stopping powers which has been extensively validated for ions and materials within this energy and mass range [104]. The close reproduction of LISE++ stopping powers and resultant energy deposition curves for SDB relevant materials with projectiles of masses and energy such as may be used in SDB experiments suggests the Geant4 version of ATIMA predicts similar stopping powers compared to the LISE++ version suggesting it is accurate and valid for use in SDB Geant4 simulations.

Geant4 gamma-ray electromagnetic physics validation

When gamma-rays travel through material they can interact with that material through three main processes (1) the photoelectric effect (2) compton scattering (3) pair production [57]. In the photoelectric effect a gamma-ray interacts with an electron bound to an atom. The electron is then ejected from the atomic shell it occupied with kinetic energy E_e equal to the energy of the photon E_γ minus the binding energy of the electron E_b

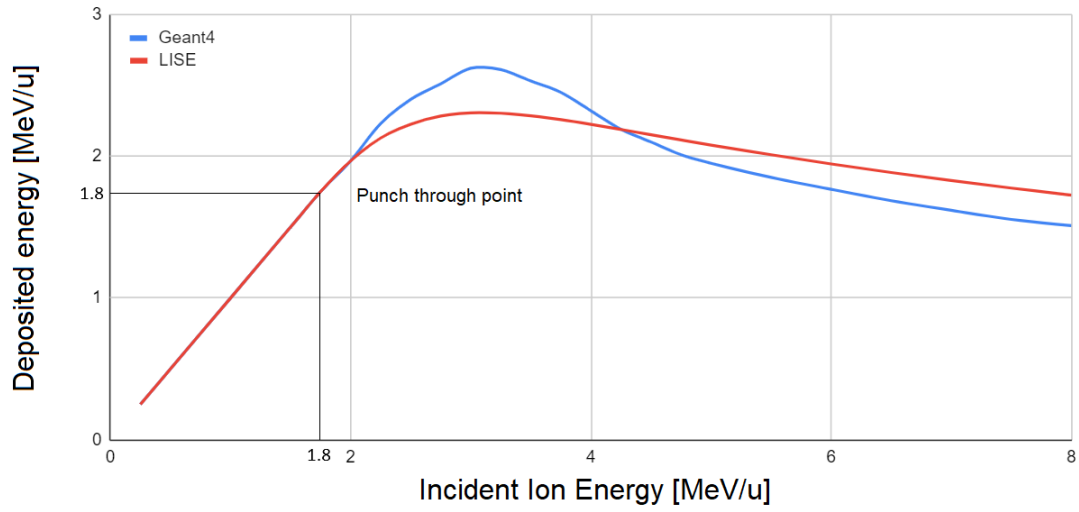


Figure 4.15: Energy deposition curve of ^{64}Ni ions across range of kinetic energies in $20\mu\text{m}$ ^{28}Si target block labelled with 1.8 MeV/u punch through point.

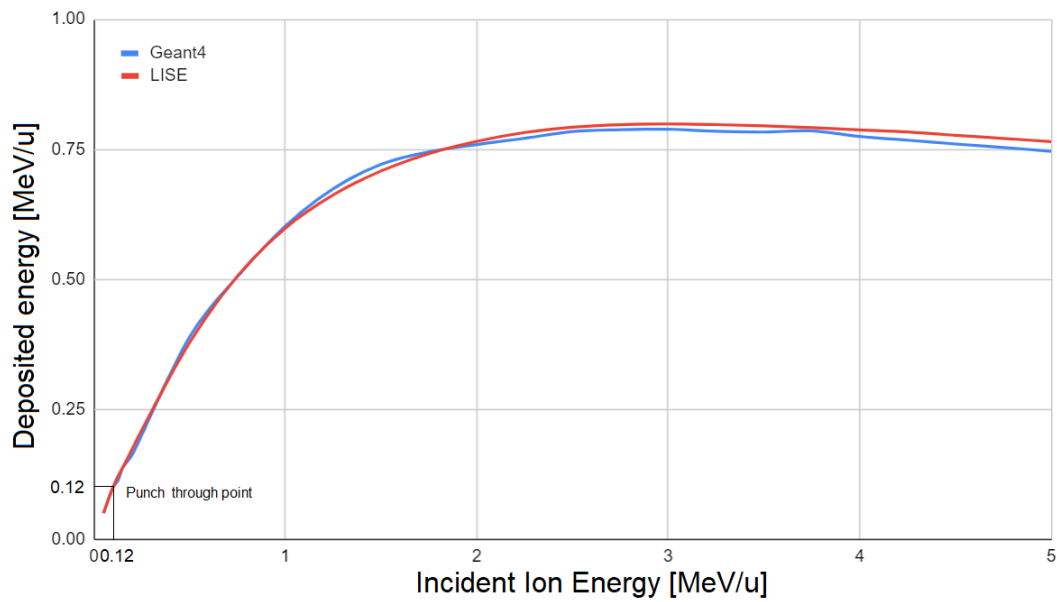


Figure 4.16: Energy deposition curve of ^{64}Ni ions across range of kinetic energies in $2\mu\text{m}$ ^{197}Au target block labelled with 0.12 MeV/u punch through point.

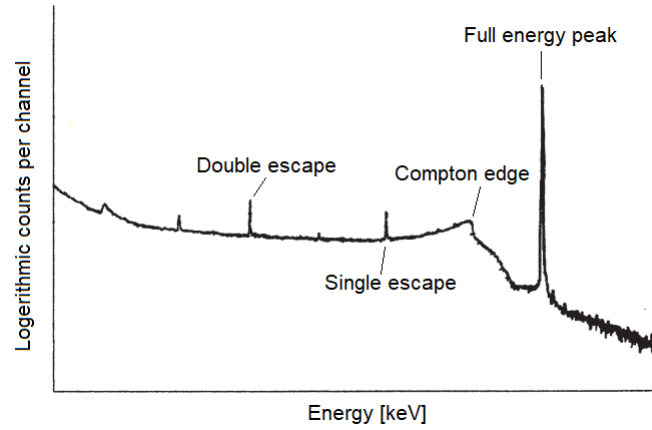


Figure 4.17: HPGe gamma-ray energy distribution with characteristic photopeak, Compton edge and escape peaks from [57].

with $E_e - E_\gamma - E_b$. The atom meanwhile is left in an excited states with excess E_b energy. The vacant atomic shell left by the ejection of the photo electron may then be filled with a higher-energy electron transitioning into it. This may result in the emission of an X-ray with a characteristic energy in the X-ray fluorescence process [57]. Alternatively the atom may de-excite by redistributing its excitation energy between the remaining electrons in the atom, resulting in the release of further electrons from the atom in an Auger cascade [57]. In Compton scattering an incident gamma-ray interacts directly with an electron, delivering part of its energy. The energy of lost by an incident gamma-ray $E_{loss} = E_{\gamma_f} - E_{\gamma_i}$ depends upon the continuous distribution of angles it may scatter θ_{scat} from the incident direction

$$E_{loss} = \frac{m_e c^2}{1 - \cos \theta_{scat}} \quad (4.5)$$

where m_e is the electron mass. The electron then recoils with the kinetic energy transferred to it by the gamma-ray. Within the Coulomb field of a nucleus a gamma-ray with a minimum 1022 keV energy may undergo pair-production of an electron-positron pair each with a rest mass of 511 keV. These electrons and positrons can go on to annihilate with their respective anti-particle partner, escaping the detector as an annihilation photon resulting in a single or double escape peak at 511 or 1022 keV below the full gamma-ray energy respectively. In HPGe detectors such the Miniball detectors described in section 3.2.1, charges freed as a consequence of these processes are accelerated across voltages applied across the detector, enabling their charge to be collected at pairs of anodes and cathodes and the energies the incident gamma-ray can be deduced [56]. As shown in figure 4.17 the energy deposited by a gamma-ray in a HPGe detector takes the characteristic form of full-energy peak, a Compton edge and if there is sufficient energy, a single or double escape peak [59]. In Geant4 the G4EMStandardPhysicsopt4 module contains gamma-ray photoelectric, Compton scattering and pair-production physics processes. In order to validate that these simulated processes realistically reproduce the characteristic gamma-ray energy deposition structures shown in figure 4.17, a Geant4 simulation was produced. In this simulation 1346 keV gamma-rays (such as might be

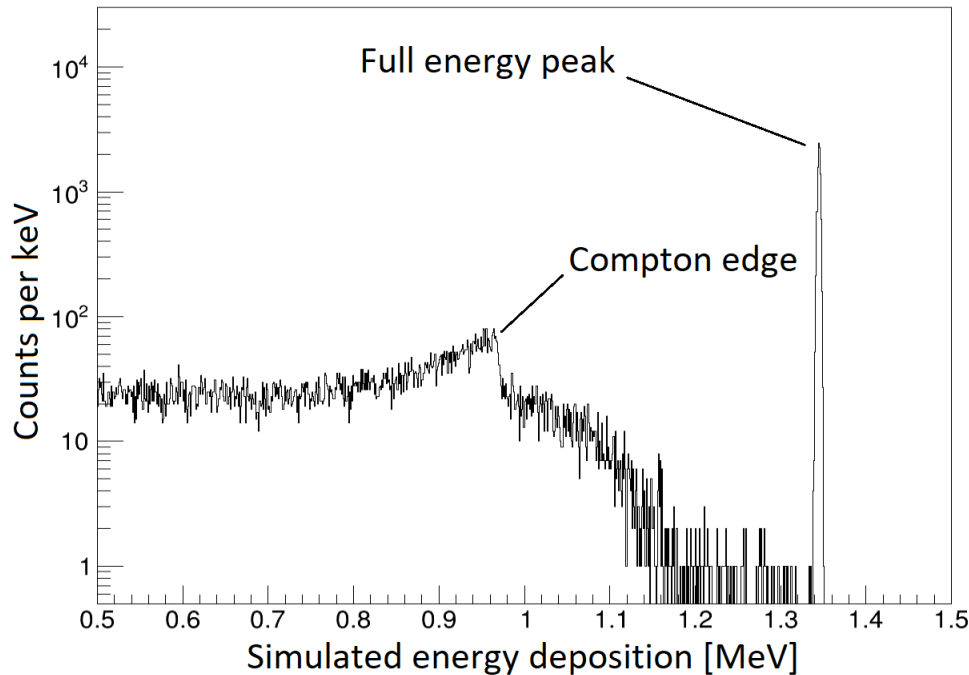


Figure 4.18: Histogram of energy deposition of 1346 keV gamma-ray in Ge target block demonstrating full energy peak and Compton edge structures.

emitted from the deexcitation of ^{64}Ni ion from its first 2^+ state to its ground state) were impinged on a $20\times 20\times 20$ cm Ge target block [89][90][91]. As shown in figure 4.18 the full energy peak is observed at the expected 1346 keV gamma-ray energy. A Compton edge is also observed, reaching a maximum below the full energy peak as in figure 4.17. In large detectors escape peaks are less likely to be observed as the products of pair-productions must travel further to escape instead of annihilate and consequently are more likely to be re-absorbed by the detector. In this simulation the analog for the detector (the $20\times 20\times 20$ cm Ge block) was large, explaining the absence of escape peaks.

4.7.8 DSSSD Geometry

Excited ion scattering angles

As established in section 2.5 ions that are excited in Coulomb excitations at the Coulomb barrier are likely to scatter at large Rutherford scattering angles [39]. Ions that do not engage in inelastic Coulomb scattering or elastic Rutherford scattering only encounter electromagnetic angular straggling, scattering at low angles from the target. As shown in figure 4.19 the polar scattering angle of ions from the target into the DSSSDs in Geant4 simulations is separable into low and wide angular groups. The vast majority of ions scatter at small (<10 deg) angles while ions that engaged in elastic Rutherford scattering or inelastic Coulomb scattering scatter at wide (>10 deg) angles from the target. There is a drop in the number of ions recorded as scattering from the target at 90 degrees. This is because the target is orientated in the transverse plane perpendicular to the direction of the beam. Ions that scatter at 90 degrees travel through the half the length

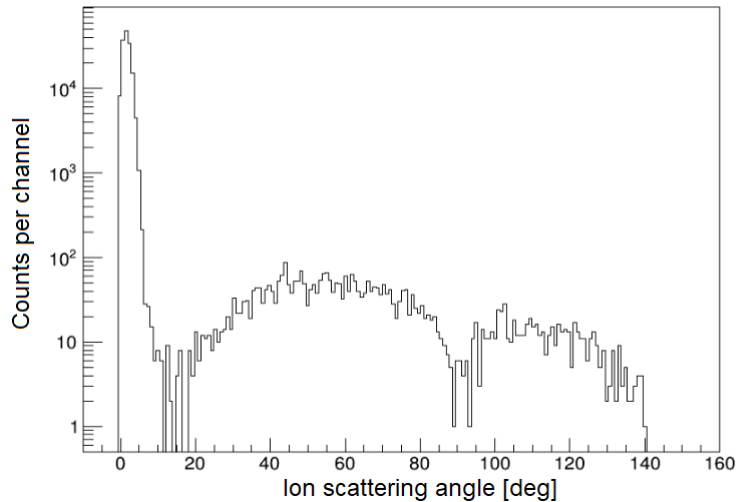


Figure 4.19: Polar scattering angle of ^{64}Ni ions from $2\mu\text{m } ^{197}\text{Au}$ target into DSSSD array. DSSSD Detection efficiency drops at transverse angles along target and angles backwards angles labelled in blue and green respectively.

of the target, are stopped, and therefore are not recorded as reaching the DSSSDs for a scattering angle to be constructed. No ions are recorded as scattering more than 140 degrees. This is because the DSSSD array needs a hole at backwards angles for incoming ions to reach the target through. The angular coverage of the DSSSDs cannot therefore extend completely to these extreme backwards angles. Given only ions which engage in Coulomb excitations are of interest to SDB experiments the DSSSD array needs only cover small angles (>10 deg) at which excited ions are likely to scatter. The angular coverage of the DSSSDs may therefore be reduced at low angles without a reduction in detection efficiency for excited ions.

Backward angle DSSSD angular coverage analysis

By cutting a circular holes in the incoming side of the DSSSD array in the transverse beamline plane with radius R_{in} , the number of ions hitting the target and the number of excited ions captured in the DSSSD array was studied in Geant4. In these simulations the inelastic scattering cross section was enhanced so that the number of excited ions captured by DSSSD arrays of different shapes could studied without running unnecessarily long ion simulations in which inelastic scattering occurs rarely. As shown in figure 4.20, the number of ^{64}Ni ions with incoming spacial and angular distributions from the MOCADI input file that hit the target increases with incoming hole size and plateaus at 90 mm. Despite the reduced backward angle coverage, as less incident ions are blocked from hitting the target on the way in, more ions can engage in excitations and so the number of excited ions captured in the array increases to 90 mm. Beyond 90 mm the vast majority of the incoming beam is already captured and so cutting larger incoming holes and further unblocking the entrance of the beam to the target is no longer dominant over the competing reduction in backward angular

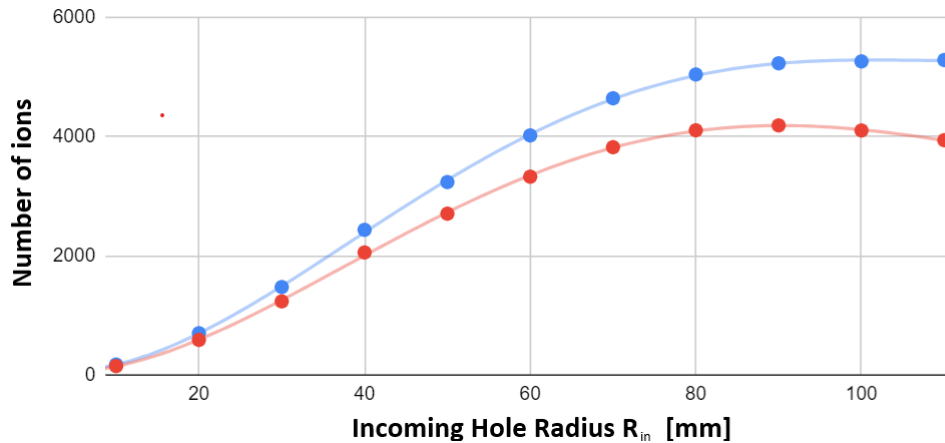


Figure 4.20: Number of incoming ions that hit target (blue) and number of excited ions that are captured in DSSSD array as a function of incoming hole radius (red).

coverage this introduces and the consequent fractional reduction in the number of backward scattered excited ions captured.

4.7.9 SDB DSSSD pileup

After an ion is detected in a DSSSD strip, the strip requires a relaxation time τ to collect the charge and thereby recover for the detection of the next event. When two ions arrive within a single relaxation window, the charge deposited by each event is indistinguishable to the detector and both events are said to be lost in a *piled up* event [104]. For a detector with a τ relaxation time and an incident ion rate of n , the observed count rate m is

$$m = ne^{-n\tau} \quad (4.6)$$

Waveform analysis of the charge signals recorded in the DSSSDs used in a 2022 SDB text experiment as GSI showed the DSSSDs intended to be used in SDB experiments to have a relaxation time of $\tau \sim 20$ us. The pile up rate $P_{rate} = \frac{m}{n}$ at which ion detection events are lost due to this detector relaxation time depends upon the intensity of ions it is exposed to. This in turn depends upon the intensity of the incident beam and the size and positioning of the strips. As shown in figure 4.19, DSSSD strips at low angles are exposed to high ion intensities at which ions are likely to scatter. By cutting larger and larger outgoing holes in the DSSSD array, low angle strips which are prone to high pileup rates can be excluded. The size of the chosen outgoing DSSSD hole should therefore depend upon two things: (1) The rate at which the number of excited ions captured drops as a function of the reduction in forward angle coverage due an outgoing DSSSD hole (2) The minimum tolerable pileup rate for exposed strips determining at what angles ions can be efficiently detected without large losses due to pile up.

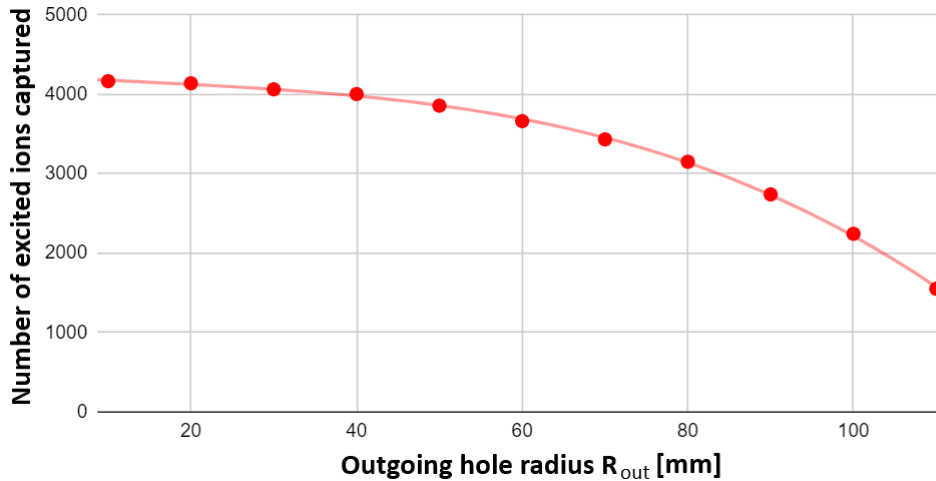


Figure 4.21: Number of excited ions that are captured by DSSSD array as a function of outgoing hole radius.

Forward angle DSSSD angular coverage analysis

In a series of Geant4 simulations in which the incoming DSSSD array hole radius was fixed to 90 mm, the number of excited ions captured in the DSSSD array was found to decrease with increasing outgoing hole radius (R_{out}) as in figure 4.21. As shown in figure 4.21 if the outgoing hole radius was chosen to be 70 mm there would be a 17.6% drop from the number of excited ions capture with with a small hole of a radius of 10 mm. In these simulations the inelastic scattering cross section was enhanced. This reduced the number of ions required to be simulated in order to see the effect different geometries has on the detection rate of ions engaging in Coulomb excitation. The results in figures 4.20 and 4.21 are based on simulations of 1×10^5 ions for each geometry.

DSSSD pile up simulations

For a DSSSD with a fixed size and position within the array, the smaller the individual strip width a DSSSD is divided into, the fewer the number of ions each individual strip is exposed to and the smaller the pile up. The angle that ions scatter from the target is taken from the assumed reaction vertex in the target to the positions of hits in the DSSSD array. The DSSSD strips must therefore be small enough not only that the level of pile up in each strip is sufficiently low but that ion hit positions within the segmented surface of the DSSSDs are measured with sufficient precision. This is important because the ion hit position is required for gamma-ray Doppler correction and particle identification which depend upon the scattering angle into the DSSSDs. In view of commercially available 20um DSSSD strip segmentation, a large 3.125mm strip width (such as was used during the SDB 2021 test experiment) and a smaller 0.625mm width (such as has been used in stopped beam gamma-spectroscopy experiments at GSI) were considered [105]. The pile up rates for strips with these widths were evaluated in Geant4 simulations of the SDB setup using the MOCADI SuperFRS beam as the input

and splitting the DSSSD array into 5x5 cm rectangular DSSSDs arranged approximately spherically around the target (as illustrated in figure 4.22) and removing 90mm and 70mm incoming and outgoing radius circular holes. The pile up rates at a $10^4 - 10^7$ beam intensity range was evaluated as these are the intensities intended to be used in future SDB experiments with rare-isotope beams [84]. As shown in table 4.3 the strip pile up rates for 3.125 mm wide strips with a deadtime of $20\mu s$ vary from 1.08×10^{-3} to 8.32×10^2 at small (<10 deg) scattering angles from the target into the DSSSDs. Strips that are only 0.625 mm wide meanwhile have pile-up rates that vary from 1.25×10^{-4} to 1.16×10^2 at small (<10 deg) scattering angles. As shown in table 4.4 the strip pile up rates for 0.625 mm wide strips with a relaxation time of $20\mu s$ vary from 1.2×10^{-12} to 1.2×10^{-6} at wide (>10 deg) scattering angles from the target into the DSSSDs. Strips that are only 0.625 mm wide meanwhile have pile-up rates that vary from 1.25×10^{-15} to 1.2×10^{-9} at wide (>10 deg) scattering angles. The wide angle strips therefore have a negligibly small pile-up rate, this is expected because as shown in figure 4.19 few ions scatter to angles beyond 10 degrees. The chosen segmentation size of wide angle DSSSD strips is therefore not restricted by pileup, but instead by the minimum segmentation required to provide sufficiently precise hit positions for kinematic reconstruction. It is still worthwhile having some small angle DSSSD coverage because depending on where in the target an ion scatters some excited ions will still scatter this small angle interior rim of the array. This is shown in figure 4.21, where increasing the outgoing hole radius beyond what it was fixed for this analysis would result in further excited ions going undetected. The upper limit of the pileup rate encountered by strips at small angles was 1.16×10^2 p/s to 8.32×10^2 p/s for small strips and large strips respectively at 1×10^7 p/s incident intensity. Taking this upper limit for pileup rate as a constant for small angle (<10 deg) strips a conservative estimate for the fraction of events lost at the highest considered intensity (10^7 p/s) is 22% and 32% respectively for the number of strips with 0.625mm and 3.125 mm widths at low angles. At a 10^6 p/s intensity however this drops to 4% and 2.38% respectively. Depending upon the chosen small (<10 deg) angle strip width between 2.38%-4% of excited ions scattered at these angles would be lost as to pile up. A mid-range 1mm strip segmentation was therefore selected for the purposes of these simulations. Alternative DSSSD segmentations may however be optimal depending upon the experiment, the tolerated loss of ions due to pile up, the beam intensity and the beam spread determining what DSSSD angles at hit with what intensities.

Segmentation mm	Intensity [p/s]	hit chance	exposure rate n	count rate m	pile-up rate
3.125	1.0e4	2.0e-8	2.0e-4	2.0e-4	1.2e-12
3.125	1.0e5	2.0e-8	2.0e-3	2.0e-3	1.2e-10
3.125	1.0e6	2.0e-8	2.0e-2	2.0e-2	1.2e-8
3.125	1.0e7	2.0e-8	2.0e-1	2.0e-1	1.2e-6
0.625	1.0e4	1.8e-9	1.8e-5	1.8e-5	1.2e-15
0.625	1.0e5	1.8e-9	1.8e-4	1.8e-4	1.2e-13
0.625	1.0e6	1.8e-9	1.8e-3	1.8e-3	1.2e-11
0.625	1.0e7	1.8e-9	1.8e-2	1.8e-2	1.2e-9

Table 4.3: Table of upper limits of pile-up rates that 3.125 mm and 0.625 mm width strips that are hit with ions scattering at >10 deg in the target into spherically arranged 5x5 cm DSSSDs encounter in Geant4 SDB simulations as they are exposed to different beam intensities.

Segmentation [mm]	Intensity [p/s]	hit chance	exposure rate n	count rate m	pile-up rate
3.125	1e4	6e-4	6	6	1.08e-3
3.125	1e5	6e-4	6e1	6e1	1.08e-1
3.125	1e6	6e-4	6e2	6e2	1.05e1
3.125	1e7	6e-4	6e1	6e3	8.38e2
0.625	1e4	2.5e-4	2.5	2.0e0	1.25e-4
0.625	1e5	2.5e-4	2.5e1	2.0e1	1.25e-2
0.625	1e6	2.5e-4	2.5e2	2.0e2	1.24
0.625	1e7	2.5e-4	2.5e3	2.0e3	1.16e2

Table 4.4: Table of upper limits of pile-up rates that 3.125 mm and 0.625 mm width strips that are hit with ions scattering at <10 deg in the target into spherically arranged 5x5 cm DSSSDs encounter in Geant4 SDB simulations as they are exposed to different beam intensities.

4.7.10 DSSSD array geometry investigations

As presented in section 4.3.2 the identification of ion atomic number by means of the $\Delta E - E$ method relies upon comparing the energy deposited by ions in a given thickness to the total kinetic energy deposited in both layers. Ions scattering from the target will enter the thin DSSSD layer with a distribution of angles from a distribution of positions within the target. Each ion therefore will traverse a different thickness through the thin DSSSDs. In order to compare the energies deposited by ions in the first layer, these energies must be normalised for the thicknesses traversed. The ideal geometry for a SDB DSSSD array would be a sphere because ions scattering from the target in the spherical focus would enter mostly normal to the surface, travelling the minimum distance through the first layer, depending upon how far from the spherical focus the

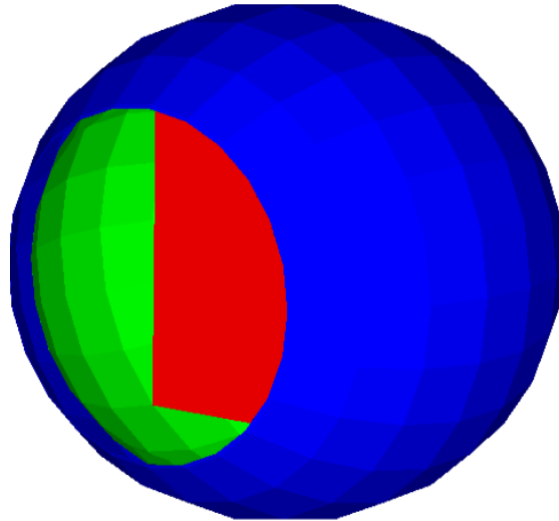


Figure 4.22: *Geant4 Visualisation of spherical DSSSD geometry. Thick DSSSD layer in blue, thin DSSSD layer in green and target in red.*

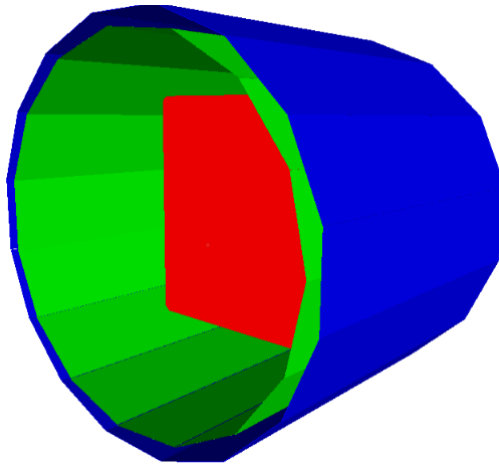


Figure 4.23: *Geant4 Visualisation of barrel DSSSD geometry. Thick DSSSD layer in blue, thin DSSSD layer in green and target in red.*

scattering occurs. Commercially available thin DSSSDs such as those intended to be used in the 2021 SDB test experiment are generally constructed in small rectangles owing to the fragile nature of self supported 20um silicon strips. A Geant4 simulation of an array of rectangular DSSSDs arranged in an approximate sphere such as before was produced and is visualised in figure 4.22. This rectangular composite sphere geometry visualized in figure 4.23 is very geometrically complex and therefore in the interest of investigating the viability of simpler, easier to construct geometries, the barrel and box geometries in figures 4.23 and 4.24 were produced.

Thickness reconstruction

As illustrated in figure 4.23, in the case of an approximately spherical array, the trajectory through the thin foils is first extrapolated to the longitudinal middle of the target. A

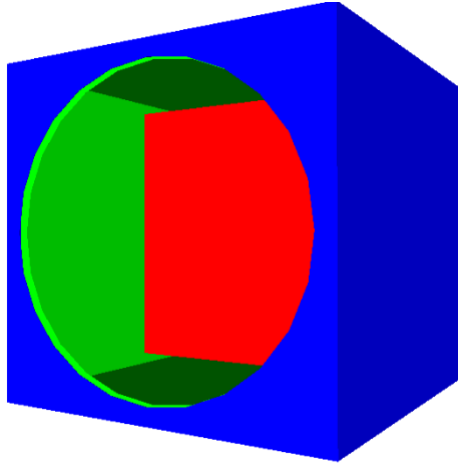


Figure 4.24: *Geant4 Visualisation of box DSSSD geometry. Thick DSSSD layer in blue, thin DSSSD layer in green and target in red.*

straight line parameterised by

$$\mathbf{x} = \mathbf{d} + n\mathbf{u} \quad (4.7)$$

of along \mathbf{x} positions at distances n along direction vector \mathbf{u} from assumed scattering point \mathbf{d} from an origin at \mathbf{o} is then constructed. \mathbf{u} is then solved for by evaluating equation 4.7 with recorded hit position in the thin DSSSD array along this line and the extrapolated \mathbf{d} from the emissive foils. The intersection of this line with the outer surface of the DSSSD sphere with a inner radius r_{in} and thickness x_{thick} , such that $r_{out} = r_{in} + X_{thick}$ at distances x from the same origin

$$|\mathbf{x} - \mathbf{o}| = r^2 \quad (4.8)$$

is then solved for the outgoing hit position r_{out} and thereby the thickness traversed x_{thick} .

$$x_{thick} = r_{out} - r_{in} \quad (4.9)$$

Similarly, the thickness traversed by ions through the box and barrel DSSSD geometries in figure 4.22 and 4.23 can be solved by solving the intersection of the target scattering trajectory with the geometry of the box and barrel. If the geometry of the constructed array is known accurately and a suitable thickness reconstruction algorithm is written all three are geometries equally valid for use in future Coulomb excitation experiments.

4.7.11 Simulated SDB particle identification reconstruction

In order investigate the necessary intrinsic timing and position resolutions required of the MCPs and the necessary intrinsic energy and position resolution required of the DSSSDs for successful post-degrader particle identification, a Geant4 simulation first assuming perfect detector resolutions was performed. As shown in figure 4.13 the fraction of contaminants to remaining SDB primary beam is small and so in this simulation a MOCADI beam input file generated with enhanced secondary reaction

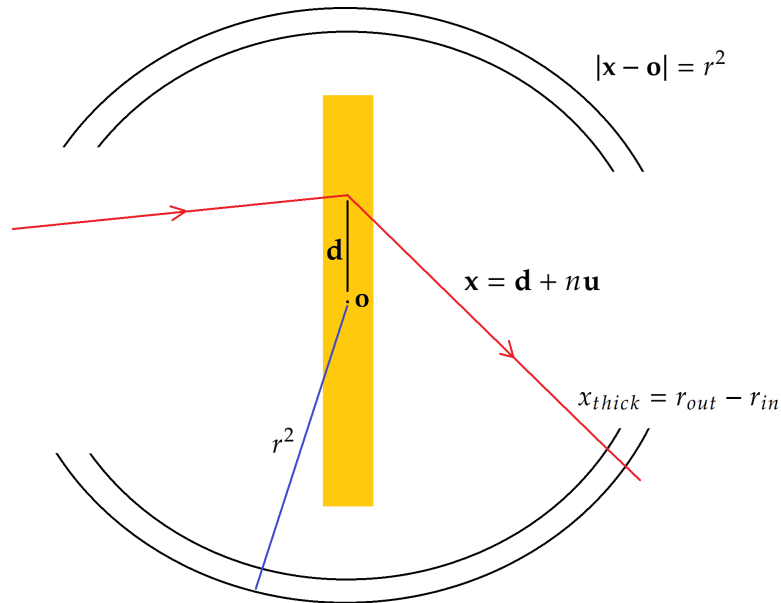


Figure 4.25: Illustration of thin DSSSD thickness traversal reconstruction in spherical case.

cross sections for Ni, Co and Fe isotopes was generated, so that the degree to which atomic masses and numbers are separated is clear. Figure 4.26 shows the simulated $\Delta E - E$ curves for ions of different atomic number, black for Ni, red for Co and blue for Fe normalised for thickness traversed as in section 4.7.11. The energy deposition curves in figure 4.26 show the elements are separated beyond 250 MeV above the punch through point. Figure 4.26 does however show contamination between elements depositing a normalised 40-60 MeV thin DSSSD energy. This suggests that outside of these regions post-degrader atomic number identification is achievable with a $\Delta E - E$ selection if perfect relevant MCP and DSSSD detector resolutions are assumed. The invariant mass of ions in the same Geant4 simulation reconstructed from the extrapolated MCP velocity and the kinetic energy deposited by ions as they stop in the DSSSDs as in section 4.3.1 is shown in figure 4.27. Figure 4.27 shows the mass of ^{64}Ni , ^{63}Ni and ^{62}Co isotopes is clearly separated into distinct Gaussian peaks with small tails resulting in minor contamination. This suggests the atomic mass of post-degrader ions can be reconstructed by this method in simulated SDB experiments assuming perfect relevant MCP and DSSSD detector resolutions.

4.7.12 Simulated SDB gamma-ray reconstruction

In order to investigate the necessary intrinsic timing and position resolutions required of the MCPs and the necessary intrinsic position resolution required of the DSSSDs for successful post-degrader particle identification, a Geant4 simulation first assuming perfect MCP and DSSSD detector resolutions was performed. The gamma-ray energy and position resolutions of AGATA summarised in table 4.1 also involved in the Doppler correction were however implemented as these are the resolutions that will be available

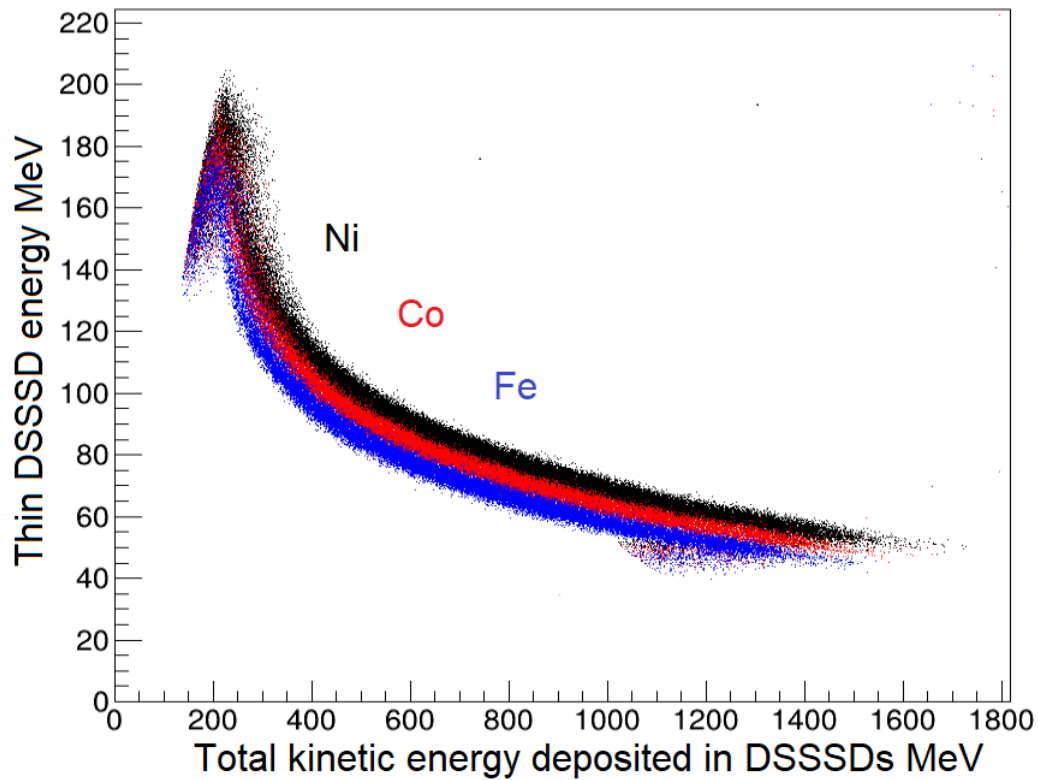


Figure 4.26: Simulated energy deposited by ions in thin DSSSD against total energy collected in DSSSD layers demonstrating $\Delta E - E$ separation of black Ni ions, red Co ions and blue Fe ions.

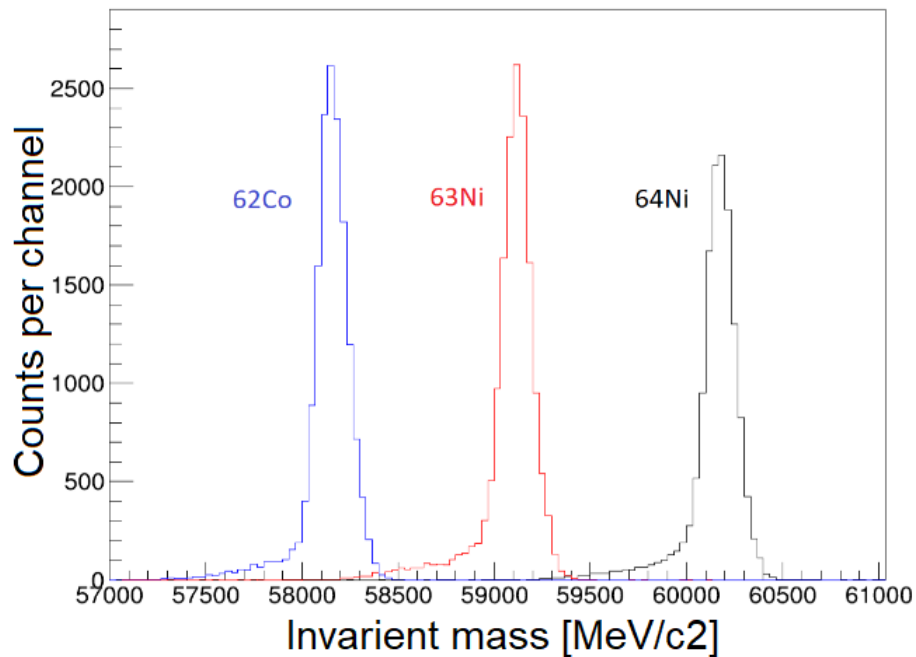


Figure 4.27: Simulated invariant mass reconstruction from MCP velocity extrapolation and DSSSD energy deposition showing separation between ^{64}Ni , ^{63}Ni and ^{62}Co isotope masses.

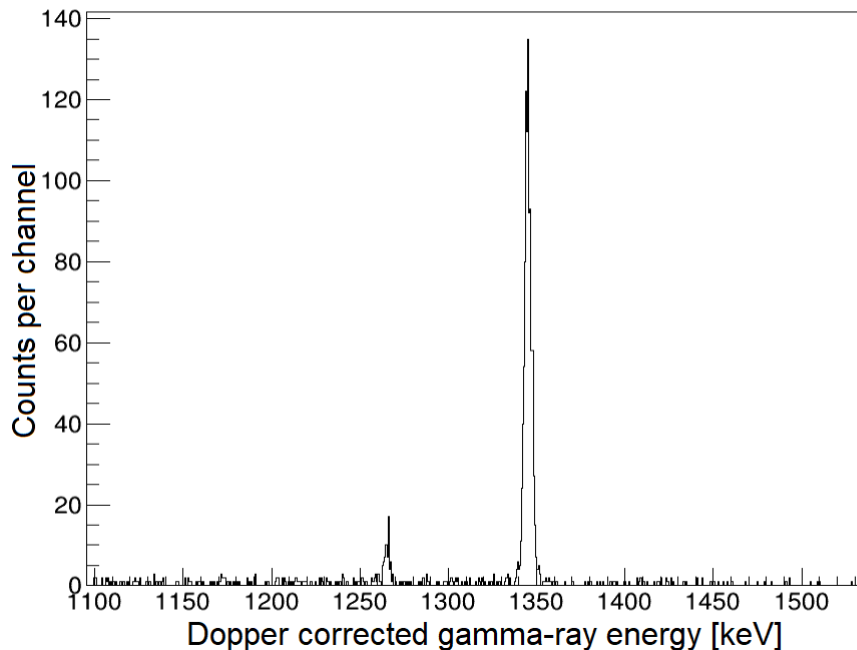


Figure 4.28: Doppler corrected gamma-ray energy distribution reconstructed of excitation of ^{64}Ni to 2^+ and 4^+ states showing reconstructed 1346 keV and 1264 keV $2^+ \rightarrow 0^+$ and $4^+ \rightarrow 2^+$ transitions. Rest-frame gamma-ray energy distributions reconstructed assuming perfect MCP and DSSSD detector resolutions and realistic AGATA energy and position resolutions [92].

in SDB experiments. In these simulations the excitation of ^{64}Ni ions to the first 2^+ and 4^+ excited states and the subsequent $2^+ \rightarrow 0^+$ and $4^+ \rightarrow 2^+$ transitions were simulated [89][90][91]. In this simulation, the energies of the emitted gamma-rays were Doppler shifted in accordance with equation 3.15 depending upon the velocity of the ion and the randomly selected gamma-ray emission angle. By correcting for the Doppler shifting of gamma-rays detected in the laboratory reference frame with the velocity of the ion at emission and the emission angle of the gamma-ray reconstructed such as in section 4.4.3 the rest-frame gamma-ray energies were reconstructed and are plotted in figure 4.28.

4.7.13 Simulated HPGe noise discrimination

As discussed in section 4.6 one of the primary challenges successful SDB experiments must overcome is the identification of gamma-rays of interest from background radiations, including those emitted from the degrader in the slowing down of ions. In order to investigate the degree to which degrader noise can be discriminated on the basis of the timing of its arrival in the HPGe array, realistic degrader noise must be added to the simulation. In 2022 a SDB Coulex test experiment was performed using a ^{208}Pb beam on a thin ^{197}Au target. In this experiment the ^{208}Pb beam was slowed down to the Coulomb barrier at 3.18 MeV/u in a plastic degrader. In this experiment a DEGAS HPGe detector was positioned perpendicular to the target and radiation emitted from the degrader, the target and natural backgrounds was collected [106]. By subtracting the natural background detected when there was no incident beam to when there was an incident

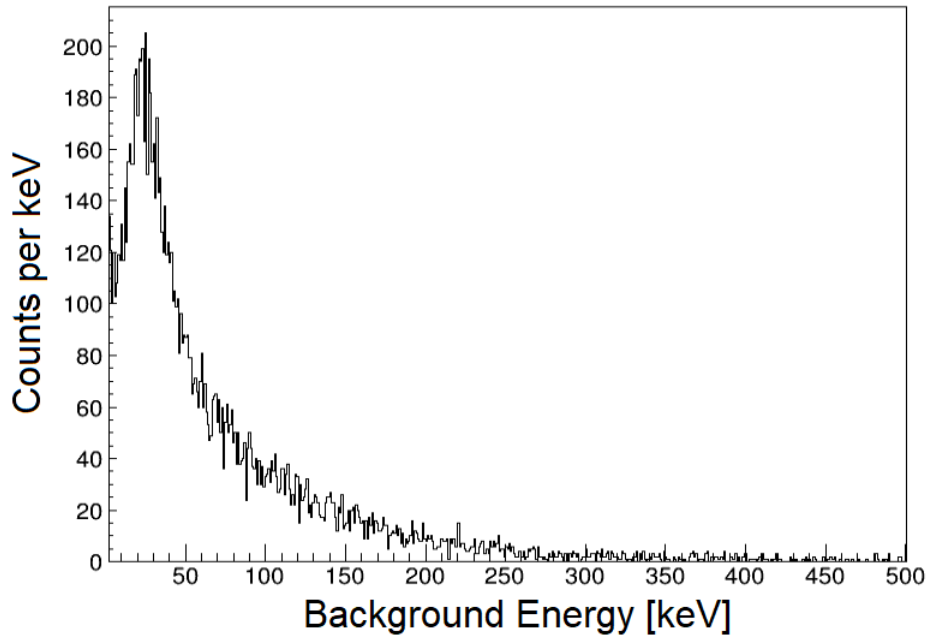


Figure 4.29: *Simulated HPGe background energy extracted from 2021 HISPEC SDB experiment.*

^{208}Pb beam in proportion to the time for which each data set was collected, a HPGe energy consisting of primarily degrader noise was obtained. By sampling the energy and multiplicity of the obtained HPGe energy spectra and scaling for the detection efficiency of the single DEGAS cluster and the beam intensity an estimate of the energy of degrader radiation emitted for each ion incident on the degrader was obtained and is plotted in figure 4.29. The accuracy with which the intensity and energy distribution of degrader background can be obtained is limited by the accuracy with which the emitted background can be extracted from what was detected in the 2021 experiment and separated from natural and target backgrounds. The energy and intensity of the emitted background also depends upon the projectile, target and beam energy combination and therefore the validity of the comparison of a simulated background obtained from the slowing of a ^{208}Pb beam in the plastic degrader used in the 2021 test experiment is limited by the degree to which the emitted radiation would be different for other cases such as the ^{64}Ni beam Al degrader test case. As the simulated energy distribution and the intensity of the detected radiation was obtained from radiation experimentally observed in DEGAS detectors, the validity of the comparison between what was observed by DEGAS and what might be observed in AGATA is limited by the degree to which the detectors are different. The difference in the shielding a DEGAS or AGATA cluster is equipped with for example may have a noticeable effect on the intensity of low energy radiations that penetrate to be detected [57]. The degree to which the success of the suppression of degrader background on the basis of timing is however independent of the energy distribution of the simulated background introduced to the simulation as Bremsstrahlung radiation (of which this radiation is primarily composed) travels at the speed of light. As shown in figure 4.30, if the simulated radiation is emitted from

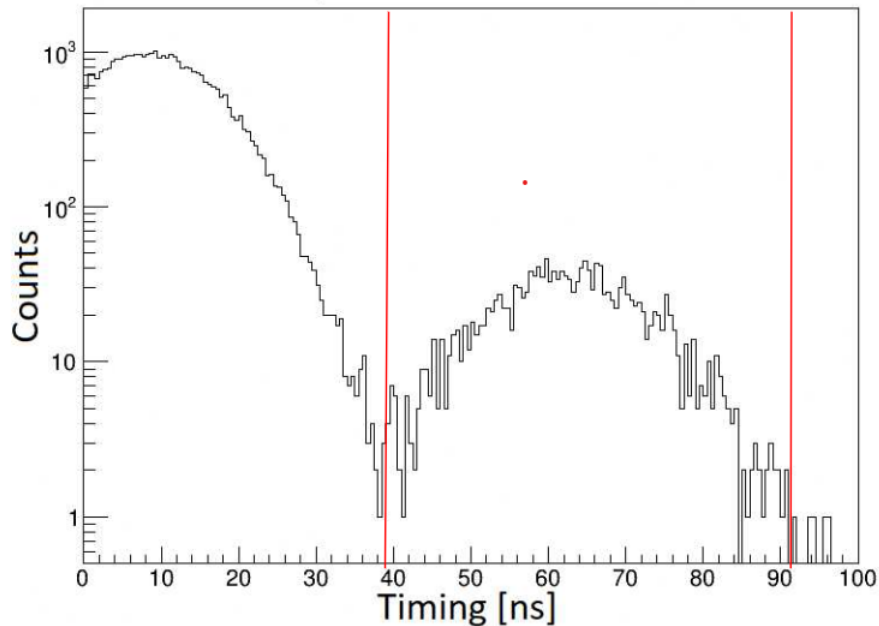


Figure 4.30: *HPGe timing distribution demonstrating time separation of degrader background from ion-correlated signal.*

the degrader and a 25ns (FWHM) AGATA timing resolution is assumed, by taking the timing between the passage of ions through the first emissive foil and the detection of gamma-rays in AGATA, two distinct timing groups are observed. At $\sim 10\text{ns}$ an early arriving group comprised of backgrounds emitted from the degrader is observed. At $\sim 65\text{ ns}$ a second group connected to transitions between excited ^{64}Ni states and backgrounds produced in the slowing of ions in the target and DSSSDs is observed. As illustrated in figure 4.3, by selecting the late timing group, Bremsstrahlung radiation emitted from the degrader can be suppressed on the basis of timing as described in section 4.5.2.

4.8 Study of required detector performance parameters

4.8.1 Performance parameters for particle identification

In order to extract transition energies and strengths from gamma-rays observed in SDB experiments these gamma-rays must be correlated with identified ions. As shown in section 4.13, the invariant mass of ions can successfully be distinguished assuming perfect MCP position and timing resolutions and DSSSD energy and position resolutions. The minimum necessary mass uncertainty ratio $\frac{\Delta m}{m}$ for the identification of ion masses in the HISPEC/DESPEC technical design report is specified as $\frac{\Delta m}{m} = 0.008 - 0.025$ [87]. When the ^{64}Ni mass peaks in figure 4.27 is fit with a Gaussian distribution the mass resolution of the peak in figure 4.27 is $\frac{\Delta m}{m} = 0.00166$ suggesting that without intrinsic MCP and DSSSD position, timing and energy resolution that this mass resolution requirement is achievable. As shown in figure 4.31, if Gaussian detector resolutions

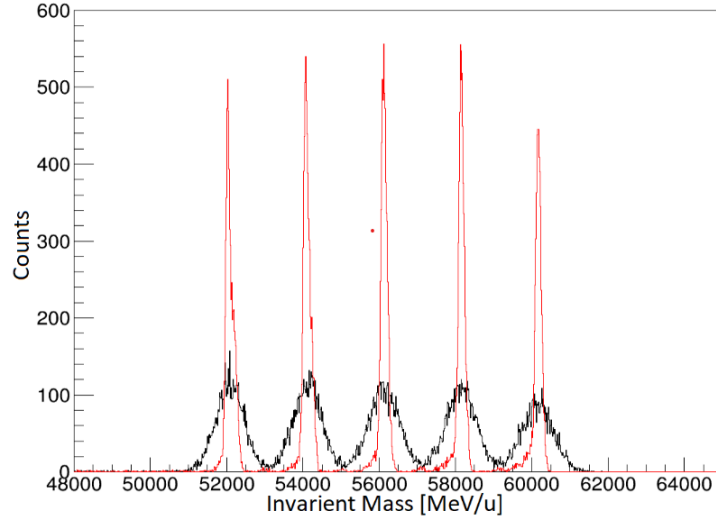


Figure 4.31: Histogram of reconstructed invariant mass of post-degrader isotopes with (black) and without (red) intrinsic MCP position and timing and DSSSD energy resolutions from Geant4 simulation with enhanced post-degrader secondary product production cross sections demonstrating separation of isotopes.

$X_{MCP} = 3mm$, $\Delta t_{MCP} = 500ps$ and $\Delta E_{DSSSD} = 1.5\%$ are introduced to the simulations, the precision of the mass reconstruction is reduced. The width of the (right-most) ^{64}Ni mass peak is reduced from $\frac{\Delta m}{m} = 0.00166$ (red) to $\frac{\Delta m}{m} = 0.00833$ (black). This mass resolution slightly exceeds the lower limit of the mass identification requirement of 0.008-0.025 [87]. As shown in figure 4.31, with $\frac{\Delta m}{m} = 0.00833$ the tails of the mass peaks overlap suggesting that worsened detector resolutions would result in further contamination. Extending this study of the influence of the implementation of detector resolutions on the success with which ion atomic number can be identified, figure 4.32 showing the thickness corrected $\Delta E - E$ histogram when the Gaussian 1.5% DSSSD energy resolution is applied was produced. The $\Delta E - E$ curves in figure 4.32 are very similar to the $\Delta E - E$ curves in figure 4.26 where no energy resolution was applied. Figure 4.32 shows that elements are separable above the punch through point beyond 250 MeV. As before there is however minor contamination between normalized 40-60 MeV thin DSSSD energy deposition. Figure 4.32 therefore shows that outside of these energy ranges elements are still sufficiently separated for ion atomic number identification even with a 1.5% DSSSD energy resolution present.

4.8.2 Performance parameters for gamma-ray Doppler correction

Beyond the identification of ions, the Doppler correction of ion-correlated gamma-rays must be sufficiently precise for transitions of interest to be visible above noise. Therefore resolutions of $\Delta X_{MCP} = 3mm$ and $\Delta t_{MCP} = 500ps$ for the MCP and $\Delta E_{DSSSD} = 1.5\%$ for the DSSSDs were introduced. A $\Delta X_{DSSSD} = 3mm$ position resolution for the DSSSDs and a $\Delta X_{AGATA} = 2mm$ position and $\Delta E_{AGATA} = 1.3keV$ energy resolution for AGATA were also introduced. The resulting reconstructed Doppler corrected gamma-ray energy distribution for the 1346 keV transition from the first 2^+ to the ground state is shown

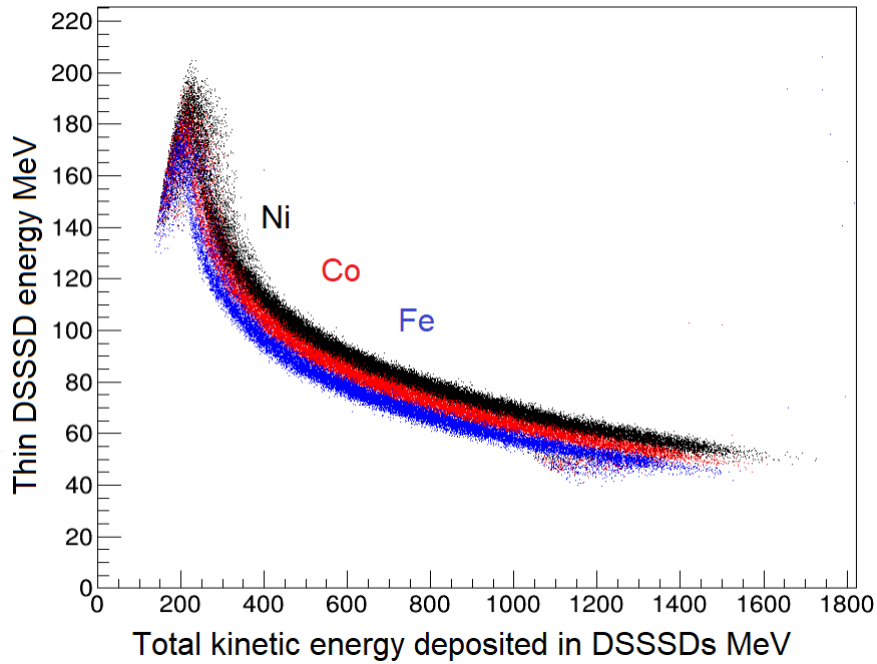


Figure 4.32: Simulated energy deposited by ions in thin DSSSD against total energy collected in DSSSD layers demonstrating ΔE - E separation of black Ni ions, red Co ions and blue Fe ions with 1.5% DSSSD energy resolution.

figure 4.34. With the additional detector resolutions applied the black gamma-ray energy peak is wider and more deformed meaning it would be less distinct above background noise. In order to determine if this Coulex peak is still distinguishable above background noise with realistic detector resolutions applied a Geant4 simulation of the excitation of the single and multi-step coulomb excitation of ^{64}Ni to its first 2^+ excited states and subsequent decay was simulated including simulated background. In figure 4.33 the timing suppression of simulated degrader backgrounds was applied assuming a $\Delta t_{AGATA} = 25\text{ns}$ timing resolution [57]. Furthermore, as established in section 4.7.8 only gamma-rays with AGATA hit positions reconstructed as being emitted at a particular range of wide angles from ions reconstructed as scattering into the DSSSD array are likely to originate from states excited in Coulomb excitations. In order to test the degree to which backgrounds can be suppressed with kinematic conditions, a 2-dimensional energy-scattering selection was made. By identifying gamma-rays correlated ion mass such as in figure 4.31 and atomic number such as in figure 4.32 the resulting Doppler corrected gamma-ray energy spectrum in figure 4.34 was plotted. As shown in figure 4.34, the $2^+ \rightarrow 0^+$ 1346 keV transition is clearly identifiable above the simulated noise. This suggests that even with the SDB detector resolutions summarised in table 4.5, gamma-ray transitions are still identifiable above the simulated backgrounds.

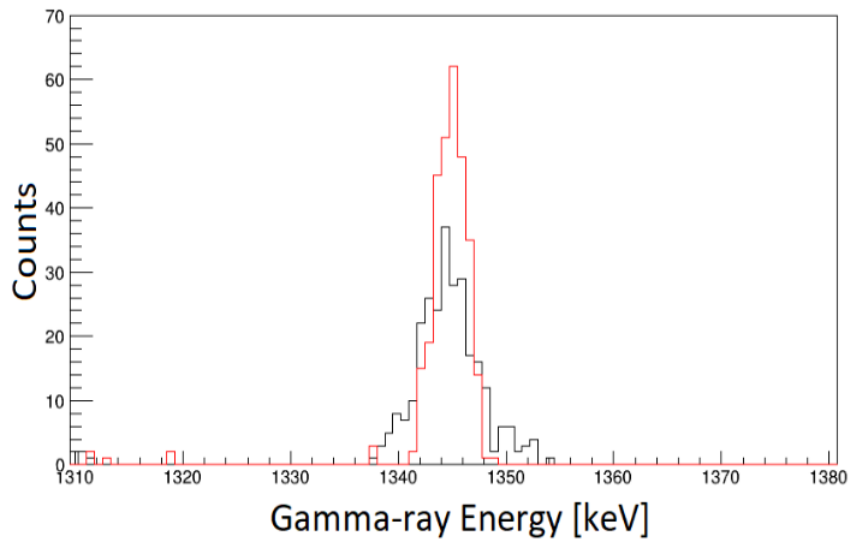


Figure 4.33: Simulated Doppler corrected gamma-ray energy distribution showing reconstruction of 1346 keV $2^+ \rightarrow 0^+$ transition with simulated SDB detector resolutions (black) and without simulated detector resolutions (red).

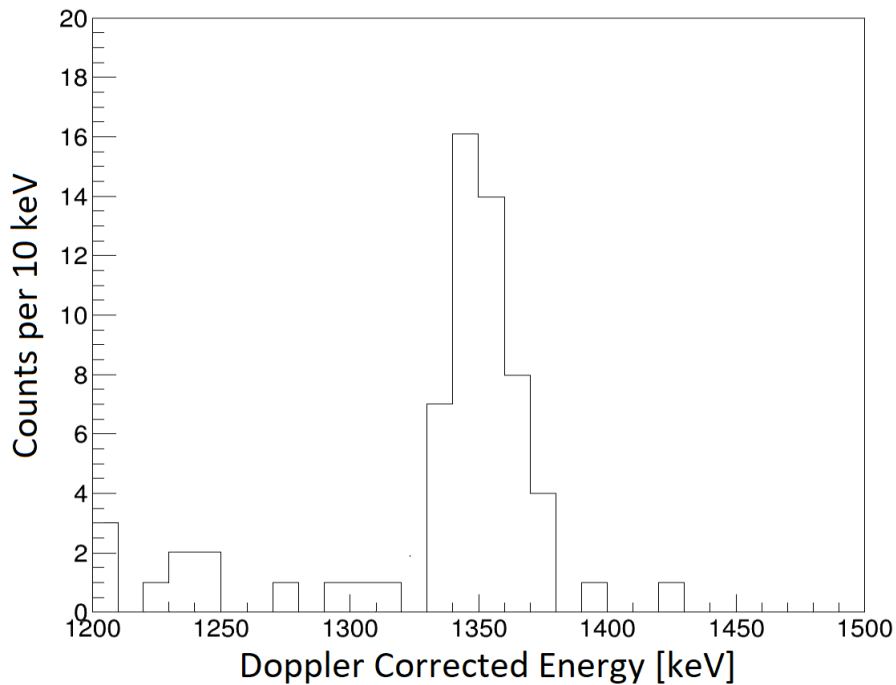


Figure 4.34: Simulated Doppler corrected gamma-ray energy distribution showing reconstruction of 1346 keV transition from first 2^+ excited state of ^{64}Ni using $\Delta E - E$ and invariant mass reconstruction, scattering angle selection and HPGe background timing suppression.

Detector	Energy resolution	Timing resolution	Position resolution
MCPs	-	500ps	3mm
DSSSDs	2%	150ps	3mm
AGATA	1.3 keV	25 ns	2mm

Table 4.5: Table of simulated detector resolutions used in Geant4 simulation study of minimum necessary detector for sufficiently precise Doppler correction and particle identification. AGATA gamma-ray energy and position resolutions from previous experiment [92], timing resolution estimated from [57].

4.8.3 Comparison of new requirements for detectors to previous estimates

Comparison of table 4.5 summarising the newly estimated minimum required detector performance parameters to the previous estimates in table 4.1 suggests a general relaxation of requirements. The previous estimates for required MCP timing and position resolutions were 120ps and 1mm, while the results of this analysis suggest that only 500ps and 3mm resolutions are necessary. The previous estimate for required DSSSD energy, position and timing resolutions were 3%, 1mm and 100ps. The results of this analysis in table 4.5 however suggest that MCP timings can solely be relied upon for velocity reconstruction and that a 3mm DSSSD position resolution is sufficient for particle identification and gamma-ray Doppler correction. As shown in table 4.5, the new simulations do however suggest that the standard for the DSSSD energy resolution must be raised from 3% to 1.5%.

4.9 Hypothetical ^{64}Ni SDB test experiment

SDB experiments are intended to operate at beam intensities of 10^4 to 10^7 p/s over the mass ranges illustrated in figure 4.1 in experiments lasting up to a week [84]. A typical experiment might therefore in total be delivered a total of 5 days of uninterrupted beamtime impinging a 10^6 p/s intensity on the SDB degrader. Such an experiment may be intended to determine the energies of gamma-rays emitted in transitions between the excited states of a chosen beam excited in single and multi-step Coulomb excitations. Another Geant4 simulation using the MOCADI SuperFRS ^{64}Ni beam input file was therefore produced in order to determine the rate at which ion correlated gamma-rays are reconstructed in the Doppler corrected gamma-ray energy peak. With 5 days of 10^6 p/s intensity incident on the degrader, a total of 3.24×10^{11} ^{64}Ni ions would survive the degrader for detection at the 74.9% ^{64}Ni survival rate from figure 4.13. As established in section 4.10.3, at this degree of spacial and angular spread and an MCP separation of 1.4 m, 89.8% of these ^{64}Ni ions would reach a 2 μm ^{197}Au target meaning 2.91×10^{11} enter the target to engage in Coulomb excitations. Using the detector resolutions summarised in table 4.5, the total number of post-degrader-identified ion correlated gamma-rays successfully reconstructed from simulated $2^+ \rightarrow 0^+$ and $4^+ \rightarrow 2^+$ transitions resulting from single and multi-step Coulomb ^{64}Ni excitations was 86012 and 8322 respectively.

With the background suppression techniques presented in section 4.5 both transitions could be un-ambiguously identified above background at 1264 ± 6 keV and 1346 ± 5 keV energies for the $2^+ \rightarrow 0^+$ and $4^+ \rightarrow 2^+$ transitions respectively. In a future experiment a rare-isotope beam may be impinged on the SDB degrader at similar intensity for a similar period [84]. If this beam had single and multi-step Coulomb excitation cross sections similar to the cross sections calculated for the ^{64}Ni projectile ^{197}Au target case in figure 4.8, similar $10^3 - 10^4$ count transition energy peaks may therefore be observed. If only a 10^5 p/s beam intensity is available then scaling these statistics proportionately leads to an estimate of 10^3 and 10^2 counts for $2^+ \rightarrow 0^+$ and $4^+ \rightarrow 2^+$ transitions respectively. At this intensity both transitions may therefore still be visible depending upon Coulomb excitation cross section. If only a 10^4 p/s beam intensity is available however then an estimate of 10^2 and 10^1 for the number of reconstructed $2^+ \rightarrow 0^+$ and $4^+ \rightarrow 2^+$ transition counts respectively is obtained. At this intensity the 10^2 count estimate for the number of gamma-ray transitions obtained subsequent to single step Coulomb excitations suggest that these transitions would likely be identifiable. The 10^1 count estimate for the number of gamma-ray transitions obtained subsequent to the less common multi-step Coulomb excitation interactions however suggest that these transitions are however unlikely to be identifiable.

4.9.1 Conclusions of simulations for SDB experiments

In these simulations the analysis techniques necessary to identify SuperFRS beams after they slow down in the SDB degrader were developed. The procedures for Doppler correcting the energies of gamma-rays correlated with ions excited in Coulomb excitations as well as discriminate these gamma-rays from background noise were also developed. This was achieved by producing MOCADI simulations of the transport and slowing down of a ^{64}Ni primary beam through the SuperFRS and the SDB degrader. The results of these simulations were used as an input for Geant4 simulations designed to simulate the identification of ions after the SDB degrader and to reconstruct the rest-frame energy of Doppler shifted gamma-rays detected in the AGATA array. In these simulations HPGe backgrounds were estimated from a previous test experiment and the ability of proposed background suppression techniques to separate gamma-rays of interest from simulated backgrounds was investigated. The minimum sufficient SDB detector resolutions to identify ions and reconstruct the rest-frame energies of correlated gamma-rays were also investigated. The results of these investigations suggested that the requirements of SDB detectors can in general be relaxed in comparison to previous estimates [87][96]. The required energy resolution of the DSSSDs was however raised from 3% to 1.5% and a 25ns timing resolution in AGATA was proposed to suppress background radiation produced in the slowing of ions in the degrader [57]. The feasibility of a hypothetical 5 day multi-step Coulomb excitation experiment involving a ^{64}Ni projectile on a ^{197}Au target was studied with a beam intensity of 10^6 p/s delivered to the SDB degrader using SDB detectors with the proposed resolutions. The results of the hypothetical experiment showed that adequate numbers of $2^+ \rightarrow 0^+$ and $4^+ \rightarrow 0^+$ ^{64}Ni transitions were observed for the extraction of transition energies from observed gamma-ray energy peaks, suggesting the hypothetical multi-step SDB Coulex experiment was feasible. This was interpreted as suggesting that adequate statistics could be obtained for rare-isotope beams of 10^6 p/s intensities with similar Coulomb excitation cross sections as ^{64}Ni . By scaling the estimates for the statistics acquired in the hypothetical 10^6 p/s Coulex experiment to a 10^5 p/s beam intensity, it was estimated that multi-step Coulomb excitations of rare-isotope beams such as proposed in the HISPEC letter of intent are feasible for 10^5 p/s intensities. At 10^4 p/s beam intensities it was estimated that only single-step Coulomb excitations would occur at a sufficient rate for the gamma-decays of connected states to be observed.

Chapter 5

Bibliography

- [1] E. P. Wigner. "The collected works of Eugene Paul Wigner: Part 1 particles and fields. Foundations of quantum mechanics. The basic conflict between the concepts of general relativity and quantum mechanics." Springer. pp 350. ISBN 978-3-662-09203-3. 1997.
- [2] R. Oerter. "The theory of almost everything: The standard model, the unsung triumph of modern physics" Penguin group. pp 2. ISBN 978-0-13-235578-6. Sept 2006.
- [3] F. Strocchi. "An introduction to non-perturbative foundations of quantum field theory" Oxford university press. Chapter 2. ISBN 978-0-19-878923-9. August 2016.
- [4] Y. Blumenfeld, T. Nilsson, P Van Duppen. "Facilities and methods for radioactive ion beam production" Phys. Scr. T152, 014023. Jan 2013
- [5] T. Otsuka, A. Gade, O. Sorlin, T. Suzuki, Y. Utsuno "Evolution of shell structure in exotic nuclei". Rev. Mod. Phys. Vol 92 015002. Mar 2020.
- [6] E. K. Warburton. J. A. Becker. B. A. Brown. "Mass systematics for $A=29-44$ nuclei: the deformed $A\approx 32$ region". Phys. Rev. C. Vol 41. Mar 1990.
- [7] T. Otsuka, R. Fujimoto, Y. Utsuno, B. A. Brown, M. Honma, T. Mizuaki. "Magic number in exotic nuclei and spin-isospin properties of the NN interaction. Phys. Rev. Lett. Vol 87. 082502. Aug 2001.
- [8] I. Dillmann et al. "N=82 shell quenching of the classical r-process 'waiting-point' nucleus ^{130}Cd ". Phys. Rev. Lett. Vol 91. 162503. Oct 2003.
- [9] Z. Podolayk. "The High-resolution in-flight spectroscopy (HISPEC) project at FAIR" Int. Jol. Mod. Phys E. Vol 15. pp 1967-1977. DOI: 10.1142/S0218301306005411. Nov 2006.

- [10] H. Weick et al. "Slowing down of relativistic few-electron heavy ions". NIM B. Vol 164-165. pp 168-179. Apr 2000.
- [11] S. Akkoyun. "AGATA-advanced gamma tracking array". NIM A. Vol 668. pp 26-58. Mar 2012.
- [12] G. Geissel et al. "Technical Design Report on the SuperFRS" Nustar collaboration. Accessed 24th December 2023 URL: <https://repository.gsi.de/record/54552/files/GSI-2013-05264.pdf>. Dec 2008.
- [13] C. A. Prieto. "Solar and stellar photospheric abundances" Living Rev. Sol. Phys. Vol 13. Article 1. Jan 2016.
- [14] K. Lodders. "Solar system abundances and condensation temperatures of the elements" Astrophysical Journal. Vol 591. pp 1220-1237. Mar 2003.
- [15] F. Hoyle. "The synthesis of the elements from hydrogen". Monthly notices of the royal astronomical society. Vol 106. Issue 5. pp 343-383. Oct 1946.
- [16] A. Lepine-Szily, P. Descouvemont. "Nuclear Astrophysics: Nucleosynthesis of in the universe". Int. Jol. Astrobiology. Vol 11. Issue 4. pp 243-250. May 2012.
- [17] K. S. Krane. "Introductory nuclear physics". Wiley. ISBN 978-0-471-80553-3. Nov 1987.
- [18] E. M Burbidge, G. R. Burbidge, W. A. Fowler, F. Hoyle. "Synthesis of the Elements in Stars". Reviews of Modern Physics. Vol 29. Issue 4. pp 547-640. Oct 1957.
- [19] M. Busso, R. Gallino, G. J. Wasserburg. "Nucleosynthesis in asymptotic giant branch stars: relevance for galactic enrichment and solar system formation". Annual Rev. Astronomy. Astrophysics. Vol 37. pp 239-309. Sep 1999
- [20] H. Grawe, K. Langanke, G. Martinez-Pinedo. "Nuclear structure and astrophysics". Reports. Prog. Phys. Vol 70. pp 1525-1582. Aug 2007.
- [21] J. C. Wheeler, J. J. Coawn, W. Hillebrandt. "The r-Process in Collapsing O/Ne/Mg Cores" The astrophysical journal. Vol 493. L1001. Jan 1998.
- [22] A. G. W. Cameron. "Some Properties of r-Process Accretion Disks and Jets" The Astrophysical journal. Vol 592. pp 456-469. July 2001.

-
- [23] S. E. Woosley, J. R. Wilson, G. J. Mathews, R. D. Hoffman, B. S. Meyer. "The r-Process and Neutrino-heated Supernova Ejecta" *The Astrophysical Journal*. Vol 433. pp 229. Sep 1994.
- [24] K. Takahashi, J. Witt, H. Th. Janka. "Nucleosynthesis in neutrino-driven winds from protoneutron stars." *Astronomy and Astrophysics*, Vol 286. pp 857-869. Feb 1994.
- [25] C. Driscler, W. Haxton, K. McElvain, E. Mereghetti, A. Nicholson, P. Vranas, A. Walker-Loud. "Towards grounding nuclear physics in qcd". *Prog. Part. Nucl. Phys.* Vol 121. 103888. Nov 2021.
- [26] M. G. Mayer. "On closed shells in nuclei II" *Phys. Rev.* Vol 75. Issue 12. pp 1969-1970. June 1949.
- [27] O. Haxel, J. Jensen, H. E. Suess. "On the "Magic numbers" in nuclear structure". *Phys. Rev.* Vol 75. Issue 11. pp 1766. June 1949.
- [28] P. J. Brussaard, P. W. M. Galudeman. "Shell-model applications in nuclear spectroscopy". North-Holland. ISBN: 9780720403367. 1977.
- [29] R. F. Casten. "Nuclear structure from a simple perspective". Oxford university press. Second Edition. ISBN: 9780198507246. Mar 2001.
- [30] S. R. Stroberg, H. Hergert, S. K. Bogner, J. D. Holt. "Nonempirical Interactions for the Nuclear Shell Model: An Update" *Annual Review. Nucl. Part. Sci.* Vol 69. pp 307-362. Oct. 2019)
- [31] B. A. Brown. Oxbash for windows pc. MSU-NSCL Report. Accessed 7th May 2024. URL: <https://people.nsl.msui.edu/~brown/resources/MSU-NSCL-Report-No-1289-2004.pdf>. 2004.
- [32] B.A. Brown, W. D. M. Rae. "The shell-model code Nushellx". *Nuclear Data Sheets*. Vol 120. pp 115-118. June 2014.
- [33] A. Jungclaus et al. "Observation of Isomeric Decays in the r-Process Waiting-Point Nucleus ^{130}Cd " *Phys. Rev. Lett.* Vol 99. 132501. Sept 2007.
- [34] Shell model calculations courtesy of M. Mikolajczuk, University of Warsaw and Magdalena Górska GSI Helmholtz institute for heavy ion research.
- [35] H. Geissel et al. "The GSI projectile fragment separator (FRS): a versatile magnetic system for relativistic heavy ions". *NIM B*. Vol 70. Issues 1-4. pp 286-297. Aug 1992.

- [36] D. Perez-Loureiro et al. "Neutron-rich fragments produced by in-flight fission of ^{238}U ." *Phys. Rev. C*. Vol 99. 054606. May 2019.
- [37] T. Faestermann, M. Górska, H. Grawe. "The structure of ^{100}Sn and neighbouring nuclei" *Prog. Part. Nucl. Phys.* Vol 69. pp 85-130. Mar 2013.
- [38] V. Vaquero et al. "Fragmentation of Single-Particle Strength around the Doubly Magic Nucleus ^{132}Sn and the Position of the $0f_{5/2}$ Proton-Hole State in ^{131}In ". *Phys. Rev. Lett.* Vol 124. 022501. January 2020.
- [39] K. Alder, A. Bohr, T. Huus, B. Mottelson, A. Winther. "Study of nuclear structure by electromagnetic excitation with Accelerated Ions". *Rev. Mod. Phys.* Vol 28. 432. Chapter 1-2. Oct 1956.
- [40] R. B. day, T. Huus. "Low-lying levels in ^7Be and ^{10}Be " *Phys. Rev.* Vol 85. 761. Feb 1952
- [41] P. G. Hansen, J. A. Tostevin. "Direction reactions with exotic nuclei" *Annual. Rev. Nuc. Part. Sci.* Vol 53. pp 219-261. Dec 2003.
- [42] T. Parry. "Structure of neutron-rich nuclei in ^{132}Sn region". University of Surrey. PhD thesis. Accessed 7th May 2024. URL: <https://inspirehep.net/files/378cb8d760e628f135326e3426b2d29e>. Nov 2023.
- [43] H. Ueno, "RI beam facility project at RIKEN and physics programs" *Eur. Phys. J. Special Topics*. Vol 162. pp 221-229. Nov 2008.
- [44] T. Nakagawa, M. Kidera, Y. Higurashi, J. Ohonishi, A. Goto, Y. Yano. "New superconducting electron cyclotron resonance ion source for RI beam factory project". *Rev. Sci. Inst.* Vol 79. 02A327. Feb 2008.
- [45] K. Yamada, "Upgrade of the rf system for RIKEN Ring Cyclotron, RRC" *Journal of the particle accelerator society of Japan*. Vol 17. Issue 3. pp 159-168. 2020.
- [46] M. Odera, Y. Chiba, T. Tonuma, M. Hemmi, Y. Miyazawa, T. Inoue, T. Kambara, M. Kase, T. Kubo, F. Yoshida. "Variable frequency heavy-ion linac, RILAC: I. Design, construction and operation of its accelerating structure". *NIM A*. Vol 227. Issue 2. pp 187-195. Nov 1984.

-
- [47] N. Sakamoto, O. Kamigaito, Y. Miyayawa, T. Mitsumoto, A. Goto, Y. Yano. "Construction of the RF-resonator for the RIKEN intermediate stage ring cyclotron (IRC)". AIP Conference Proceedings. Vol 600. pp 306-308. DOI: 10.1063/1.1435261. Dec 2001.
- [48] H. Okuno, T. Dantsuka, K. Yamada, M. Kase. T. Maie, O. Kamigaito. "Superconducting ring cyclotron for RIKEN RI beam factory in Japan" AIP Conf. Proc. 1218. pp 1410-1417. DOI: 10.1063/1.3422316. April 2010.
- [49] A. Goto. "Overview of the RIBF accelerators". 2nd PAC meeting for Nuclear Physics experiments at RIBF. Accessed 1st January 2024. URL: https://www.nishina.riken.jp/ribf/NP-PAC/2ndPAC_Presen/goto_NP-PAC070912.pdf. Sep 2007.
- [50] T. Kubo et al. "BigRIPS separator and ZeroDegree spectrometer at RIKEN RI beam factory". Prog. Theo. Exp. Phys. Vol 2012. Issue 1. 03C003. Dec 2012.
- [51] T. Ohnishi et al. "Identification of new isotopes ^{125}Pd and ^{126}Pd produced by in-flight fission of $345\text{MeV/nucleon }^{238}\text{U}$: First results from the RIKEN RI Beam factory". Jol. Phys. Soc. Japan. Vol 77. 083201. Doi: 10.1143/JPSJ.77.083201. Jul 2008.
- [52] N. Fukuda, T. Kubo, T. Ohnishi, N. Inabe, H. Takeda, D. Kameda, H. Suzuki. "Identification and separation of radioactive isotope beams by the BigRIPS separator at the RIKEN RI beam factory". NIM B. Vol 317. Part B. pp 323-332. Dec 2013.
- [53] H. Kumagai, T. Ohnishi, N. Fukuda, H. Takeda, D. Kameda, N. Inabe, K. Yoshida, T. Kubo. "Development of parallel plate avalanche counter (PPAC) for BigRIPS fragment separator". NIM B. Vol 317. Part B. pp 717-727. Dec 2013.
- [54] K. Kimura et al. "High-rate particle identification of high-energy heavy ions using a tilted electrode gas ionization chamber". NIM A. Vol 538. pp 608-614. Feb 2005.
- [55] P. Sigmund. "Particle Penetration and Radiation Effects". Springer. ISBN: 978-3-540-31713-5. Mar 2006
- [56] G. F. Knoll. "Radiation detection and measurement". Wiley. Fourth edition. Chapter 12. ISBN: 978-0-470-13148-0. Aug 2010.
- [57] G. R. Gilmore. "Practical gamma-ray spectroscopy". 2nd Edition. Wiley. Chapter 1. pp 10. ISBN: 9780470861967. Apr 2008.
- [58] N. Warr et al. "The MINIBALL spectrometer". Eur. Phys. J. A. Vol 49. Article 40. Mar 2013.

- [59] G. Duchene et al. "The Clover: a new generation of composite Ge detector". NIM A. Vol 432. Issue 1. pp 90-110. Aug 1999.
- [60] T. J. Ross et al. "Neutron damage tests of a highly segmented Germanium detector". NIM A. Vol 606. Issue 3. pp 533-544. July 2009.
- [61] P. Doornenbal et al, "Lifetime effects for high-resolution gamma-ray spectroscopy at relativistic energies and their implications for the RISING spectrometer" Nucl. Inst. Meth. Phys. A. Vol 613. pp 218-225. Feb 2010.
- [62] C. A. Berulani, C. M. Campbell, T. Glasmacher. "A computer program for nuclear scattering at intermediate and high energies". NSCL, MSU. Accessed 29th December 2023. URL: <https://people.nscl.msu.edu/brown/reaction-codes/bertulani/Dweiko.pdf>. July 2009.
- [63] L. A. Riley et al. "UCGRETINA Geant4 simulation of the gretina gamma-ray energy tracking array" NIM A. Vol 1003. 165305. July 2021.
- [64] O. B. Tarasov et al. "LISE++cute, the latest generation of the LISE++ package, to simulate rare isotope production with fragment-separators". NIM B. Vol 541. pp 4-7. Aug 2023.
- [65] P. Doornenbal, K. Wimmer. "In-Beam Gamma-ray Spectrometer for the RIBF". Proposal for Nuclear Physics Experiment at RI Beam Factory. NP-PAC-18. Accessed 3/2/2024. URL: <https://www.nishina.riken.jp/collaboration/SUNFLOWER/devices/harray/ConstructionProposal.pdf>. Oct 2018.
- [66] J. Taprogge, A. Jungclaus, H. Grawe et al. "Proton-hole and core-excited states in the semi-magic nucleus ^{131}In ". Eur. Phys. Jol. A. Vol 52. DOI: 10.1140/epja/i2016-16347-y. Dec 2016.
- [67] C. Rangacharyulu, "Physics of Nuclear radiations concepts, techniques and applications." Routledge. 1st Edition. ISBN:9781439857779. Dec 2013.
- [68] F. James. "MINUIT - Function minimization and error analysis reference manual". CERN program library long writeups. D506. Accessed 20th January 2024. URL: <https://root.cern.ch/download/minuit.pdf>. Aug 1994.
- [69] "Green IT cube: supercomputing center for GSI and FAIR" GSI Website. Accessed 9th January 2024 URL: "https://www.gsi.de/en/researchaccelerators/research_an_overview/green-it-cube"

-
- [70] J. Taylor. "Introduction to error analysis: The Study of Uncertainties in physical Measurements." 2nd Edition. University Science Books. ISBN: 9780935702750. July 1997.
- [71] R. Barlow. "Asymmetric errors". PHYSSTAT 2003. Accessed 2nd February 2024. Url: <https://www.slac.stanford.edu/econf/C030908/papers/WEMT002.pdf>. Sep 2003.
- [72] L. van Dommelen. "Quantum Mechanics for Engineers". University of Michigan. 2012 Accessed 30th January 2024. URL: <https://websites.umich.edu/~ners312/CourseLibrary/Dommelen.pdf>. June 2012.
- [73] O. Kavatsyuk et al. "Beta decay of ^{101}Sn ". Eur. Phys. A. Vol 31. pp 319-325. Mar 2007.
- [74] R. Machleidt, F. Sammarruca, Y. Song. "Nonlocal nature of the nuclear force and its impact on nuclear structure". Phys. Rev. C. Vol 53. R1483(R). Apr 1996.
- [75] M. Hjorth-Jensen, T. T. S. Kuo. E. Osnes. "Realistic effective interactions for nuclear systems". Physics Reports. Vol 261. Issues 3-4. pp 125-270. Oct 1995.
- [76] B. Fogelberg, K. Heyde, J. Sau. "Energy levels and transition probabilities in ^{130}Sn ." Nucl. Phys. A. Vol 352. pp 157-180. Feb 1981.
- [77] T. Bjornstad et al. "The doubly closed shell nucleus ^{132}Sn ." Nucl. Phys. A. Vol 453. Issue 3. pp 463-485. May 1986.
- [78] B. Pritychenko, M. Birch, B. Singh, M. Horoi. "Tables of E2 transition probabilities from the first 2^+ states in even-even nuclei." Atomic data and nuclear data tables. Vol 107. pp 1-139. Jan 2019.
- [79] A. Orbertelli, H. Sagawa. "Modern Nuclear Physics: From Fundamentals to Frontiers" Springer. 1st Edition. ISBN: 978-981-16-2288-5. Sep 2021.
- [80] H. Gutbrod. "FAIR Baseline Technical Report." GSI Repository. ISBN: 9783981129809. Aug 2006.
- [81] P. Spiller et al. "The FAIR Heavy Ion Synchrotron SIS100". JINST. Vol 15. T12013. Dec 2020.
- [82] W. Barth, R. Hollinger, A. Adonin, M. Miski-Oglu, U. Scheeler, H. Vormann. "LINAC developments for heavy ion operation at GSI and FAIR". Jol. Inst. Vol 15. T12012. DOI: 10.1088/1748-0221/15/12/T12012. Dec 2020.

- [83] Z. Podolayk. "The High-resolution in-flight spectroscopy (HISPEC) project at FAIR" *Int. Jol. Phys E*. Vol 15. pp 1967-1977. Doi: 10.1142/S0218301306005411. Nov 2006.
- [84] Nustar Collaboration. "NUSTAR facility, letters of intent of the nuclear structure, astrophysics and reactions collaboration at FAIR". NUSTAR/ELISE LOI. pp 41-54. Accessed 24th January URL: <https://fair-center.eu/user/experiments/nustar/experiments/elise/elise-documents> 2024. Apr 2004.
- [85] S. Akkoyun et al. "AGATA-advanced gamma tracking array". *NIM A*. Vol 668. pp 26-58. Mar 2012.
- [86] M. Zielińska, S. M. Lenzi, D. Cortina-Gil. *The Euroschool on Exotic Beams*. Springer. Vol 6. pp 43–86. ISBN: 978-3031107504. Aug 2022.
- [87] HISPEC/DESPEC collaboration, "HISPEC/DESPEC technical design report". Nustar. 2020. Accessed 29th January 2024. URL: <https://fair-center.de/user/experiments/nustar/documents/technical-design-reports>. May 2020.
- [88] A.M. Rogers et al. "Tracking rare-isotope beams with microchannel plates". *NIM. A*. Vol 795. pp 325-334 Sep 2015.
- [89] J. M. Allmond et al. "High-precision B(E2) measurements of semi-magic $^{58,60,62,64}\text{Ni}$ by Coulomb excitation." *Phys. Rev. C*. Vol 90. 034309. Sep 2014.
- [90] R. Broda et al. "Spectroscopic study of the $^{64,66,68}\text{Ni}$ isotopes populated in $^{64}\text{Ni}+^{238}\text{U}$ collisions-" *Phys. Rev. C*. Vol 86. 064312. Dec 2012.
- [91] D. little et al. "Multistep Coulomb excitation of ^{64}Ni Shape coexistence and nature of low-spin excitations". *Phys. Rev. C*. Vol 106. 044313. Oct 2022.
- [92] J. Ljungvall et al. "Performance of the advanced gamma tracking array at GANIL". *NIM A*. Vol 955. 163297. Mar 2020.
- [93] F. Naqvi et al. "Development of slowed down beams at GSI/FAIR" GSI Scientific report. PHN NUSTAR FRS. Vol 4. pp 135. 2010.
- [94] P. Boutachkov et al. "Simulations and first tests of slowed down beams project at GSI" GSI Scientific report. *Inst. Meth.* Vol 09. pp 215. 2007.
- [95] K. Summerer, B. Blank. "Modified empirical parametrization of fragmentation cross sections". *Phys. Rev. C*. Vol 61. 034607. Feb 2000.

-
- [96] P. Boutachkov. "Development of slowed down beams at GSI" DITANET 2011. Retrieved 29th December 2023. URL: https://web-docs.gsi.de/wolle/EB_at_GSI/SLOWED-DOWN_BEAMS/TALKS/Boutachkov-2011.pdf. Feb 2011.
- [97] S. Agostinelli et al. "Geant4—a simulation toolkit" NIM A. Vol 506. Issue 3. pp 250-303. July 2003.
- [98] M. Labiche et al. "Simulation of the AGATA spectrometer and coupling with ancillary detectors". Euro. Phys. A. Vol 59. Article 158. July 2023.
- [99] M. Labiche. AGATA. <https://gitlab.com/malabi-agata/agata>. Oct 2023.
- [100] C. Strahl, "New methods for the gamma-ray spectroscopy with position-sensitive detector systems". Phd Thesis. Technical University Darmstadt. Accessed 30th January 2024. URL: https://tuprints.ulb.tu-darmstadt.de/4955/13/Thesis_Stahl_online.pdf. July 2015.
- [101] H. Ower, J. Gerl, and H. Scheit, CLX Coulomb excitation FORTRAN code
- [102] J. L. Rodriguez Sanchez, H. Weick, C. Scheidenberge, H. Geissel, N. Iwasa, A. Prochazka, S. Purushotaman. "Implementation of ATIMA code in the Geant4 transport model." GSI Technical Report. Accessed 30th December 2023. URL: https://www.researchgate.net/publication/327561245_Implementation_of_ATIMA_code_in_the_Geant4_transport_model
- [103] H. Weick, H. Geissel, N. Iwasa, C. Scheidenberger, J. L. Rodriguez Sanchez. A. Prochazka, S. Purushotaman. "Improved accuracy of the code ATIMA for energy-loss of heavy ions in matter" GSI Scientific report. Accessed 7th May 2024. URL: https://web-docs.gsi.de/~weick/atima/ATIMA_GSI_scientific_report_2017-5.pdf. Oct 2018.
- [104] S. Usman, A Patil. "Radiation detector deadtime and pile up: A review of the status of science" Nucl. Engi. Tech. Vol 50. Issue 7. pp 1006-1016. Oct 2018.
- [105] Nustar collaboration. "Advanced implantation detector array (AIDA) technical design report". Nustar. Accessed 29th January 2024. URL: https://edms.cern.ch/ui/file/1865809/2/TDR_HISPEC_DESPEC_AIDA_public.pdf. Nov 2008.
- [106] G. S. Li, "Simulated characteristics of the DEGAS γ detector array." NIM A. Vol 890. pp 148-154. May 2018.

Michael Armstrong

Böcklerstraße 48, 64291,

Darmstadt-Arheligen, Hesse, Germany

m.armstrong@gsi.de

+447713342809

Education

August 2020 - Present PhD Student, Universität zu Köln

Nuclear Physics graduate student at GSI Helmholtz Centre for Heavy Ion Research through the University of Köln in the HISPEC/DESPEC collaboration within NUSTAR. Research includes stopped beam gamma-ray decay spectroscopy of short-lived exotic nuclei at GSI, in-flight gamma-ray spectroscopy of r-process waiting point nuclei ^{130}Cd , Geant4 and ion-transport simulations for HISPEC Slowed Down Beam Campaign for FAIR and detector developments.

Sep 2016 - July 2020 Nuclear Astrophysics MPhys (Hons) University of Surrey

First class masters degree in physics with nuclear astrophysics at the University of Surrey including physics placement year at Jefferson Lab through University of Richmond and exchange year at Nanyang Technological University, Singapore.

Experience

Feb 2019 - Dec 2019 Graduate Student Researcher, Jefferson Lab

Research placement year within Jefferson Lab CLAS collaboration for the University of Richmond. Focusing on development of particle reconstruction software for CLAS12 wide-angle electron scattering spectrometer. Application of Hough transform image processing technique to CLAS12 track recognition and validation with Geant4 simulations.

Jun 2018 - Aug 2018 Research Internship, Window to the Stars, Surrey

Research internship developing Window To The Stars (WTTS) at the University of Surrey. WTTS is simplified front end GUI for the TWIN binary stellar evolution code for teaching at the University of Surrey, Nijmegen and Utrecht, enabling users to study the evolution of single and binary star systems in animated Hertzsprung-russell and Kippenhahn diagrams.

Technical Skills

Analysis of in-flight gamma-ray decay spectroscopy experiment studying low-lying excited states of $^{128-130}\text{Cd}$ with ROOT. Interpretation of results with comparison to Geant4 simulations performed on high-performance computing cluster.

Developed Geant4 and ion-transport simulations evaluating the feasibility of low energy multi-step Coulomb excitation experiments of rare isotope beams in experiments with AGATA gamma detection array produced and separated with the SuperFRS magnetic fragment separator at FAIR.

Technical Skills (continued)

Produced magnetic field simulations of permanent magnet array for conversion foil based MCP ion tracking detector. Implemented DAQ solution for stable beam test experiment at Universität zu Köln tandem accelerator and wrote ROOT based online monitoring and analysis suite.

Participated in a wide variety of nuclear physics experiments in Germany, Japan and the USA applying unique techniques and experimental setups including gamma-ray spectroscopy experiments, storage-ring mass spectrometry and electron-scattering experiments.

Soft Skills

Given talks on nuclear physics results and developments at national APS, IOP and DPG conferences in USA, UK and Germany as well as collaboration conferences. Also given talks on applied machine learning in the context of nuclear physics at a European space agency conference and on cyber security at the University of West London.

Publications

July 2020 CLAS12 Technical Note

M. Armstrong, G. P Gilfoyle, V. Ziegler "CLAS12 Drift Chamber Reconstruction Software Validation", CLAS12-Note, Jefferson Lab. Hall B. July 2020 URL: [<https://misportal.jlab.org/mis/physics/clas12/>]

Jun 2022 DESPEC Setup Technical Report, NIM A

A. K. Mistry et al "The DESPEC setup for GSI and FAIR". Nuclear Inst. and Methods in Physics Research A. Vol 1033. Jun 2022

Aug 2023 Lifetimes of 190W , Phys Rev C (submitted)

E. Sahin et al. "Lifetime measurement of the yeast $2+$ state of 190W " Phys. Rev. C. Aug 2023

May 2023 WASA-FRS TOF Technical Report, NIM A (submitted)

E. Liu et al "A Compact start timecounter using plastic scintillators readout with MPPC arrays for the WASA-FRS HyPhi experiment". Nuclear Inst. and Methods in Physics Research A

Nov 2023 Spectroscopy of ^{94}Pd Phys Rev Let C (in preparation)

A. Yaneva et al "The shape of the $T_z=+1$ Nucleus ^{94}Pd and the role of Proton-Neutron Interactions on the Structure of its Excited States"

Dec 2023 Two-photon decay of ^{72}Ge , Phy Let B (in preparation)

D. Freire-Fernandez et al "Measurement of the Isolated Nuclear Two-Photon Decay in ^{72}Ge ". Physics Letters B.

Conferences

Oct 2019 APS Division of Nuclear Physics Meeting Presentation

M. Armstrong, G. P. Gilfoyle, V. Ziegler "CLAS12 Drift Chamber Reconstruction Code Validation" DNP 2019 Fall Meeting. ID HA.075. Bibcode: 2019APS..DNP.HA075A

Mar 2022 DPG Meeting Presentation

M. Armstrong, G. Hackenberg "Magnet Simulations for HISPEC position tracking detector". DPG 2022 Mainz Meeting. HK 344.

Oct 2021 AI STAR ESA Symposium

M. Armstrong, H. Albers, J. Gerl, M. Gorska, A. K. Mistry "AI Applications In Nuclear Spectroscopy". AI STAR Oct 2021

Apr 2022 IOP Nuclear Physics Conference

M. Armstrong, P. Boutachkov, M. Gorska, J. Vesic, J. Jolie "Simulations for HISPEC Slowed Down Beam Campaign at FAIR". IOP Nuclear Physics Conference. April 2022.